Control on Multiple Floating Bodies

PhD Thesis

Shuangrui Yu

Hydrodynamics and Ocean Renewable Energy Laboratory
Department of Naval Architecture, Ocean and Marine Engineering
University of Strathclyde, Glasgow

May 2024

This thesis is the result of the author's original research. It has been composed by the author and has not been previously submitted for examination which has led to the award of a degree.

“天之道，损有余而补不足；人之道则不然，损不足以奉有余。” ——《道德经》

“The law of nature,
It reduces those who have surpluses,
To supplement those who are deficient.
The man’s way is contrary.
It reduces those who are deficient,
To offer those who have surpluses.”

——Laozi, Chapter 77, *Tao Te Ching*

Abstract

Floating multi-body systems include different types of structures, such as arrays of wave energy converters (WECs) that extract energy from their interaction with the ocean waves, floating hybrid platforms requiring stabilisation of their main structure, and photovoltaics whose overall movement needs to be reduced for best energy capture. These systems exhibit sophisticated dynamics in sea conditions. The control of such a system is a topic that has rarely been investigated in previous research. This thesis aims to address the challenge of controlling multiple floating bodies with mechanical connections by presenting the development and application of a novel optimal control strategy.

The first objective is to overcome the challenge presented by the complex behaviour of multiple floating bodies in waves. In the dynamic equation, the wave-induced radiation force was described by a convolution term using Cummin's impulse response function (IRF). Frequency domain identification (FDI) was adopted to estimate the convolution term with hydrodynamic parameters, as an expression of the linear representation. The mechanical connections within the system were coupled with the dynamic equation using constraint matrix method, and effectively reduced the degrees of freedom (DoFs) in the system. The state-space representation of dynamic equation provides a computationally efficient framework and benefits the integration of control forces into the system model.

Upon establishing the dynamic equation of multiple floating bodies, the optimal control strategy, based on Pontryagin's Maximum Principle (PMP), can be applied to the system. This involves iterative optimisation of objective functions over a specified

time horizon. A key component of the present approach is the implementation of declutching control, an effective method for exerting control force on multiple floating bodies. Its control force is a discrete function varying between 0 and a constant, typically generated by the damping effect of power take-off (PTO) system between bodies.

The optimal declutching control method was adapted for different application scenarios, depending on the formulation of dynamic equation and the selection of objective functions. In the case of hinged boxes, the results in relative angle and heave motion at the hinge point are compared with published results. The good agreement of these results validated the accuracy of multiple floating bodies' dynamic model. The efficiency of the control method was evident in its capacity to either minimise or maximise selected objective function across a wide range of wave frequencies. Declutching control demonstrated good ability in tuning the phase between multiple floating bodies. Additionally, the control strategy showed robust adaptability to irregular waves and extendibility in systems including three or more bodies.

In cases involving the control of floating platforms, the objective function was set as the minimisation of platform's motion. An auxiliary structure was connected to the platform to construct the floating multi-body system. A crucial aspect of this system is the damping coefficient of the PTO between the bodies, which is instrumental in reducing the motion of the platform at a specific wave frequency. The present control methodology extends this capability, effectively reducing the platform's motion over a broader range of wave frequencies and under irregular wave conditions. Furthermore, the mitigation of platform motion and the enhancement of PTO power output can be achieved simultaneously, which is described as "killing two birds with one stone" in this research. Subsequent analyses revealed that the initial mass of the auxiliary structure and the damping coefficient of the PTO are also critical factors influencing the efficiency of the control strategy.

In cases of WECs, the objective function was set as the maximisation of power output from the PTO system. For multi-body WEC configurations, energy is absorbed through the relative motions between adjacent bodies. The control command adjusts

the damping force, thereby influencing these relative motions between the bodies. The control effects of two objective functions: the power generated by wave (P_{wave}) and that absorbed by PTO system (P_{PTO}), were compared in the analysis. The coupling of damping coefficient and relative motion poses a challenge for achieving convergence under the objective function P_{PTO}. This can be potentially addressed by applying alternative optimisation algorithms.

In conclusion, this research fills the gap in controlling floating multi-body systems and provides practical guides for their optimisation in various application scenarios.

Contents

List of Figures

List of Figures

List of Tables

List of Nomenclatures

$\bar{J}$	Time-averaged objective functions
β	Control command of WEC latching control
$\boldsymbol{\lambda}_{\mathrm{r}}(\omega)$	Added damping in frequency domain (Ns/m or Nms/rad)
$\boldsymbol{\mu}_{\mathrm{r}}(\omega)$	Added mass in frequency domain (kg or kg·m^2)
$\boldsymbol{A_r}$, $\boldsymbol{B_r}$ and $\boldsymbol{C_r}$	System identification matrices of the state-space model of radiation forces
Δs	Relative translation (m)
$\Delta \dot{z}$	Relative heave velocity (m/s)
$\Delta \dot{\theta}$	Relative pitch velocity (rad/s)
$\Delta \theta$	Relative rotation (rad)
η, $\dot{\eta}$ and $\ddot{\eta}$	Displacement (m), velocity (m/s) and acceleration (m/s^2) in body-fixed coordinate system
λ	Lagrange multiplier
ω	Angular wave frequency (rad/s)
Ψ	Ending up state
ε_i^j	Wave phase (rad)
φ, θ, and ψ	Rotation in roll, pitch and yaw direction (rad)

List of Nomenclatures

ζ^{A}	Incoming wave amplitude (m)
B_{c}	Damping coefficient of control device (Nms/rad)
B_{d}	Total damping coefficient in declutching control (Nms/rad)
B_{PTO}	Damping coefficient of PTO (Nms/rad)
CWR	Capture width ratio
dt	Time interval (s)
err	Error of performance index
err_{critical}	Critical error of performance index
f^{R}	Wave radiation force (N)
f_{d}	Total damping force in declutching control (N)
f_{e}	Wave excitation force (N)
f_{h}	Hinge force (N)
f_{PTO}	Damping force of PTO (N)
H	Hamiltonian function
h	Water depth (m)
H_s	Significant height of irregular wave (m)
h_{r}	Retardation kernel function
J	Objective functions
K	Stiffness (N/m)
L	Lagrangian function
M	Body mass (kg) or moment of inertia (kg·m^2)

List of Nomenclatures

m	Added mass at infinite frequency (kg or kg·m^2)
N	Number of floating bodies
n	Number of iterations
n_{critical}	Critical number of iterations
P_{PTO}	Average absorption power of PTO (W)
P_{wave}	Wave power (W)
R	Radius from centre of gravity to hinge point (m)
S	Coefficient matrix of constraints
T	Total time length (s)
t	Current time (s)
T_p	Peak period of irregular wave (s)
v_{heave}	Average heave speed of platform (m/s)
v_{pitch}	Average pitch speed of platform (rad/s)
x	System state
x, y and z	Displacement in surge, sway and heave direction (m)
x'	System state considering hinge constrains
3D	Three-dimensional
ATMD	Active tuned mass damper
BEM	Boundary element method
CFD	Computational fluid dynamics
CM	Centre of mass

List of Nomenclatures

CoG	Centre of gravity
DoF	Degree of freedom
FDI	Frequency-domain identification
FPV	Floating photovoltaic
FWT	Floating wind turbine
IRF	Impulse response function
LPT	Linear potential theory
LQR	Linear Quadratic Regulator
MPC	Model predictive control
N-S	Navier-Stokes
PMP	Pontryagin's Maximum Principle
PTO	Power take-off
RAO	Response Amplitude Operator
SS	Semi-submersible platform
STD	Standard Deviation
SWL	Still water line
TLCBD	Tuned liquid column ball damper
TLCD	Tuned liquid column damper
TLD	Tuned liquid damper
TMD	Tuned mass damper
WEC	Wave energy converter

List of Publications

Journal Articles

1. **Yu, S. R.**, Zhang, M.*, Zhang, D. Q., Yuan, Z. M. Optimal Declutching Control of Hinged Multiple Floating Bodies. *Ocean Engineering.* (Submitted in March 2024) (Relevant to Chapter 5)

2. Zhang, M., **Yu, S. R.**, Zhao, G. W., Dai, S. S., He, F.*, & Yuan, Z. M. (2024). Model predictive control of wave energy converters. *Ocean Engineering, 301*, 117430. (Relevant to Chapter 7)

3. Wei, Y., **Yu, S.**, Li, X., Zhang, C.*, Ning, D., & Huang, L.* (2024). Hydrodynamic analysis of a heave-hinge wave energy converter combined with a floating breakwater. *Ocean Engineering, 293*, 116618.

4. Wei, Y., **Yu, S.**, Jin, P., Huang, L., Elsherbiny, K., & Tezdogan, T.* (2024). Coupled analysis between catenary mooring and VLFS with structural hydroelasticity in waves. *Marine Structures, 93*, 103516.

5. Zhang, M., **Yu, S. R.**, Chung, K. S., Chen, M. L., & Yuan, Z. M.* (2023). Time-optimal path planning and tracking based on nonlinear model predictive control and its application on automatic berthing. *Ocean Engineering, 286*, 115228.

6. Zhang, D., Du, J.*, Yuan, Z., **Yu, S.**, & Li, H. (2023). Motion characteristics of large arrays of modularized floating bodies with hinge connections. *Physics of Fluids, 35*(7).

Conference Papers

1. **Yu, S. R.**, Zhang, M., Chen, M. L., & Yuan, Z. M. (2023, June). Pitch Motion Control of Spar-Type Floating Wind Turbines. In *International Conference on Offshore Mechanics and Arctic Engineering* (Vol. 86908, p. V008T09A027). American Society of Mechanical Engineers. (Relevant to Chapter 6)

2. Li, T., Zhang, M., **Yu, S. R.**, & Yuan, Z. M. (2022, June). Real-Time Control of WECs Based on NAR, NARX and LSTM Artificial Neural Network. In *ISOPE International Ocean and Polar Engineering Conference* (pp. ISOPE-I). ISOPE.

Acknowledgements

I would like to express my heartful thanks to my supervisor, Dr Zhi-Ming Yuan, whose kind guidance and expert knowledge have brightened my doctoral life. Dr Yuan is an ambitious researcher and has profoundly influenced me with his insightful thinking and unwavering passion. The most valuable thing I learnt from him was the importance of maintaining motivation towards our goals. His confidence in research and attention to detail in writing are truly admirable. Additionally, his emphasis on the importance of maintaining a work-life balance is worth imitating. The skills and habits I have developed under his supervision will undoubtedly benefit me throughout my career.

I also extend my sincere thanks to Prof Mehmet Atlar, my second supervisor, for his generous assistance. I am grateful to Professors Atilla Incecik, Mehmet Atlar, Chengi Kuo, and Long-Bin Tao, who have influenced me with their academic spirit. I am deeply thankful to Professor Pei-Lin Zhou for his care and support in daily life. I appreciate Professor Erkan Oterkus for his encouragement during my presentations. Special thanks to Dr. Sai-Shuai Dai and Lai-Bin Jia for their frequent communication and guidance.

Dr Ming Zhang has been more than a colleague; his continuous support and valuable advice have been crucial in my research journey. Dr Liang Li has left a precious treasure to me and our group with his contributions. Dr Xiu-Di Ren's assistance in solving a critical software issue was really helpful. Mr Wang Zhao's expertise in designing experimental hardware was immensely beneficial to my project.

I am thankful for the friendship and support of Mr Xiang Li, Dr Yu-Jia Wei, Mr Zhong-Sheng Deng, Mr Yun-Xin Xu, Mr Hong-Bo Hou, Mr Guang-Wei Zhao, Dr Yi-

Han Liu, and Mr Feng-Shen Zhu, who started their PhD journey at the University of Strathclyde with me in the same year. My gratitude extends to my flatmate and colleague, Mr Wen-Xuan Xia, for his kindness. I also cherish the accompaniment of Dr De-Qing Zhang, Mr Bo-Yu Liao, Dr Yang Huang, Mr Yu-Lin Deng, Mr Yin-Hua Liu, Mr Wan-Ru Deng, and Mr Yi Huang, both in academia and in life.

Finally, I am deeply grateful to my family, whose support has been my constant source of strength. To my partner, Ms Lin Yang, whose love is my greatest treasure, I am eternally grateful.

Chapter 1

Introduction

1.1 Background

In deep-sea environments, there is an increasing utilisation of floating structures as devices for harnessing renewable energy. To enhance energy absorption efficiency, a notable trend is designing these devices as floating multi-body systems. This concept is often implemented in the form of hybrid systems or modular configurations. The design of floating multi-body systems includes the integration of Floating Wind Turbines (FWTs) with Wave Energy Converters (WECs), which not only suppress motion but also increase energy capture. Another example is the raft-type WEC, which uses two hinged floaters to harvest wave energy in a wider wave frequency range. Furthermore, the Floating Photovoltaic (FPV) system, employs arrays of floaters to optimise solar energy production by maximising surface coverage. The concept of multiple floating bodies plays a crucial role in the field of ocean engineering and renewable energy.

The control strategies employed in managing multiple floating bodies have a great influence on the motion characteristics and energy conversion efficiency of these systems. The control technology brings more benefits to the system's performance, yet also introduces more complex challenges. Different from a single floating body system, there are hydrodynamic interactions and constraints from connections between multiple floating bodies. Therefore, the motion performance of multi-body floating systems, especially large arrays of floating bodies, is very complex. Moreover, the control of

multiple floating bodies is a challenging task since the control law will influence the multi-body floating system's performance, and vice versa. The derivation of an optimal control command is based on a sufficient number of iterations through an optimisation algorithm.

The control methodologies have evolved from passive control methods to active control methods. Traditional passive control strategies only involve the coupling of an external control device - such as a heave plate, a tuned mass damper (TMD), or a tuned liquid damper (TLD) - to the main body, utilising parameters that are carefully determined to specific scenarios. These strategies provide static or periodic control force to the system. However, real-world applications present complex challenges due to the inherent irregularity of input forces, such as wave forces. Consequently, active control systems, capable of producing effective control forces in dynamically irregular environmental conditions, are deemed essential for modern, efficient system control.

The principal topic of this thesis is to investigate and explore semi-active control methods for managing multiple floating bodies. The optimal control methods we use operate under the assumption that all the input information in the time horizon is fully known. After several iterations of control commands and motion results, an optimal result can be computed according to the predefined optimisation objective. The determination of this objective is inherently dependent on the uniqueness of the application scenario, thus requiring an understanding of the questions in ocean engineering.

As the utilisation of FWTs in deep seas becomes more widespread, strategies to effectively reduce wave-induced motions are essential for the efficient operation and longevity of the turbines.

The wave-induced motion is a high-frequency motion compared to the wind-induced motion. This kind of fore-aft motion can cause large fluctuation in the rotor's relative wind speed and its blade tip speed ratio, and therefore the reduction of the power output. For example, in the case of spar-type FWT, the dominant pitch motion may induce significant bending moments of the tower and potential lubricant leaks. Furthermore, the acceleration at the nacelle should be less than 0.3 g to avoid damage to the power electronics during operation [7].

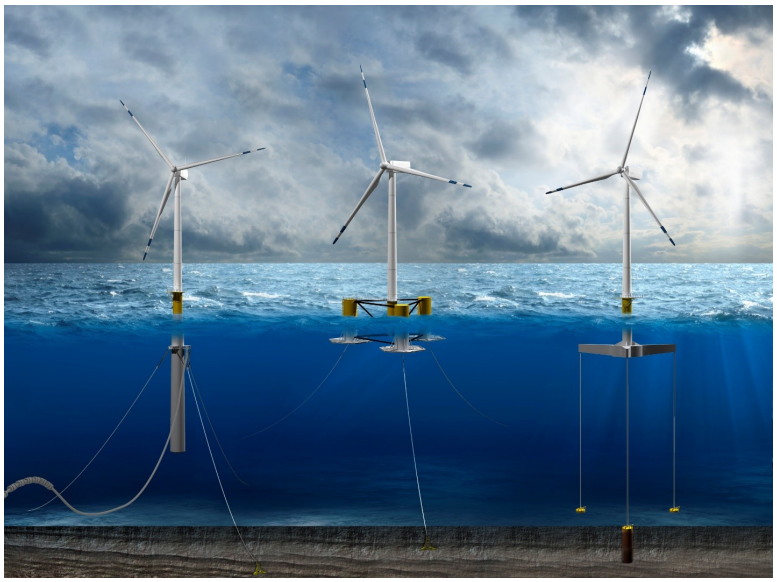

Figure 1.1: Types of floating wind turbines. Left: spar-buoy; middle: semi-submersible; right: tension leg. Copyright: DNV GL

In order to mitigate this motion, wind turbines use active blade pitch control in early time, which changes the attack angle of the blade actively. However, frequent blade pitching is harmful to the wind turbine's bearing and gear system. Furthermore, the traditional blade pitch controller or generator controller of floating wind turbines, though mainly used to regulate the extraction of wind energy and to stabilise the power output, has also been applied to mitigate wave-induced motion. This dual-objective approach, however, involves a trade-off, with the need to balance the weightings of power output stabilisation and motion mitigation.

Therefore, the development of active control strategies employing external control devices has become an increasingly popular method for motion mitigation in FWTs. These technologies offer more targeted and efficient ways to mitigate the wave-induced motion of FWTs without negatively changing the original FWT designs. Various such solutions are being researched, with promising technologies like auxiliary damping systems (TMD and TLD), active fin, and active mooring.

However, the development of most active control strategies requires continuous power input, and the computation of their control laws is often very complex. As such, a simple but effective solution is still a gap in this area, requiring continuous improve-

ments to be made in the design, testing, and implementation of these advanced control devices and methods.

Wave energy converter is another important category of renewable energy devices. WECs are designed to capture the kinetic energy induced by the wave and convert it into electric energy. Although there are various types of WECs, this thesis focuses on the dynamics and control of multi-body WECs. They consist of multiple interconnected floating bodies or structures that respond to the motion of waves.

The prototype of a multi-body WEC is characterised as an attenuator. Attenuators are typically composed of long, multi-segmented floating structures oriented parallel to the wave direction [8]. These segments move and rotate in response to wave excitation. They capture energy from the relative motion of their segments as the waves pass along the length of the device. Attenuators are called so because of their functional characteristic in wave energy conversion: they "attenuate" or reduce the amplitude of the ocean waves as they capture energy from them. In some research contexts, this configuration is also referred to as a "raft-type WEC" or "hinge-barge WEC", representing a horizontal, hinged structure comprising two rafts [9].

The "Pelamis Wave Power" attenuator [10, 11] was one of the most notable devices of this type. It was a snake-like structure composed of cylindrical segments connected by hinged joints. Although the company behind Pelamis is no longer in operation, it was crucial in advancing the technology and understanding of attenuator WECs. Another example of the two-body attenuator is Mocean Energy's Blue Star WEC [12].

The excitation forces from waves generate relative motion between the bodies. This relative motion is usually converted into mechanical energy, and then into electrical energy, through various transduction methods. These could include hydraulic systems, air turbines, or direct-drive linear generators, among others.

A single-body WEC has one main resonance frequency, which matches the natural frequency of the floating body. It's most effective at converting wave energy into electrical energy when the frequency of the incoming waves matches this resonance frequency. If the frequency of the waves is significantly higher or lower, the efficiency of energy conversion drops off. For multi-body WEC, on the other hand, the "resonance

Figure 1.2: The Mocean Energy Blue X wave energy converter. Credit: Colin Keldie, Emec.

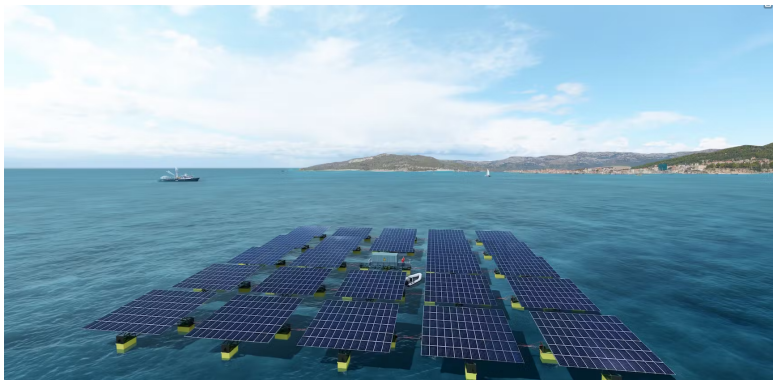

Figure 1.3: Renderings of vast arrays of solar panels (Sun'Sète) floating along coastal southern France. Credit: SolarinBlue.

frequency" of relative motion is not the same as the natural frequency of any single body. It is dependent on all the bodies, and the interaction between them. The design and control of multi-body WECs can be more complex than single-body WECs due to the added Degrees of Freedom (DoFs) and the interactions between the bodies.

1.2 Motivation

The control of multiple floating bodies differs greatly from that of a single body. For a floating body with a connection to the seabed, like single point WECs, latching control can be easily realised by devices like a brake mechanism that can increase the

damping instantly. Nevertheless, it is impossible to provide infinite latching force to floating bodies without connection to the seabed. Therefore, compared to offshore structures with seabed or shore connections, it is more challenging to exert control force on free-floating bodies in deep-sea environments.

One solution is to utilise the wave force on external devices to control the floating bodies. For floating wind platforms, the active control device, such as Active Tuned Mass Damper (ATMD), can be effective in certain scenarios. The raft-type WEC is another example of a floating multi-body system. However, for these floating multi-body structures, the latching control only welds the multiple bodies together, thus it cannot tune the phase of the system. Declutching control currently represents the optimal solution for controlling floating hinged multiple-body systems.

Besides, to minimise or maximise a specific objective in engineering, like minimising the motion of a floating platform or maximising the power extraction of a WEC, using an optimal strategy is necessary.

In this work, a hybrid approach of integrating optimal control and declutching control strategy is deployed to realise the control of multiple floating bodies. The control effects depend on the selection of an objective function in the control strategy. The control effect of this hybrid optimal phase control method has been proven via its implementation in a hinged boxes system, a spar-plate system and a multi-body WEC. This control method can also be applied to a diverse range of floating multi-body systems and application scenarios.

1.3 Research objective

The aim of this work is mainly to develop an optimal control method for multiple floating bodies, which can be implemented in various physical scenarios according to specific objectives. The research targets are listed as follows:

- To build a precise system of equations of motion of multiple floating bodies, considering the hydrodynamic interaction and connection between the bodies.
- To develop an optimal control method for the multi-body system, define spe-

cific objective functions in the control method, which can effectively maximise or minimise our target of motion or power output.

- To verify the effectiveness of the control method in different multi-body systems, especially the new proposed spar-plate system.
- To investigate the energy redistribution in the floating multi-body system.
- To compare different optimisation strategies and improve the performance of the proposed optimal control method.

1.4 Research contents

The thesis involves knowledge from two disciplines: dynamics of multiple floating bodies and control methods. The realisation method of control is also considered.

1.4.1 Floating multi-body dynamics

In scenarios where the turbulence and viscous effects can be neglected, potential flow theory is the most applicable method to describe and analyse the pressure of inviscid, incompressible fluids and wave forces on structures. A boundary element method based on the Rankine source method has been developed to model the hydrodynamic coefficients of multiple floating bodies, including the wave excitation force, added mass, and radiation damping of each single body, and those parameters among the bodies. With these frequency-domain hydrodynamic coefficients, a multi-body, multi-DoF time domain motion equation can be constructed to describe the system in waves.

1.4.2 Multi-body mechanic connection

Compared to the hydrodynamic coefficients, the mechanical interactions of the floaters have a more direct impact on the performance of the connected floating bodies. The constraints among these devices can significantly change their responses. If there are mechanical connections among the multiple floating bodies, a constraint equation needs to be built. For ball joints, each connection will constrain the relative motion

in 3 DoFs; for universal joints, each connection will constrain the relative motion in 4 DoFs; for hinge joints, each connection will constrain the relative motion in 5 DoFs. A commonly used method is to write the restraints as a constraint matrix and couple it with the multi-body motion equation.

1.4.3 Semi-active control

Semi-active control is widely utilised in civil engineering for vibration control and in ocean engineering for energy management of WECs. Drawing inspiration from these applications, this concept is adapted to the control on the dynamics of multiple floating bodies. A notable advantage of semi-active control, particularly declutching control as demonstrated in this study, is its effective control performance at a low cost. Additionally, the inclusion of auxiliary structures within the control strategy enables the harnessing of wave energy to control wave-induced motions, further enhancing the system' s efficacy.

1.4.4 Optimal control

The optimal control is realised by Pontryagin's Maximum Principle (PMP). When the initial and end states are determined, PMP is able to derive an optimal trajectory between the states that maximises or minimises the objective function. In this thesis, the states are the motions of the multiple floating bodies, and the objective functions are related to both motion (η, $\dot{\eta}$, or $\ddot{\eta}$) and time horizon T.

To realise optimal control, the input information from waves over the entire time horizon is assumed to be known.

1.5 Main contributions

The main contribution of this thesis is to develop a novel optimal phase control method based on various objective functions for multiple floating bodies. Previous control methods focus on the performance of a single floating body, and the external control devices require external power input. This thesis builds a new multi-body

control theory that controls the performance of the system by tuning the phase of wave forces on different floating bodies.

A key advantage of the proposed method is that it does not require additional power input, as it harnesses the wave energy present in the system. The auxiliary device extracts the mechanical energy from the primary floating body to reduce its wave-induced motion, and transfer the mechanical energy into electric energy at the same time. This is a significant difference from the high-cost active control methods that typically rely on external power sources. This idea is in-sighted from "Jie Li Da Li" in Tai Chi Chuan, which means "Using your opponent's force against them" .

Moreover, our approach enables phase control, which can be realised by opening or closing a valve within the multi-body system. This allows for precise tuning of the wave force acting on the bodies, resulting in more effective motion control, and minimal power demand. Furthermore, the extra power generated by the power take-off (PTO) system can be stored and utilised for other purposes.

1.6 Thesis structure

The outline of each chapter in this thesis is listed as follows:

- Chapter 1 Introduction
  Introduce the inspiration and formation of the idea of floating multi-body control. The mainly used research methodologies are also briefly mentioned.

- Chapter 2 Literature Review
  Summarise and review the previous research for multiple floating bodies, control methods of floating bodies, and applications of floating multi-body control. Emphasise the gap of control of multiple floating bodies in existing research.

- Chapter 3 Dynamic Model of Multiple Floating Bodies
  Give a complete mathematical model of multi-body motion equation in ocean engineering. The water surface memory effect, constraint matrix, and linearised representation are considered herein.

- Chapter 4 Control Algorithm of Multiple Floating Bodies
  Introduce the algorithm of optimal control applied on multiple floating bodies.

- Chapter 5 Optimal Phase Control Method of Multiple Floating Bodies
  Apply optimal control and declutching control to the motion of multiple floating bodies. Develop an optimal phase control method based on various objective functions.

- Chapter 6 Motion Control of Multiple Floating Bodies
  Demonstrate and analyse the control effect in a case of minimising the motion of floating structures.

- Chapter 7 Control of Multiple Floating WECs
  Demonstrate and analyse the control effect in a case of maximising the power output of a multi-body WEC system.

- Chapter 8 Conclusions and Future Work
  List conclusions of this thesis and potential future discussions.

Chapter 2

Literature Review

The review chapter provides a detailed exploration of the developing history and current state-of-the-art within the scope of this thesis. Structured as a multidisciplinary research, the chapter has two primary sections: a review of the hydrodynamics of floating multi-body systems, and a review of various control methodologies for these floating bodies. The review of control methodologies is also divided into two distinct sections: control strategies and control algorithms, including an examination of both semi-active control methods and optimal control techniques.

2.1 Multiple floating bodies

Before discussing control methodologies, it's essential to first understand the dynamics of multiple floating bodies. Despite there are various types of floating multi-body systems, they all fundamentally follow a consistent form of governing equations. The main characteristic related to the dynamics of these floating multi-body systems is the consideration of the interaction among bodies. Such interactions can be induced by different factors: hydrodynamic interactions due to diffraction or radiation effects and mechanic constraints due to rigid connections.

2.1.1 Types of floating multi-body system

Nowadays, many renewable energy systems have been designed as floating multi-body systems from both practical and efficiency considerations. Based on their functional applications, floating multi-body systems investigated in this thesis can be categorised into three primary types:

- Floating Platforms with Auxiliary Infrastructure

  These systems mainly serve as offshore operational bases or substructures of wind turbines. Their primary engineering objective is to ensure the stabilisation of the core structure - platform - particularly under dynamic marine conditions, thereby ensuring operational safety and power generation. Combining different types of renewable energy systems (e.g., wind and wave energy converters) in a single floating platform can lead to more efficient energy capture. For example, the Spar-Torus Combination concept [1] integrated spar-type FWTs and Torus-shaped WECs for a lower capital cost. However, the combination increases the wave-induced heave motions of the spar due to increased wave forces on the system.

- Wave Energy Converter Arrays

  These energy harvesting devices are designed to harness the kinetic and potential energy from ocean waves. The objective of controlling WECs is to enhance their total energy extraction efficiency, thereby maximising their net power output. The typical concept of a WEC array is Pelamis [10, 11], a long, slim, semi-submerged structure composed of cylindrical sections linked by hinged joints. The wave-induced relative motion at the joints between the sections pumped the hydraulic rams back and forth, driving hydraulic motors which in turn powered electrical generators.

- Floating Photovoltaic Systems

  Floating systems can be designed modularly, allowing for separated manufacture and scaling up as demand or technology evolves. A popular concept in recent years is the Floating Photovoltaic System, buoyant solar panel arrays designed

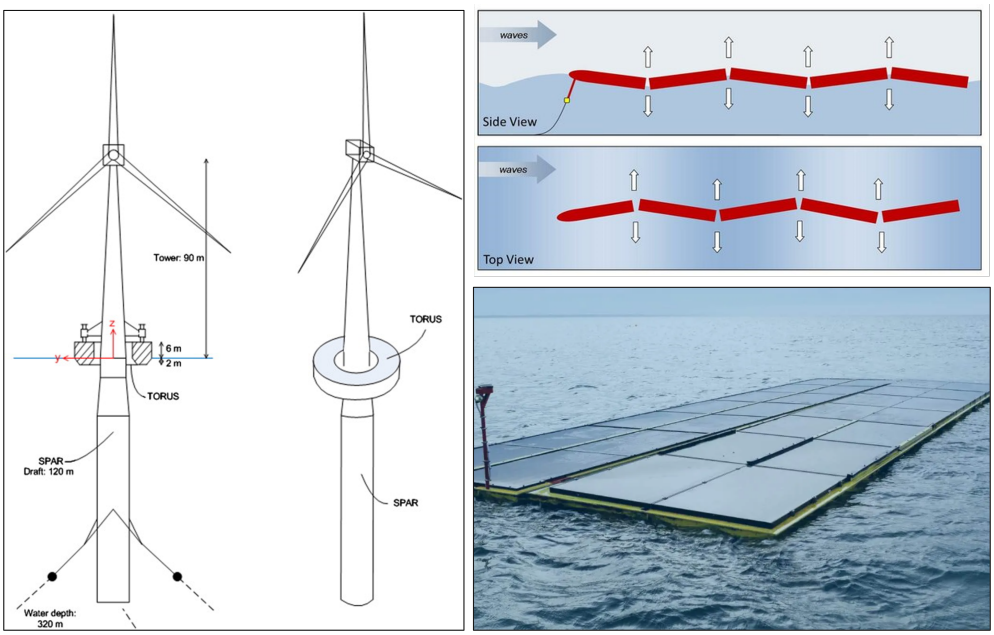

Figure 2.1: Left: Conceptual sketch of the combined concept "STC" [1]. Upper right: Operation sketch of Pelamis (Source: Pelamis Wave Power) [2]. Lower right: The FPV panels installed at the Dutch North Sea.

to gather solar energy. The stabilisation of the overall motion dynamics of the photovoltaic panels is crucial, because it not only ensures the longevity of the panels but also amplifies their effective solar exposure area. The project "Zon-op-Zee (Solar-at-Sea)" is the world's first offshore floating solar farm in the Dutch North Sea.

These structures are composed of individual floating bodies, commonly with connections among them. Their dynamic behaviours under operational conditions are affected by the hydrodynamic interactions with the surrounding waves or between the bodies. Accurately calculating hydrodynamic interactions is crucial in ensuring precise simulation of the multi-body dynamics involved.

2.1.2 Multi-body hydrodynamic interaction

The motions of multiple floating bodies are mainly excited by the wave on the water surface. Thus, wave-structure interaction is a crucial aspect of this study. Computational Fluid Dynamics (CFD) and Linear Potential Theory (LPT) are two mainstream

adopted to address the hydrodynamic responses of multiple floating bodies. CFD approach describes the fluid dynamics around a floating body by solving Navier-Stokes equations, which consider the nonlinearity of wave-structure interactions in the system. However, in practical applications, the expensive computation resources are a huge block to realise optimisation and control by CFD method. In this thesis, the focus is only on LPT which simplifies the N-S equations by removing the viscous and the high-order terms.

Under the presumption of an ideal fluid, the fluid field is described by velocity potential, which satisfies the Laplace equation. The solution of velocity potential is regarded as a boundary value problem. Velocity, pressure and force are derived from the velocity potential. The LPT has a fast speed of computational analysis because the numerical iteration depends on the scalar variable, ϕ. In the well-established field of LPT, a range of commercial software has been developed to analyse the hydrodynamic behaviour of floating bodies, including ships or platforms. For example, HydroD computes hydrodynamic coefficients and response amplitude operators (RAOs) in the frequency domain, while SIMA presents the response of the structure in time domain analysis.

Some researchers have explored the dynamics of single or two floating bodies based on potential flow theory. Faltinsen [13] provided an overview interpretation of the boundary element method and how it was applied in the calculation of motion responses of ship and platform. Linear loads, nonlinear loads, environmental loads, viscosity effects, and stationkeeping problems are discussed in sea waves in detail. Newman [14] showed the expressions of ship responses in waves and excitation force under the ideal fluid assumption. Cummins [15] incorporated the fluid memory effect into the time-domain motion equation of a floating body. He employed an Impulse Response Function (IRF) to represent the radiation effect stemming from body movements. The radiation force acting on the floating body is formulated as the wave memory effect whose expression is a convolution term of velocity. The impulsive motion of one body can influence neighbouring bodies. This is the radiation interaction between multiple floating bodies, which also contributes to their added mass and radiation damping.

Masubuchi and Kawatani [16] analysed the frequency-domain response of a two-body WEC with rigid connection in regular waves. Hydrodynamic interactions and different configurations of the two-body system are considered in their research.

Further research was undertaken to thoroughly investigate the dynamics of multiple floating bodies. Choi and Hong [17] used a high-order boundary element method (BEM) to compute the hydrodynamic parameters of floating multi-body and compared the numerical results with model test results. The results both showed that the hydrodynamic parameters of a floating multi-body system are very different from a single floating body due to the interaction between bodies. Yuan *et al.* [18] developed a 3-D Rankine source method to investigate the hydrodynamic interactions between two travelling ships. Their computational results gave good agreement with the experimental results conducted by Kashiwagi *et al.* [19]. Zhang *et al.* [20] extended Yuan's method [18] by introducing a cut-off radius to analyse the radiated hydrodynamic coefficients of a multi-box array. Their numerical results showed that it is feasible to model the hydrodynamic properties of large arrays of floating bodies. The cut-off range method significantly reduces computational time when simulating the interaction between multiple floating bodies.

A thorough study of the motion characteristics of these floating multi-body systems, especially under the influence of control algorithms, is of great importance. Such knowledge could greatly accelerate the industrialisation and wider adoption of these devices.

2.1.3 Multi-body mechanical connection

The primary objective of this thesis is to explore energy conversion within floating multi-body systems. Consequently, the discussion is confined to mechanical joints, which are designed to transfer loads, moments, and energy between the bodies without significant deformation. Typical mechanical connectors are rigid connectors and flexible connectors [21]. In rough sea conditions, rigid connection carries the wave load because the connectors completely fix two adjacent modules. As a result, this creates a large bending moment at the connector, therefore, rigid connectors have been gradually

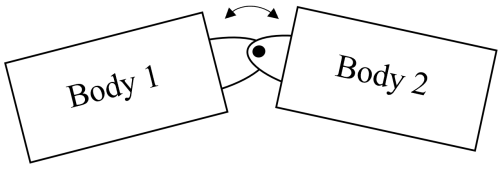

Figure 2.2: Typical hinge (articulated) connection.

abandoned. A typical example of flexible connectors in engineering applications is the hinged connection, or well-known articulated connection. The simplest articulated connectors used horizontal peg hinges and docking probes to allow only relative pitch motion between adjacent floating bodies [22].

Published studies have proposed several methods for solving the motion responses of hinged multi-body systems. In 1984, Langley [23] utilised the constraint matrix method in multi-rigid body dynamics. The structure is assumed to have rigid components and a linearised frequency domain analysis method is used. Newman [24] took hinge constraints into consideration in multi-body problems in the frequency domain. He utilised a mode generalised method to predict the vertical motion and relative rotation of a hinge in a two-barge system. Sun *et al.* [25] applied the Lagrange multiplier technique to investigate the same interconnected barge configuration. They compared their numerical results with Newman's results and got a good agreement. Zheng *et al.* [26] used the method of introducing a constraint matrix in the frequency-domain dynamic equation to calculate the motion results. Their results also agreed well with the results from Newman's method [24].

While frequency-domain methods provide responses based on frequency analysis, they are short in capturing the complexity of wave-body interactions when control actions are introduced. In contrast, time-domain analysis can address these complexities, leading to its increased usage in recent research. Among the current methods employed for hinged multiple floating bodies, the Constraint Matrix Method can reduce the order of the system matrix, avoiding computational non-convergence in the time domain. Thus, this thesis selects the Constraint Matrix Method as the approach for solving the fluid-structure coupled dynamic analysis of hinged multiple floating bodies.

In systems where multiple floating bodies are connected, either rigidly or via moor-

ing lines, the radiation interactions can lead to additional stresses and loading on the connecting components. However, these structure stresses are not included in the discussion of this thesis, as the primary focus is hydrodynamics.

2.2 Active and semi-active control technology

The implementation of appropriate control algorithms significantly enhances the performance of floating multi-body systems. This is true even in the case of a single floating body, such as a FWT or a ship, where adding supplementary structures can transform the system into a multi-body configuration. Emerging control concepts mainly include three types of control systems: passive control, active control, and semi-active control [27]. Passive control strategies, while economical, require precise tuning and may not be always effective across varying wave conditions. Active control methods, on the other hand, are known for their high-level control effect but are often energy-intensive. This thesis focuses on the declutching control strategy, a form of semi-active control widely adopted in vibration control applications. This method combines the advantages of both passive and active controls, utilising the wave forces acting on different bodies to resist motion or amplify power absorption.

2.2.1 Structural control for FWTs and ships

The control objective of FWTs and ships is to stabilise their motions. Traditionally, researchers focused on optimising the shapes of floating bodies and implementing passive control methods to reduce wave-induced motions. Fixed heave plate can provide additional added mass and suppress the heave and pitch motion of floating bodies [28–30]. Helical strakes are designed to suppress vortex-induced vibration [31–34]. Truss spar is a concept designed to increase the effective vertical mass and heave damping of the structure, and hence reduce the motion of floating platforms [35, 36]. However, the effect of designs depends on the floating structure geometry and the excitation force conditions. Additionally, the shape optimisation process can be computationally expensive, as it often requires extensive simulations and iterative refinement.

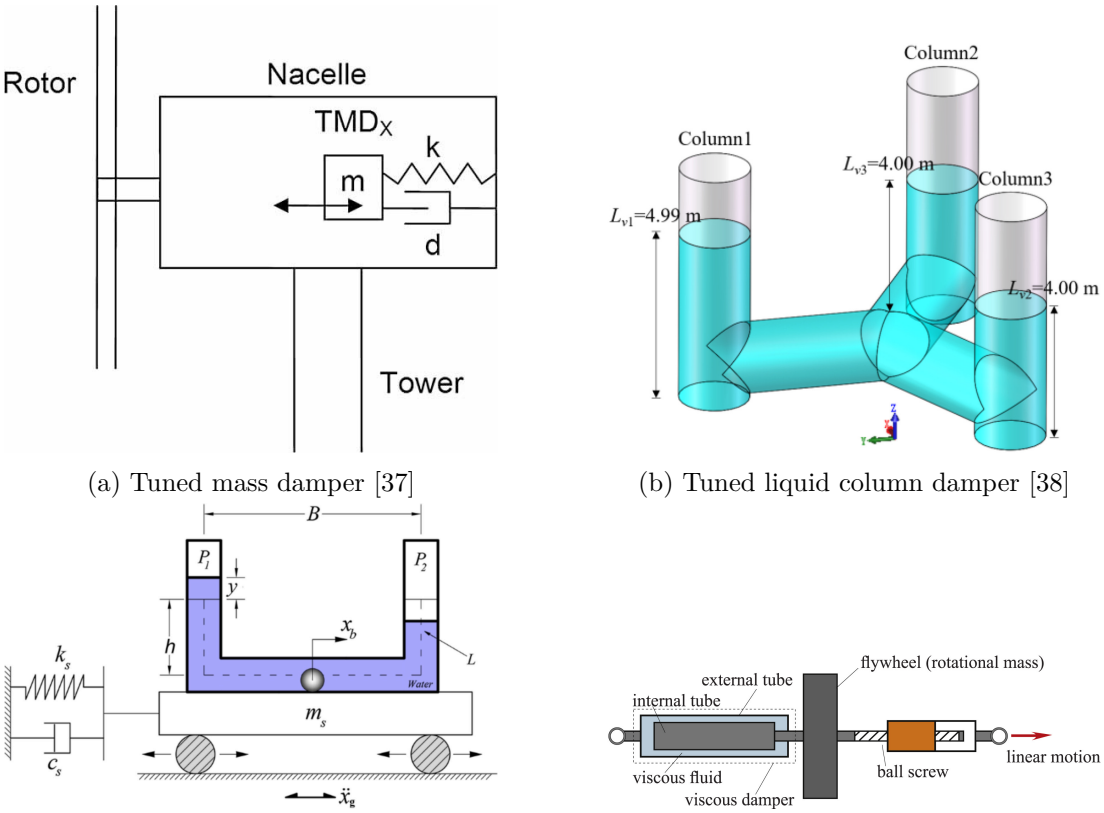

(a) Tuned mass damper [37]

(b) Tuned liquid column damper [38]

(c) Tuned liquid column ball damper [39]

(d) Inerter-tuned mass damper [40]

Figure 2.3: Passive vibration control technologies.

Passive control methods also have been widely employed to reduce wave-induced motions, but their effectiveness varies depending on the application. Passive control methods, such as movable heave plates, mooring systems, tuned mass damper (TMD), tuned liquid column damper (TLCD), and tuned liquid column ball damper (TLCBD) [37–39], can be effective in certain scenarios. The inerter-tuned mass damper is another technology for FWT vibration control which outperforms the classic TMD [40]. However, their performances are highly sensitive to the wave conditions and are only effective in a narrow wave bandwidth.

Active control methods are state-of-the-art solutions to reduce wave-induced motions in floating structures. Blade pitch control is one of the typical active control methods for floating wind turbines to regulate the extraction of wind energy and reduce the fluctuation of power output. It can also be applied to mitigate waved-induced

motion, though has to balance the weightings of the two objectives. Moreover, such a method that relies on modifying the aerodynamic lift on the blades is incapable of operating during shutdowns due to extreme events when load mitigation may be most critical. Furthermore, wave frequency is much higher than the frequency that wind speed or wind direction changes. Frequent blade pitching is harmful to the rotor's gear and bearing system. This situation primarily impacts the blade loads [41] and leads to negative damping of the platform-pitch mode [42].

Some other active control methods using additional structures are proposed for floating structures' motion control, including active dampers, active moorings, active vertical vanes, and gyroscopes [43–46]. The implementation of these active control methods can require complex control algorithms and hardware, potentially increasing the overall cost and maintenance requirements of the system. Perez [47] did seminal research on the roll stabilisation with rudder and fin. Cakici *et al.* [48] considered the amplitude and rate saturation of the pair of fins in the reduction of the roll motion and acceleration of a ship. Hu *et al.* [49] combined Model Predictive Control (MPC) with gyrostabiliser to achieve real-time ship roll control. While these technologies have demonstrated their ability to improve motion control, they often necessitate additional power input, resulting in increased energy consumption [50].

In this thesis, we propose a novel approach that utilises wave energy as the power input to control the floating platform's motion induced by waves, thereby minimising and even eliminating the need for extra power input. The proposed method involves connecting another floating device to the primary floating body, creating a multi-body system that can be actively tuned to effectively reduce the motion of the primary floating body. The detailed concept designs and results are shown in Chapter 6. This is achieved through the implementation of an optimal declutching control method that tunes the wave force acting on the bodies, ultimately reducing the motion experienced by the primary floating body. The proposed multi-body control method can be regarded as a semi-active method, which controls some tunable parameters (e.g., stiffness and damping) without needing as much energy input as active systems.

A key advantage of the proposed method is that it hardly requires additional power

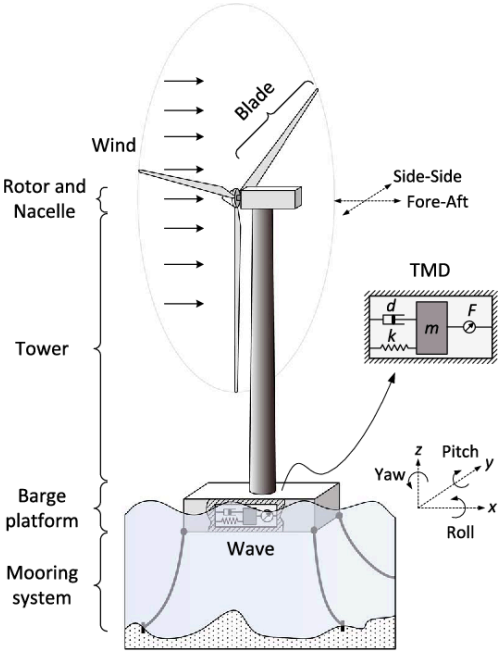

(a) Active mass damper [43]

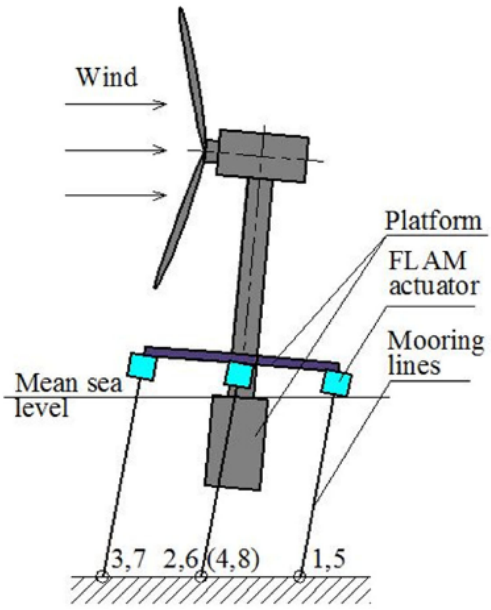

(b) Active moorings [44]

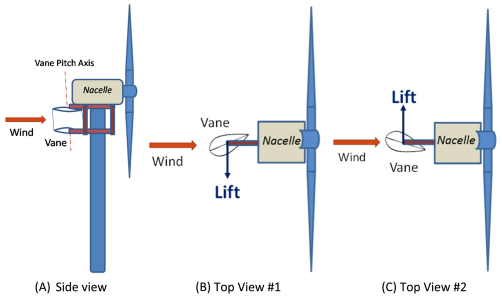

(c) Active vertical vanes [45]

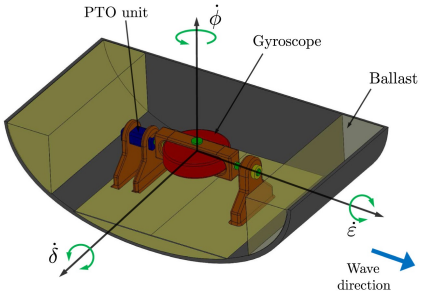

(d) Gyroscopes [46]

Figure 2.4: Active vibration control technologies.

input, as the device harnesses the wave energy present in the system. The auxiliary device extracts the mechanical energy from the primary floating body to reduce its wave-induced motion, and transfers the mechanical energy into electric energy at the same time. This is a significant difference from the high-cost active control methods that typically rely on external power sources. Moreover, our approach enables phase control, which can be realised by opening or closing a valve within the multi-body system. This allows for precise tuning of the wave force acting on the bodies, resulting in more effective motion control, and minimal power demand. Furthermore, the extra

power generated by the PTO system can be stored and utilised for other purposes.

2.2.2 Phase control for WEC

Phase control refers to a semi-active control strategy commonly used in the operation of WECs to optimise their energy capture from ocean waves. This concept is extended in this thesis, representing a strategy that can tune the phase between forces and motions to realise different objectives in control.

Phase control includes latching control and declutching control, as shown in Fig. 2.5. It is a kind of on/off PTO control, implemented either through a braking mechanism, called latching control, or through a bypass valve, called declutching control. In summary, the range of the PTO damping coefficient for latching control can vary from B_{PTO} to positive infinity, symbolised as $[B_{\mathrm{PTO}}, +\infty]$. Conversely, for declutching control, the range is confined between zero and B_{PTO}, represented as $[0, B_{\mathrm{PTO}}]$.

The latching control works by locking and releasing the PTO system occasionally. By controlling the phase between the velocity and the wave force, the wave force is always accelerating the floater and thereby the energy absorption reaches the optimal value. The concept of latching control was initially introduced by Budal and Falnes [51].

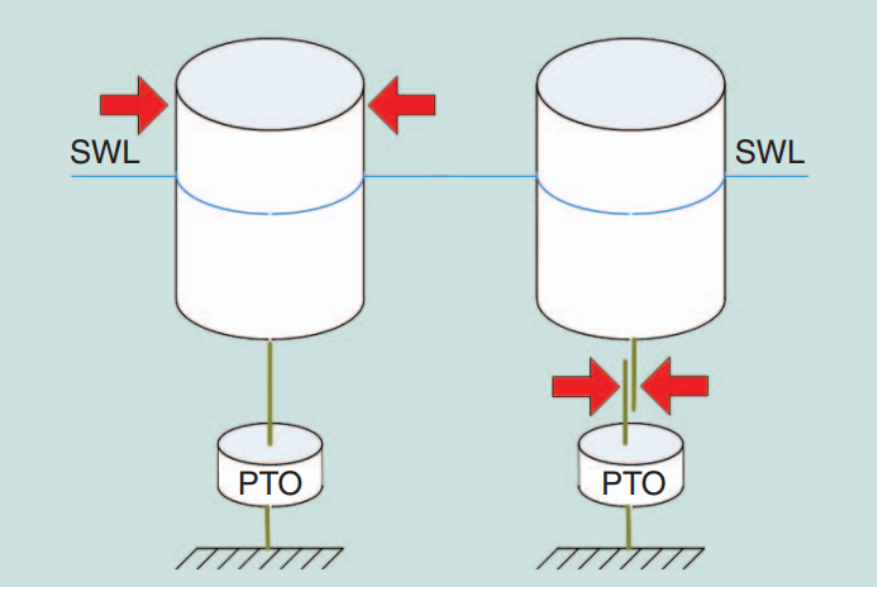

Figure 2.5: Left: latching control; Right: declutching control [3].

In a related study, Greenhow and White [52] explored the correlation between energy absorption and the duration of latching in regular wave scenarios. However, research in the field of WEC's latching control has involved diverse optimisation strategies. As noted by Hals *et al.* [53], while some studies emphasised optimising latching duration [52,54], others focused on fine-tuning the phase difference between the peak of wave force and the WEC's velocity. In a comparative analysis, Babarit *et al.* [55] reviewed various latching control strategies for WECs operating in random sea conditions. The effectiveness of latching control was further evaluated by Babarit *et al.* [56], who applied the optimal command theory based on pre-generated wave elevations to gain the optimised control commands. Since infinite latching force is impractical in real-world applications, Falcão *et al.* [57] introduced an alternative called "load control" through the implementation of a high-pressure hydraulic PTO system. This system provides a natural way to achieve latching: the body remains static as long as the hydrodynamic forces acting upon its wetted surface are insufficient to overcome the resistance force. This resistance is the product of the gas pressure differential and the cross-sectional area of the ram. In the field of multi-body WECs, Zheng *et al.* [26] carried out a time-domain analysis of a raft-type WEC to investigate the mechanism and effect of latching control. They compared the parameters of the cylindrical raft and the PTO damping coefficients to maximise the power capture. Even at optimal parameters and damping coefficient, there are phase lags between wave excitation moments and velocities in the pitch direction. These lags can be eliminated by non-uniform mass distribution or latching control in certain wave conditions.

Declutching control is a necessary solution to complement the latching control for multiple floating bodies, and is typically implemented in conjunction with PTO systems. The concept of declutching control or unlatching control was introduced in Salter's work [58] as a complement to latching control. The declutching control means switching on and off alternatively the by-pass valve in the circuit of the hydraulic cylinder. When declutching happens, the by-pass valve is switched on and the damping force is set equal to 0. This control approach is known as "bang-bang control" or "on-off control". Babarit *et al.* [59] compared declutching control with pseudo-continuous control,

a method realised by deploying several hydraulic cylinders and/or several high-pressure accumulators with different pressure levels in the PTO system. Declutching control is proven to have even higher energy absorption while its control device is simpler. After comparing different control strategies for a sphere WEC, Hals *et al.* [60] also determined that latching and declutching control strategies are attractive because of their simplicity and because they do not require additional energy input. In the research of Zhang *et al.* [61] on a hemispherical WEC, the amplification ratio of absorbed power by declutching control is less than 1.1. It indicates that declutching control is inapplicable for oscillating WEC in proposed wave frequencies in this research. The analysis of declutching control on a single body shows a distinct relationship with wave frequency, which may vary in the case of multiple floating bodies.

Pelamis [10, 11] was designed to absorb wave energy from the rotational motion between 4 to 5 tube segments and its dynamics show good energy capture efficiency and extreme wave condition resistance. The control algorithms allow the performance improvement of multiple floating bodies in the time domain. Li *et al.* [62] implemented a real-time declutching control to a bi-oscillator WEC to enhance power capture. This research focuses on the implementation of the developed wave force prediction algorithm based on artificial neural networks and power extraction. The power absorption is significantly enhanced; however, the motion of the outer oscillator is not well analysed. Liu *et al.* [63] proposed a discrete control method based on discrete control force by switching the valves in the hydraulic PTO system. The combination of declutching control and load control shows a good performance enhancement in the entire wave bandwidth. In research applying declutching control to the multi-body systems, the main purpose is to maximise the electric power generation of WEC. In this thesis, however, more physical scenarios and objectives are applied to the control of multiple floating bodies, such as the stabilisation of a floating platform or relative motion reduction between solar panels.

2.3 Optimal control

2.3.1 Methodologies in optimal control

The optimal control method includes control strategies that optimise specific performance indices under given constraints. The motivation for introducing optimal control to our method is its ability to determine the control inputs that will guide a system from an initial state to a desired final state while minimising or maximising a certain performance index, such as cost, energy, time, or a combination of these factors. Mainstream methodologies in optimal control include:

- Pontryagin's Maximum Principle (PMP) [64]
  PMP is a fundamental principle in optimal control, providing necessary conditions for optimality. It is particularly useful in problems where the control actions are bounded.

- Dynamic Programming
  Dynamic Programming was developed by Richard Bellman [65]. This method solves complex problems by breaking them down into simpler sub-problems. It's particularly effective for multi-stage decision processes.

- Linear Quadratic Regulator (LQR) [66]
  Used for linear systems with quadratic cost functions, LQR provides an efficient way to calculate optimal control laws.

- Model Predictive Control (MPC)
  MPC is a more modern approach where a model of the system is used to predict future states and optimise control actions over a moving time horizon. It relies on prediction technologies to realise real-time control.

The core of an optimal control problem is the objective function, a mathematical expression that quantifies the goal of the control. The control actions are subject to constraints which might include physical limits of the system, environmental conditions, safety requirements, or operational limits. These parameters are subject to definition

by the controller designer. Control variables are the inputs or actions that can be manipulated to control the system, which is mainly provided by the PTO force in many WEC systems. State variables represent the system's current status, and their evolution over time is typically governed by the system's motion equations.

As computational capabilities advance, optimal control methods are able to handle high-dimensional systems and nonlinear dynamics. In recent years, the field has further integrated with emerging areas such as machine learning, autonomous systems, and renewable energy management. Our method can also be integrated into a real-time control framework in the future.

2.3.2 Application of Pontryagin's Maximum Principle

Pontryagin's Maximum Principle (PMP) [64] is highly suited to the nature of our research problem and robust enough for our analysis. It is a powerful tool in optimal control theory that is widely used to find the optimal control inputs that minimise or maximise objective functions. Objective functions represent the objectives that are being optimised. In this research, PMP is employed to solve the control commands that result in a minimum motion of floating bodies or a maximum power absorption of PTO devices over a given computation period.

This principle provides a necessary condition for an optimal control problem to have an extremum. PMP is good at determining the optimal control strategy that will maximise or minimise a given performance index for a dynamic system. The principle, fundamentally mathematical, finds its roots in the calculus of variations [67] and Hamiltonian formulation. It involves the introduction of co-state variables and the Hamiltonian function, offering a systematic approach to handling constraints in dynamic systems. PMP's most significant contribution lies in its ability to handle complex systems that traditional methods fail to solve, particularly in nonlinear and time-dependent scenarios. Compared with other optimal control methods based on it, PMP is potentially more computationally efficient in that the conditions which it specifies only need to hold over a particular trajectory.

Guided by the PMP, the computation of optimal control follows a specified pro-

cedure. First, a Hamiltonian function, denoted as H, is formulated. This function depends on the system states and the co-states. The co-states are introduced to address the constraints within the problem. Subsequently, the conditions for optimality are deduced by calculating the partial derivatives of H with respect to the system states, co-states, and the control variable. These derivatives are expected to converge to zero at the point of optimal solution.

In Ocean Engineering, PMP has been widely applied to the optimisation of WECs, where it is used to maximise energy extraction efficiency. In regular waves, it is possible to use the analytical solution of WEC's motion equation in the time domain to compute the optimal delay of latching control. However, as Hoskin *et al.* proposed in [54], the above semi-analytical method cannot be applied in irregular waves. Babarit and Clément [56] implemented the optimal command theory based on a Hamiltonian formulation and PMP to realise the latching control of WECs in irregular waves. This method is proven effective in generating optimally controlled time domain sequences of the WEC motions in a random sea. Cândido *et al.* [68] further extended the research to evaluate the performance of two-body devices in real wave conditions. He also employed a latching control strategy based on PMP to the control strategy. While significant improvements in power absorption were observed in regular waves, the enhancement was limited in irregular wave conditions. Their finding proves the combination of latching control and PMP is not suitable for floating multi-body systems in certain wave conditions. However, Liu *et al.* [69] found the latching control based on PMP can significantly improve power capture of the raft-type WEC both in regular and irregular waves. Specifically, in regular waves, the benefit brought by latching control depends on the wave period, while in irregular waves it mainly depends on the peak wave period.

PMP has the potential to be integrated into the framework of Model Predictive Control (MPC), relying on the development of real-time sea wave prediction methods. Li *et al.* [70] described an approach to predicting short-crested waves, necessitating the use of remote sensing technologies, including Light Detection and Ranging (LIDAR) [71], or an array of wave buoys. Real sea wave data was employed in their research for optimal control; however, it is crucial to clarify that these were not predicted data. Different

from the dynamic programming Li used, Henriques *et al.* [72] applied a Discontinuous Galerkin (DG) finite element time-stepping method for the numerical solution of control problems within the framework of PMP. In the optimal latching (bang-bang) control of a floating oscillating water column WEC equipped with a self-rectifying air turbine, the results showed that the DG method is an efficient alternative to the well-known Pseudo-Spectral methods. Henriques *et al.* [73] also successfully implemented a receding horizon latching control strategy of the oscillating-water-column WEC and validated its effect experimentally. Also, the sensitivity of the PTO power output to receding horizon time intervals was evaluated. Wu *et al.* [74] applied a PMP-based real-time latching control strategy in irregular waves to the solo Duck WEC. As stated in their research, the short-term prediction of excitation force can be realised by the Fast Fourier Transform (FFT) or Deterministic sea-wave prediction (DSWP) [75, 76]. However, the prediction of excitation force in the near future is still a challenge in practice because of the inherent deficiency of the prediction methods. Addressing this challenge, Li *et al.* [77] developed and trained a multi-layer artificial neural network to forecast the short-term wave forces, which realised the practical implementation of wave energy control. They also applied this real-time discrete control algorithm to a bi-oscillator WEC to enhance the power capture [62].

In this thesis, we expand the application scope of PMP from its conventional usage in WECs to a variety of scenarios within the renewable energy domain. The thesis includes several practical case studies which analyse the system of hinged boxes, FWT platform with auxiliary structure, and multi-body WECs. Within these studies, control strategies based on PMP are implemented and tested through numerical simulations.

2.4 Summary

This chapter comprehensively reviews the floating multi-body systems and their associated control methodologies, tracing developments from the seminal work to recent research. The numerical methods for describing the hydrodynamics of multiple floating bodies have evolved in response to academic and industrial demands. Despite these

developments, a noticeable gap exists in the control strategies for such systems. Among the existing methods for controlling floating bodies, phase control, which tunes the phase between waves and the floating body's motions, stands out as both effective and economical. The strategy adopted for implementing phase control in this context is within the optimal control framework, aimed at optimising a predefined objective function over a specified time horizon. In pursuit of simplicity and effectiveness, this thesis employs Pontryagin's Maximum Principle as the foundation for optimal control.

Chapter 3

Dynamic Model of Multiple Floating Bodies

3.1 Introduction

This thesis simplifies the general concept of multiple floating bodies into an N-body array where only the interactions between adjacent bodies are considered. In practical application scenarios, N is set to be 2. The characteristics of the fluid and structure are addressed with potential flow theory. Potential flow theory is suitable for describing the motion of structure in waves with the assumption that fluid is inviscid and irrotational. By ignoring viscosity, potential flow theory simplifies the governing equations of fluid dynamics (the Navier-Stokes equations) into a linear problem. While this is a large simplification, potential flow theory can accurately predict many flow phenomena, particularly those in which viscous effects are negligible or occur in a small region.

This chapter develops a dynamic model of multiple floating bodies. The bodies are assumed to be rigid throughout the whole thesis. The frequency-domain hydrodynamic coefficients are acquired from a commercial software WADAM [78] using panel method. The hydrodynamic coefficients include the wave forces, added mass, and radiation damping related to the wave frequency. The wave diffraction effect is reflected in

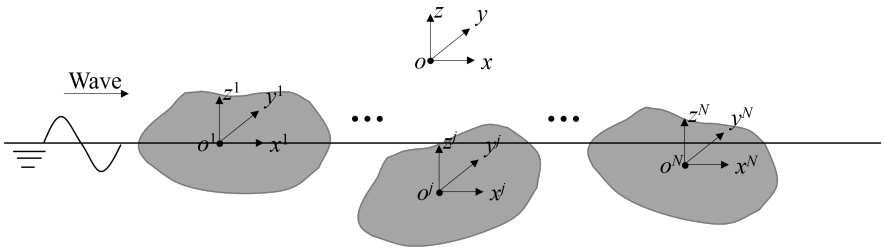

Figure 3.1: Configuration of multiple floating bodies.

the wave forces, and the wave radiation effect between bodies is reflected in different added mass and radiation damping matrices. With these coefficients, a time domain motion equation can be established in Matlab to solve the motion of each floating body in each DoF. Impulse response function (IRF) is used herein to represent radiation force induced by the memory effect of water surface. The equation can be linearised to first-order differential equations when written in a state-space representation. The convolutional term representing the radiation force can also be linearised with the state-space representation.

3.2 *N*-body time-domain hydrodynamic model

For a multi-body floating system, the dimensions of the mass matrix, motion vector, and force vector are $6N \times 6N$, $6N \times 1$, and $6N \times 1$ respectively, where N is the number of bodies. The theoretical model of N floating bodies is depicted in Fig. 3.1. The global coordinate system $o-xyz$ is a right-handed Cartesian coordinate system with $x-y$ axes in the horizontal water plane and z axis oriented in the upward direction. Each body can be simplified as a mass point at its centre of gravity (CoG). The surface memory effect related to the shape and velocity of a floating body is described by added mass and damping coefficients. The hydrodynamic parameters and motion responses are described in body-fixed coordinate systems $o^j - x^j y^j z^j$, where j corresponds to the j-th body.

Assuming the flow field is ideal, potential flow theory is applied to derive the hydrodynamic parameters of the floating bodies. The water depth, h, is assumed to be

infinite as the effect of seabed is not considered, and waves are propagating towards positive x-axis throughout the computation. When considering the wave surface memory effect, the time-domain motion equation of multiple floating bodies in regular wave is,

$$(\boldsymbol{M}+\boldsymbol{m})\ddot{\boldsymbol{\eta}}(t)+\int_0^t \boldsymbol{h}_{\mathrm{r}}(t-\tau)\dot{\boldsymbol{\eta}}(\tau)d\tau+\boldsymbol{K}\boldsymbol{\eta}(t)=\boldsymbol{f}_{\mathrm{e}}(t)+\boldsymbol{f}_{\mathrm{PTO}}(t) \tag{3.1}$$

where the hydrodynamic coefficients and wave excitation forces are described in their body-fixed coordinate systems respectively. $\boldsymbol{M}$ is the body mass matrix; $\boldsymbol{m}=\boldsymbol{\mu}(\boldsymbol{\infty})$ is the added mass matrix at infinite frequency; Assume $\boldsymbol{\lambda}(\infty)$, the added damping matrix at infinite frequency to be 0; $\boldsymbol{h}_{\mathrm{r}}(t)$ is the kernel retardation function matrix; $\boldsymbol{K}$ is the stiffness matrix. $\boldsymbol{\eta}(t)$, $\dot{\boldsymbol{\eta}}(t)$ and $\ddot{\boldsymbol{\eta}}(t)$ are the displacement, velocity and acceleration vectors respectively, where the motion of body j is defined as $\boldsymbol{\eta}^j=\left[\eta_1^j;\ \eta_2^j;\ \eta_3^j;\ \eta_4^j;\ \eta_5^j;\ \eta_6^j\right]=\left[x^j;\ y^j;\ z^j;\ \varphi^j;\ \theta^j;\ \psi^j\right]$, representing the surge motion, sway motion, heave motion, roll angle, pitch angle, and yaw angle of j-th body respectively. $\boldsymbol{f}_{\mathrm{PTO}}(t)$ is the PTO damping force vector between adjacent multiple floating bodies. $\int_0^t \boldsymbol{h}_{\mathrm{r}}(t-\tau)\dot{\boldsymbol{\eta}}\left(\tau\right)d\tau$ is the convolution integral expression of radiation force. It can be approximated and expressed by state-space representation, which will be discussed in detail in the following sections.

In studies of wave motion on the surface of a fluid, it is common to assume that the amplitudes of the waves are small compared to the wavelengths in Airy wave theory [79]. For simplicity, a regular wave can be assumed to be sinusoidal with constant wave amplitude, wavelength, and wave period. Thus, in regular waves, the wave excitation force $\boldsymbol{f}_{\mathrm{e}}$ can be expressed as sinusoidal functions,

$$\boldsymbol{f}_{\mathrm{e},i}^j=\zeta^{\mathrm{A}}f_{\mathrm{W}}^j\sin\left(\omega t+\varepsilon_i^j\right),\ i=1,\ 2,\ \cdots 6 \tag{3.2}$$

where $\boldsymbol{f}_{\mathrm{e}}{}^j$ are the components of the j-th wave excitation force vector; f_{w} is the wave force transfer function; ζ^{A} is the incoming wave amplitude; ω is the angular wave frequency; ε_i^j are the phases of harmonic components of a periodic wave.

3.3 PTO system

The PTO force $\boldsymbol{f}_{\mathrm{PTO}}(t)$ is the PTO damping force vector between adjacent multiple floating bodies, which is defined as,

$$f_{\mathrm{PTO}}{}^{j}(t) = -B^{j}_{\mathrm{PTO}}\dot{\eta}^{j}_{7}(t),\ j = 1,\ 2, \cdots,\ N-1 \tag{3.3}$$

where B^{j}_{PTO} is the PTO damping between the adjacent j-th and $(j+1)$-th floating bodies, which is defined as a constant; $\dot{\eta}^{j}_{7}(t)$ is the relative velocity between the adjacent j-th and $(j+1)$-th floating bodies. The relative motions between the adjacent floating bodies can be either translations or rotations. With different types of mechanical connections within a system, the DoFs associated with relative motion can increase. When two bodies are connected, the relative motions will be restricted. The restrictions are inherently related to the type of connection. For instance, if the connection between two bodies is a sliding connection, the relative motion η_7 will correspond to the relative translation Δs; if the connection between two bodies is a hinge connection, the relative motion η_7 will correspond to the relative rotation $\Delta\theta$.

The average power output of the system's PTO is defined as,

$$P_{\mathrm{PTO}} = \frac{1}{T}\int_{0}^{T}\left[\sum_{j=1}^{N-1} B^{j}_{\mathrm{PTO}}\dot{\eta}^{j}_{7}(t)^{2}\right]dt \tag{3.4}$$

This equation calculates the integral of the instantaneous power generation over a time period of T, considering the collective contributions of each PTO in the system.

3.4 Impulse response theory

In the time domain, the non-linear radiation term in the motion equation can be derived from Cummins' impulse theory [15]. According to Cummins' equation, the radiation force is,

$$\boldsymbol{f}^{\mathrm{R}}(t) = \int_{0}^{t}\boldsymbol{h}_{\mathrm{r}}(t-\tau)\dot{\boldsymbol{\eta}}(\tau)d\tau \tag{3.5}$$

where $\boldsymbol{h}_{\mathrm{r}}(t)$ is the retardation kernel function, representing the wave memory effect. $\boldsymbol{h}_{\mathrm{r}}(t)$ can be obtained from the added mass or added damping in the frequency domain,

$$\boldsymbol{h}_{\mathrm{r}}(t) = \frac{2}{\pi}\int_0^\infty \omega(m - \boldsymbol{\mu}_{\mathrm{r}}(\omega))\sin(\omega t)d\omega = \frac{2}{\pi}\int_0^\infty \boldsymbol{\lambda}_{\mathrm{r}}(\omega)\cos(\omega t)d\omega \tag{3.6}$$

where $\boldsymbol{\mu}_{\mathrm{r}}(\omega)$ is the added mass in frequency domain; $\boldsymbol{\lambda}_{\mathrm{r}}(\omega)$ is the added damping in frequency domain. $\boldsymbol{h}_{\mathrm{r}}(s)$, the Laplace transform of $\boldsymbol{h}_{\mathrm{r}}(t)$, can be regarded as the transfer function from the velocity $\dot{\boldsymbol{\eta}}(s)$ to the radiation force $\boldsymbol{f}^{\mathrm{R}}(s)$. In conclusion, the radiation force is related to the body's added mass and added damping in all wave frequencies. These parameters are usually computed in potential flow software. In this thesis, a 3D potential flow solver, WADAM, is utilised to solve the added mass and added damping for both single and multiple bodies across different frequencies [80].

Multi-body hydrodynamic interactions considered in this thesis are mainly caused by the radiation effect of j-th body induced by k-th body. Therefore, for a N-body system, the $\boldsymbol{h}_{\mathrm{r}}$ has the dimension of N and comprising components denoted as h_{r}^{jk}, where $j = 1,\ 2,\ \cdots,\ N$ and $k = 1,\ 2,\ \cdots,\ N$. When $j = k$, h_{r}^{jk} represents the retardation kernel function specific to the body itself; when $j \neq k$, h_{r}^{jk} refers to the interaction between different bodies.

3.5 State-space representation

3.5.1 System identification of radiation term

The transfer function from the velocity $\dot{\boldsymbol{\eta}}(t)$ to the radiation force $\boldsymbol{f}^{\mathrm{R}}(t)$ can be approximated with polynomial equations, and represented in state-space form,

$$\begin{aligned} \boldsymbol{f}^{\mathrm{R}}(t) &= \boldsymbol{C_r}\cdot\boldsymbol{u}(t) \\ \dot{\boldsymbol{u}}(t) &= \boldsymbol{A_r}\cdot\boldsymbol{u}(t) + \boldsymbol{B_r}\dot{\boldsymbol{\eta}}(t) \end{aligned} \tag{3.7}$$

where the memory effect of wave is defined as the observation of the state space. $\boldsymbol{u}(t)$ is the state vector with dimension $n \times 1$. $\boldsymbol{A_r}$, $\boldsymbol{B_r}$ and $\boldsymbol{C_r}$ are the system matrix, the state matrix and the output matrix, with dimension $n \times n$, $n \times 1$ and $1 \times n$. Define $\eta(t)$

as the input and $f^{\mathrm{R}}(t)$ as the output of the dynamic process, the convolutional term of the input and output is

$$f^{\mathrm{R}}(t) = \int_0^t h_{\mathrm{r}}(t-\tau)\eta(\tau)d\tau. \tag{3.8}$$

This convolutional form of h_{r} and η in the time domain can be converted to the product form in the frequency domain. The dynamic process of a system can be described as follows,

$$\begin{aligned} &\frac{d^n f^{\mathrm{R}}}{dt^n} + q_{n-1}\frac{d^{n-1} f^{\mathrm{R}}}{dt^{n-1}} + ... + q_2\frac{d^2 f^{\mathrm{R}}}{dt^2} + q_1\frac{df^{\mathrm{R}}}{dt} + q_0 f^{\mathrm{R}} \\ &= p_{n-1}\frac{d^{n-1}\eta}{dt^{n-1}} + p_{n-2}\frac{d^{n-2}\eta}{dt^{n-2}} + ... + p_2\frac{d^2\eta}{dt^2} + p_1\frac{d\eta}{dt} + p_0\eta \end{aligned}, \tag{3.9}$$

where the derivative order of the output is higher than that of the input. It makes the dynamic process a stable one. Combing Eqs. 3.7 and 3.9, one gets

$$\begin{aligned} \boldsymbol{A_r} &= \begin{bmatrix} -q_{n-1} & -q_{n-2} & \cdots & -q_1 & -q_0 \\ 1 & 0 & \cdots & 0 & 0 \\ 0 & 1 & \cdots & 0 & 0 \\ \vdots & \vdots & \ddots & \vdots & \vdots \\ 0 & 0 & \cdots & 1 & 0 \end{bmatrix}, \boldsymbol{B_r} = \begin{bmatrix} 1 \\ 0 \\ 0 \\ \vdots \\ 0 \end{bmatrix} \\ \boldsymbol{C_r} &= \begin{bmatrix} p_{n-1} & p_{n-2} & \cdots & p_1 & p_0 \end{bmatrix} \end{aligned} \tag{3.10}$$

Operating the Laplace transform of Eq. 3.9,

$$h_{\mathrm{r}}(s) = \frac{p_{n-1}s^{n-1} + p_{n-2}s^{n-2} + ... + p_2 s^2 + p_1 s + p_0}{s^n + q_{n-1}s^{n-1} + q_{n-2}s^{n-2} + ... + q_2 s^2 + q_1 s + q_0}, \tag{3.11}$$

where $h_{\mathrm{r}}(s)$ is retardation kernel function in s-domain. The order number $n \geq 2$. It is also expressed in matrix notation as follows,

$$h_{\mathrm{r}}(s) = \boldsymbol{C_r}(s\boldsymbol{I} - \boldsymbol{A_r})^{-1}\boldsymbol{B_r}, \tag{3.12}$$

where $\boldsymbol{I}$ is unit diagonal matrix. Eq. 3.6 is the time-domain expression of the retardation kernel function, and it can be transformed to the frequency domain through the

Fourier transformation,

$$h_{\mathrm{r}}(i\omega) = \int_0^\infty h_{\mathrm{r}}(t)e^{i\omega\tau}d\tau = \lambda(\omega) + i\omega[\mu(\omega) - \mu(\infty)] \tag{3.13}$$

where $\mu(\infty)$ is the added mass at infinite frequency. According to Eq. 3.11 and 3.12

$$\begin{aligned}&\frac{p_{n-1}(i\omega)^{n-1}+p_{n-2}(i\omega)^{n-2}+...+p_2(i\omega)^2+p_1(i\omega)+p_0}{(i\omega)^n+q_{n-1}(i\omega)^{n-1}+q_{n-2}(i\omega)^{n-2}+...+q_2(i\omega)^2+q_1(i\omega)+q_0}.\\&=\lambda(\omega)+i\omega[\mu(\omega)-\mu(\infty)]\end{aligned} \tag{3.14}$$

Parameters p and q can be estimated by the least square method.

The system matrices $\boldsymbol{A_r}$, $\boldsymbol{B_r}$ and $\boldsymbol{C_r}$ are derived by frequency-domain identification (FDI) using the MSS FDI toolbox [81]. Hence, when considering the wave surface memory effect, Eq. 3.1 can be written as,

$$\begin{aligned}(\boldsymbol{M}+\boldsymbol{m})\ddot{\boldsymbol{\eta}}(t)+\boldsymbol{C_r}\cdot\boldsymbol{u}(t)+\boldsymbol{K}\boldsymbol{\eta}(t)&=\boldsymbol{f}_e(t)+\boldsymbol{f}_{\mathrm{PTO}}(t)\\\dot{\boldsymbol{u}}(t)&=\boldsymbol{A_r}\cdot\boldsymbol{u}(t)+\boldsymbol{B_r}\dot{\boldsymbol{\eta}}(t)\end{aligned} \tag{3.15}$$

For a two-body system, Eq. 3.15 can be expressed in matrix notation as,

$$\begin{aligned}&\begin{bmatrix}\boldsymbol{M}^1+\boldsymbol{m}^1 & \boldsymbol{m}^{12}\\ \boldsymbol{m}^{21} & \boldsymbol{M}^2+\boldsymbol{m}^2\end{bmatrix}\begin{bmatrix}\ddot{\boldsymbol{\eta}}^1\\ \ddot{\boldsymbol{\eta}}^2\end{bmatrix}+\begin{bmatrix}\boldsymbol{C}_r^1 & \boldsymbol{C}_r^{12} & \boldsymbol{0} & \boldsymbol{0}\\ \boldsymbol{0} & \boldsymbol{0} & \boldsymbol{C}_r^2 & \boldsymbol{C}_r^{21}\end{bmatrix}\begin{bmatrix}\boldsymbol{u}^1\\ \boldsymbol{u}^{12}\\ \boldsymbol{u}^2\\ \boldsymbol{u}^{21}\end{bmatrix}\\&+\begin{bmatrix}\boldsymbol{K}^1 & \boldsymbol{0}\\ \boldsymbol{0} & \boldsymbol{K}^2\end{bmatrix}\begin{bmatrix}\boldsymbol{\eta}^1\\ \boldsymbol{\eta}^2\end{bmatrix}=\begin{bmatrix}\boldsymbol{f}_e^1+\boldsymbol{f}_{PTO}\\ \boldsymbol{f}_e^2-\boldsymbol{f}_{PTO}\end{bmatrix}\end{aligned} \tag{3.16}$$

$$\begin{bmatrix}\dot{\boldsymbol{u}}^1\\ \dot{\boldsymbol{u}}^{12}\\ \dot{\boldsymbol{u}}^2\\ \dot{\boldsymbol{u}}^{21}\end{bmatrix}=\begin{bmatrix}\boldsymbol{A}_r^1 & \boldsymbol{0} & \dots & \boldsymbol{0}\\ \boldsymbol{0} & \boldsymbol{A}_r^{12} & \boldsymbol{0} & \vdots\\ \vdots & \boldsymbol{0} & \boldsymbol{A}_r^2 & \boldsymbol{0}\\ \boldsymbol{0} & \dots & \boldsymbol{0} & \boldsymbol{A}_r^{21}\end{bmatrix}\begin{bmatrix}\boldsymbol{u}^1\\ \boldsymbol{u}^{12}\\ \boldsymbol{u}^2\\ \boldsymbol{u}^{21}\end{bmatrix}+\begin{bmatrix}\boldsymbol{B}_r^1 & \boldsymbol{0}\\ \boldsymbol{0} & \boldsymbol{B}_r^{12}\\ \boldsymbol{0} & \boldsymbol{B}_r^2\\ \boldsymbol{B}_r^{21} & \boldsymbol{0}\end{bmatrix}\begin{bmatrix}\dot{\boldsymbol{\eta}}^1\\ \dot{\boldsymbol{\eta}}^2\end{bmatrix}$$

3.5.2 Linearised representation

In the body-fixed coordinate system, define the state vector $\boldsymbol{x} = [\boldsymbol{\eta}(t), \dot{\boldsymbol{\eta}}(t), \boldsymbol{u}(t)]^{\mathrm{T}}$, Eq. 3.8 can be written in a linearised representation as,

$$\begin{gathered} \dot{\boldsymbol{x}} = \gamma \cdot \boldsymbol{x} + \zeta \\ \gamma = \begin{bmatrix} \mathbf{0} & \boldsymbol{\Lambda} & \mathbf{0} \\ -\dfrac{\boldsymbol{K}}{\boldsymbol{M}+\boldsymbol{m}} & \mathbf{0} & -\dfrac{\boldsymbol{C_r}}{\boldsymbol{M}+\boldsymbol{m}} \\ \mathbf{0} & \boldsymbol{B_r} & \boldsymbol{A_r} \end{bmatrix}, \\ \zeta = \begin{bmatrix} \mathbf{0} \\ -\dfrac{\boldsymbol{f}_{\mathrm{e}}(t) + \boldsymbol{f}_{\mathrm{PTO}}(t)}{\boldsymbol{M}+\boldsymbol{m}} \\ \mathbf{0} \end{bmatrix} \end{gathered} \tag{3.17}$$

This linearised expression is more convenient for computation and adding a damping force as the control force. The motion equation can be solved with the 4th-order Runge Kutta method in MATLAB. Furthermore, the hydrodynamic interactions between multiple bodies induced by wave radiation are also considered.

3.6 Constraint matrix of hinged bodies

In the cases of two floating bodies, N is set to 2. The motion equation of the two-body system has 12 DoFs, where $\boldsymbol{\eta} = \left[\eta_i^1, \eta_i^2\right]^{\mathrm{T}}$, $i = 1,\ 2,\ \cdots,\ 6$. The hinge connections used in this work limit the relative motions in five directions, leaving one direction unrestricted. For two bodies with hinge connection, $f_{\mathrm{PTO}} = -B_{\mathrm{PTO}}\dot{\eta}_7(t)^2$, where $\dot{\eta}_7(t)$ is the unrestricted DoF, representing the relative velocity between the two bodies.

With a constraint matrix, the motions $\boldsymbol{\eta}^2$ can be represented by the motions $\boldsymbol{\eta}^1$ and the relative motion η_7. The multi-body system's motion can be rewritten as,

$$\boldsymbol{\eta} = \begin{bmatrix} \boldsymbol{\eta}^1 \\ \boldsymbol{\eta}^2 \end{bmatrix} = \boldsymbol{S} \begin{bmatrix} \boldsymbol{\eta}^1 \\ \eta_7 \end{bmatrix} = \boldsymbol{S}\boldsymbol{\eta}' \tag{3.18}$$

where S is the coefficient matrix of constraints. In Chapters 5 to 7, the specific form

of S will be derived based on the corresponding multi-body model. In the motion equation of the connected system, $\boldsymbol{\eta}$, $\dot{\boldsymbol{\eta}}$, $\ddot{\boldsymbol{\eta}}$ can be replaced by $\boldsymbol{\eta}'$, $\dot{\boldsymbol{\eta}}'$, $\ddot{\boldsymbol{\eta}}'$, the original 12-DoF equation 3.7 can be transformed into a 7-DoF equation set,

$$\begin{aligned}(\boldsymbol{M}+\boldsymbol{m})\boldsymbol{S}\ddot{\boldsymbol{\eta}}'(t)+\boldsymbol{C_r}\cdot\boldsymbol{u}(t)+\boldsymbol{K}\boldsymbol{S}\boldsymbol{\eta}'(t)&=\boldsymbol{f}_{\mathrm{e}}(t)+\boldsymbol{f}_{\mathrm{PTO}}(t)+\boldsymbol{f}_{\mathrm{h}}(t)\\ \dot{\boldsymbol{u}}(t)&=\boldsymbol{A_r}\cdot\boldsymbol{u}(t)+\boldsymbol{B_r}\boldsymbol{S}\dot{\boldsymbol{\eta}}'(t)\end{aligned} \tag{3.19}$$

In order to eliminate the hinge forces $\boldsymbol{f}_{\mathrm{h}}(t)$, multiplies the matrix $\boldsymbol{S}^{\mathrm{T}}$ at both sides of Eq. 3.12. Eq. 3.12 can then be derived as,

$$\begin{aligned}\boldsymbol{S}^{\mathbf{T}}(\boldsymbol{M}+\boldsymbol{m})\boldsymbol{S}\ddot{\boldsymbol{\eta}}'(t)+\boldsymbol{S}^{\mathbf{T}}\boldsymbol{C_r}\cdot\boldsymbol{u}(t)+\boldsymbol{S}^{\mathbf{T}}\boldsymbol{K}\boldsymbol{S}\boldsymbol{\eta}'(t)&=\boldsymbol{S}^{\mathbf{T}}\boldsymbol{f}_{\mathrm{e}}(t)+\boldsymbol{S}^{\mathbf{T}}\boldsymbol{f}_{\mathrm{PTO}}(t)\\ \dot{\boldsymbol{u}}(t)&=\boldsymbol{A_r}\cdot\boldsymbol{u}(t)+\boldsymbol{B_r}\boldsymbol{S}\dot{\boldsymbol{\eta}}'(t)\end{aligned} \tag{3.20}$$

The hinge forces $\boldsymbol{f}_{\mathrm{h}}(t)$ can be eliminated when it multiplies the matrix $\boldsymbol{S}^{\mathrm{T}}$ because in the coordinate system of the hinge system, the hinge forces are internal forces. According to Newton' s third law, the hinge forces and torques of the two bodies are of equal magnitude and opposite direction, and the torques need to be superimposed with the product of relevant forces and arms. Take the two hinged boxes in Fig. 3.2 for example, $f^1_{\mathrm{h},1}=-f^2_{\mathrm{h},5}$, and $f^1_{\mathrm{h},5}=-Rf^1_{\mathrm{h},3}$. The mathematical derivation can be seen as follows,

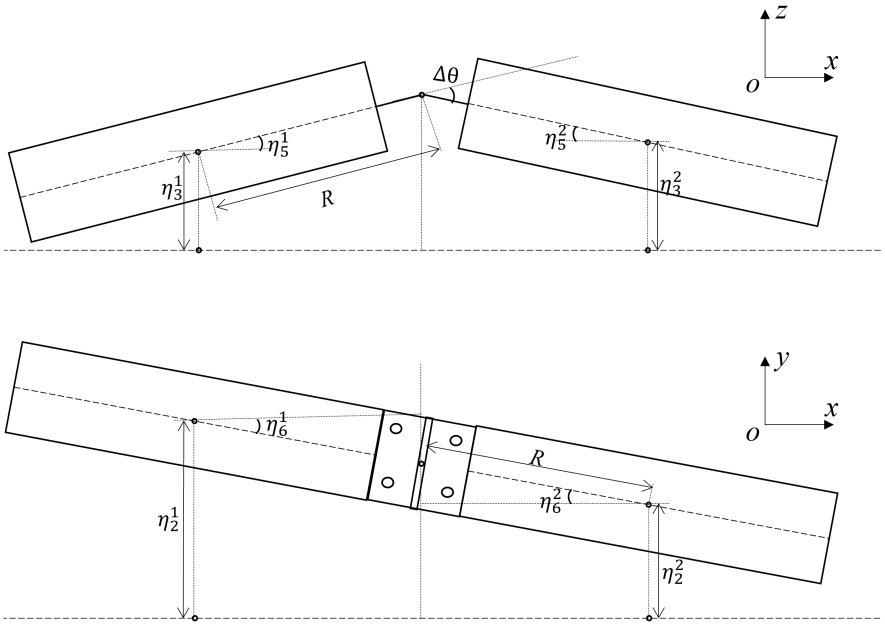

Figure 3.2: Two hinged boxes.

$$\boldsymbol{S}^{\mathrm{T}}\boldsymbol{f}_{\mathrm{h}}(t) = \boldsymbol{S}^{\mathrm{T}} \begin{bmatrix} f_{\mathrm{h},1}^1 \\ f_{\mathrm{h},2}^1 \\ f_{\mathrm{h},3}^1 \\ f_{\mathrm{h},4}^1 \\ -Rf_{\mathrm{h},3}^1 \\ f_{\mathrm{h},6}^1 + Rf_{\mathrm{h},2}^1 \\ f_{\mathrm{h},1}^2 \\ f_{\mathrm{h},2}^2 \\ f_{\mathrm{h},3}^2 \\ f_{\mathrm{h},4}^2 \\ Rf_{\mathrm{h},3}^2 \\ f_{\mathrm{h},6}^2 - Rf_{\mathrm{h},2}^2 \end{bmatrix} = \begin{bmatrix} f_{\mathrm{h},1}^1 + f_{\mathrm{h},1}^2 \\ f_{\mathrm{h},2}^1 + f_{\mathrm{h},2}^2 \\ f_{\mathrm{h},3}^1 + f_{\mathrm{h},3}^2 \\ f_{\mathrm{h},4}^1 + f_{\mathrm{h},4}^2 \\ -Rf_{\mathrm{h},3}^1 - 2Rf_{\mathrm{h},3}^2 + f_{\mathrm{h},5}^2 \\ f_{\mathrm{h},6}^1 + Rf_{\mathrm{h},2}^1 + 2Rf_{\mathrm{h},2}^2 + f_{\mathrm{h},6}^2 - Rf_{\mathrm{h},2}^2 \\ -Rf_{\mathrm{h},3}^2 + Rf_{\mathrm{h},3}^2 \end{bmatrix} = \mathbf{0} \quad (3.21)$$

For an N-body system, there is one hinge connection between each pair of adjacent bodies. The total constraint matrix is the product of the individual constraint matrices.

The motion matrix of the system can be rewritten as,

$$\begin{aligned}\boldsymbol{\eta} = \begin{bmatrix} \boldsymbol{\eta}^1 \\ \boldsymbol{\eta}^2 \\ \vdots \\ \boldsymbol{\eta}^{N-1} \\ \boldsymbol{\eta}^N \end{bmatrix} &= \begin{bmatrix} \boldsymbol{I} & \boldsymbol{0} & \dots & \boldsymbol{0} & \boldsymbol{0} \\ \boldsymbol{S}_{21} & \boldsymbol{S}_{22} & \dots & \boldsymbol{0} & \boldsymbol{0} \\ \vdots & \vdots & \ddots & \vdots & \vdots \\ \boldsymbol{S}_{21}^{N-2} & \boldsymbol{S}_{21}^{N-3}\boldsymbol{S}_{22} & \dots & \boldsymbol{S}_{22} & \boldsymbol{0} \\ \boldsymbol{S}_{21}^{N-1} & \boldsymbol{S}_{21}^{N-2}\boldsymbol{S}_{22} & \dots & \boldsymbol{S}_{21}\boldsymbol{S}_{22} & \boldsymbol{S}_{22} \end{bmatrix} \begin{bmatrix} \boldsymbol{\eta}^1 \\ \boldsymbol{\Delta\theta}^1 \\ \vdots \\ \boldsymbol{\Delta\theta}^{N-2} \\ \boldsymbol{\Delta\theta}^{N-1} \end{bmatrix} \\ &= \boldsymbol{S} \begin{bmatrix} \boldsymbol{\eta}^1 \\ \boldsymbol{\Delta\theta}^1 \\ \vdots \\ \boldsymbol{\Delta\theta}^{N-2} \\ \boldsymbol{\Delta\theta}^{N-1} \end{bmatrix} = \boldsymbol{S}\boldsymbol{\eta}' \end{aligned} \tag{3.22}$$

In the global coordinate system, define the new state vector $\boldsymbol{x}' = [\boldsymbol{\eta}'(t), \dot{\boldsymbol{\eta}}'(t), \boldsymbol{u}(t)]^{\mathrm{T}}$, the linearised motion response of connected multiple floating bodies can be written as,

$$\begin{aligned} \dot{\boldsymbol{x}}' &= \gamma \cdot \boldsymbol{x}' + \zeta \\ \gamma &= \begin{bmatrix} \boldsymbol{0} & \boldsymbol{\Lambda} & \boldsymbol{0} \\ -\dfrac{\boldsymbol{S}^{\mathrm{T}}\boldsymbol{K}\boldsymbol{S}}{\boldsymbol{S}^{\mathrm{T}}(\boldsymbol{M}+\boldsymbol{m})\boldsymbol{S}} & \boldsymbol{0} & -\dfrac{\boldsymbol{S}^{\mathrm{T}}\boldsymbol{C}_{\boldsymbol{r}}}{\boldsymbol{S}^{\mathrm{T}}(\boldsymbol{M}+\boldsymbol{m})\boldsymbol{S}} \\ \boldsymbol{0} & \boldsymbol{B}_{\boldsymbol{r}}\boldsymbol{S} & \boldsymbol{A}_{\boldsymbol{r}} \end{bmatrix}, \\ \zeta &= \begin{bmatrix} \boldsymbol{0} \\ -\dfrac{\boldsymbol{f}_{\mathrm{e}}(t) + \boldsymbol{f}_{\mathrm{PTO}}(t)}{\boldsymbol{S}^{\mathrm{T}}(\boldsymbol{M}+\boldsymbol{m})\boldsymbol{S}} \\ \boldsymbol{0} \end{bmatrix} \end{aligned} \tag{3.23}$$

3.7 Summary

This chapter establishes a series of time-domain motion equations of multiple floating bodies subjected to wave-induced dynamics. The equations consider several critical factors: the fluid memory effect, expressed via a retardation function; hinge connection constraints, solved through the constraint matrix approach; the interactions resulting

from PTO force. The calculation of PTO power is given explicitly. Subsequently, these equations are written in a state-space representation to achieve their linearisation.

There are also several conclusions about the multiple floating bodies' dynamics:

- The hinge force is the internal force of the system and can be eliminated in calculations.
- For multiple floating bodies, the interactions from connections are more important than the interactions from hydrodynamics.
- The PTO power is dependent on the damping coefficient and wave frequency in regular waves.

Chapter 4

Control Algorithm of Multiple Floating Bodies

4.1 Introduction

In the context of wave energy conversion, phase control is a strategy to maximise the energy extracted by ensuring that the motion of the WEC is in phase with the wave excitation forces. In a simplified sense, the phase between the oscillating system (the WEC) and the excitation (the waves) is crucial for energy transfer. Building upon this principle, it can also be deduced that by tuning a floater's motion to be in an antiphase with the wave excitation forces, one can enhance the stability of the floating structure. Therefore, a control method that can fulfil various control objectives is developed to manage the wave energy conversion within a floating multi-body system.

4.2 Semi-active phase control

A combination of semi-active control with phase control is introduced herein. Semi-active components adjust their characteristics to help the system maintain an optimal phase relationship with the incoming waves, enhancing energy capture without the need for large power inputs. The semi-active phase control involves two complementary strategies: latching control and declutching control.

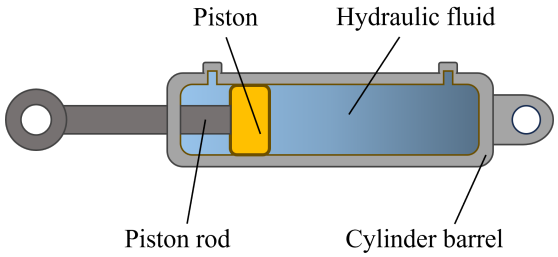

Figure 4.1: The sketch of a hydraulic power-take-off (PTO) device for translational or rotational motion.

4.2.1 Phase control

Phase control is often used in active vibration control systems to reduce or eliminate vibrations in mechanical systems by adjusting the phase relationship between forces and velocities [3]. In ocean engineering, phase control is also very commonly applied to control the phase between wave forces and the velocities of floating WECs to enhance their energy absorption efficiency. Latching control and declutching control employed in this thesis are two complementary on-off control strategies to realise phase control. Their control commands are both binary functions, which ensure the system switches between two discrete states. The binary mode employs a 0-1 control strategy to tune system responses.

Latching control provides an infinite damping force alternatively by locking and releasing the floating body with a brake system. The braking effect is similar to a car handbrake, where the brake is applied at zero velocity and reliance is made on static friction to prevent motion [3]. In the algorithm of latching control, the control command "1" triggers the imposition of a theoretical infinite damping force, like the engagement of a brake, thereby "latching" the motion of the structure; the control command "0" resets the system back to its normal operation state.

For a single floater, the latching force from the PTO system allows it to stay static and "wait for"the wave force to be in phase. However, for most multiple floating bodies, the connections and latching forces can only restrain the relative motion between bodies. They cannot be locked to "wait for" the waves. Therefore, unlike its application in single-body systems, latching control in multi-body systems lacks the capacity to

precisely tune the phase of the bodies' motions with the incoming wave forces. This limitation requires a different control logic to enhance energy capture efficiency.

Declutching control system provides discrete damping force by switching on and off alternatively the by-pass valve in the circuit of the hydraulic cylinder. When control command is 0, the by-pass valve is closed, and the damping force is $B_{\mathrm{PTO}}\dot{\eta}_7$; when control command is 1, the by-pass valve is open, and the damping force is 0. In the algorithm of declutching control, the control command "1" triggers the switching-off of the PTO, reducing the value of the PTO damping coefficient to 0 instantaneously; the control command "0" resets the damping of PTO back to B_{PTO}. In summary, the range of the PTO damping coefficient in the latching control can be equivalent to $[B_{\mathrm{PTO}}, +\infty]$; for declutching control, the range is $[0, B_{\mathrm{PTO}}]$.

4.2.2 Declutching control

To enhance the performance of a two-body coaxial axisymmetric WEC, the sub-optimal latching control method, as proposed in [57], was tested by Cândido in [68]. This method proved to be effective for a single-body device. This, however, was not the case for the two-body device, particularly under irregular wave conditions. It can be inferred that the latching control method, when applied to floaters without connection to seabed, does not directly control the absolute displacement of the bodies. This limitation necessitates a different control logic to adjust the phase between body motion and wave force. Therefore, this thesis focuses exclusively on the application of declutching control.

For declutching control, when the control command of declutching control is 0, the value of damping force is $B_{\mathrm{PTO}}\Delta\dot{\theta}$; when the control command is 1, the damping force is 0. When the binary control command, β, is introduced to Eq. 3.13, the controlled PTO forces can be written as,

$$f_{\mathrm{PTO}} = (B_{\mathrm{PTO}} + \beta(t)B_{\mathrm{c}})\Delta\dot{\theta}(t) \tag{4.1}$$

where B_{c} and B_{PTO} represent the damping coefficients of the control device and the

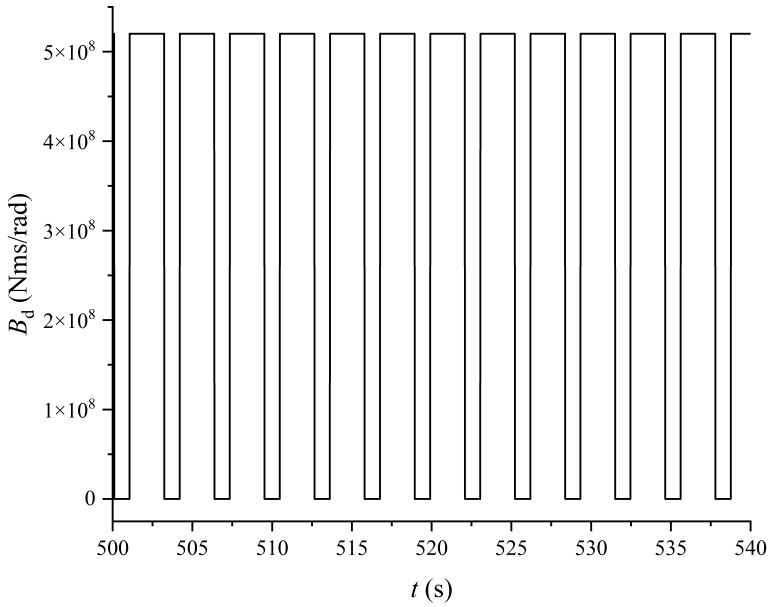

Figure 4.2: Time history of the PTO damping coefficient under optimal declutching control.

PTO system in pitch direction. We define that $B_c = -B_{PTO}$ in declutching control, representing the PTO is switched off when declutching control is activated. Define the total declutching control damping coefficient as $B_d(t) = B_{PTO} + \beta(t)B_c$. An example of the time history of B_d is shown in Fig. 4.2. In the following discussions, "without control" refers to not considering declutching control, but with damping control; whereas "with control" indicates that the PTO damping is not a constant but a discrete variable (referring to Eq. 4.1) that can be controlled to optimise the system's performance.

With the binary control command β, the linearised representation of the dynamics of the multiple floating bodies, Eq. 3.14, can be written as

$$\dot{\boldsymbol{x}'} = \gamma \cdot \boldsymbol{x}' + \zeta$$

$$\gamma = \begin{bmatrix} \mathbf{0} & \boldsymbol{\Lambda} & \mathbf{0} \\ -\dfrac{\boldsymbol{S}^{\mathrm{T}}\boldsymbol{K}\boldsymbol{S}}{\boldsymbol{S}^{\mathrm{T}}(\boldsymbol{M}+\boldsymbol{m})\boldsymbol{S}} & -\dfrac{\boldsymbol{S}^{\mathrm{T}}(\boldsymbol{B}_{\mathrm{PTO}}+\beta(t)\boldsymbol{B}_{\mathrm{c}})}{\boldsymbol{S}^{\mathrm{T}}(\boldsymbol{M}+\boldsymbol{m})\boldsymbol{S}} & -\dfrac{\boldsymbol{S}^{\mathrm{T}}\boldsymbol{C}_{\boldsymbol{r}}}{\boldsymbol{S}^{\mathrm{T}}(\boldsymbol{M}+\boldsymbol{m})\boldsymbol{S}} \\ \mathbf{0} & \boldsymbol{B}_{\boldsymbol{r}}\boldsymbol{S} & \boldsymbol{A}_{\boldsymbol{r}} \end{bmatrix}, \tag{4.2}$$

$$\zeta = \begin{bmatrix} \mathbf{0} \\ -\dfrac{\boldsymbol{f}_{\mathrm{e}}(t)}{\boldsymbol{S}^{\mathrm{T}}(\boldsymbol{M}+\boldsymbol{m})\boldsymbol{S}} \\ \mathbf{0} \end{bmatrix}$$

The damping forces from the PTO system and the control system are written in the same term in this equation. In this equation, the damping matrices are constructed as,

$$\boldsymbol{B}_{\mathrm{PTO}} = \begin{bmatrix} 0 & 0 & 0 & 0 & B_{\mathrm{PTO}} & 0 \end{bmatrix}^{\mathrm{T}} \tag{4.3}$$

$$\boldsymbol{B}_{\mathrm{c}} = \begin{bmatrix} 0 & 0 & 0 & 0 & B_{\mathrm{c}} & 0 \end{bmatrix}^{\mathrm{T}} \tag{4.4}$$

This linearised expression is more convenient for computation and adding a damping force as the control force.

The range of damping of the declutching control is from 0 to a constant value. Unloading the device during the declutching periods allows the device to "catch up" to the excitation force, which brings the device's velocity (though nonlinear) into phase with the excitation force [3]. The energy costs of declutching control comprise energy consumption of the control system and minor mechanical energy losses due to friction, which are negligible.

4.3 Optimal phase control

4.3.1 Pontryagin's Maximum Principle

PMP is a widely used optimal control theory, which is suitable for continuous-time systems with smooth dynamics and cost functions. It is particularly useful when the optimal control is a bang-bang or singular control. In this research, it can state the way to get the minimum motion of floating bodies in a limited period, from the initial state to the end state with our control.

In this research, PMP is employed to find the optimal control inputs that minimise or maximise cost functions. Objective functions represent the objectives that are being optimised. PMP can solve the control commands that result in a minimum motion of floating bodies or a maximum power absorption of PTO devices over a given computation period. These objective functions are computed along the trajectory of the system, which describes the system's motion from its initial static state to its final state.

In order to minimise or maximise the target objective function, we need to minimise or maximise Hamiltonian, H, calculated by the state of the system.

$$\begin{aligned} H &= L + \boldsymbol{\lambda}(\gamma \cdot \boldsymbol{x}' + \zeta) \\ \dot{\boldsymbol{\lambda}} &= -\frac{\partial H}{\partial \boldsymbol{x}'} = -\frac{\partial L}{\partial \boldsymbol{x}'} - \boldsymbol{\lambda}\gamma \end{aligned} \tag{4.5}$$

where the co-state vector $\boldsymbol{\lambda}$ is Lagrange multiplier and L is Lagrangian function, i.e., the performance index. By solving the value of $\boldsymbol{\lambda}$, the Hamiltonian H containing $\beta(t)$ can be derived. There are two unknown variables in the dynamic equation and Pontryagin's equation: the system state $\boldsymbol{x}$ and the control command β. In theory, Eqs. 4.2 and 4.5 can be coupled and solved together. However, since the dynamic equation is a 2nd ordinary differential equation, we choose to linearise the system and solve the system state $\boldsymbol{x}$ with a numerical method in Matlab before substituting it into the equation of Pontryagin's theorem. In discrete control, the control command $\beta(t)$ is binary, which means the command is either 0 or 1. If H needs to be maximised, β is defined as,

$$\beta = \begin{cases} 0, & \lambda^{\mathrm{T}}(8:14)\dfrac{S^{\mathrm{T}}[-B_{\mathrm{c}};B_{\mathrm{c}}]\dot{\Delta\theta}}{S^{\mathrm{T}}MS} < 0 \\ 1, & \text{ohterwise} \end{cases} \tag{4.6}$$

If H needs to be minimised, β is defined as,

$$\beta = \begin{cases} 1, & \lambda^{\mathrm{T}}(8:14)\dfrac{S^{\mathrm{T}}[-B_{\mathrm{c}};B_{\mathrm{c}}]\dot{\Delta\theta}}{S^{\mathrm{T}}MS} < 0 \\ 0, & \text{ohterwise} \end{cases} \tag{4.7}$$

The key point is to extract the term that includes the control command β from Eq. 4.5. To maximise the objective function, the strategy is: if the term is greater than 0, set β =1 and retain the term; conversely, if the term is less than 0, set $\beta = 0$ and don't count the term. When the goal is to minimise the objective function, the opposite strategy is applied. After β is solved, the responses with control can be computed. The responses with control are introduced to the iteration as the initial state until the control command converges and reaches its numerical optimum. The flow chart of the optimal control process is shown in Fig. 4.3.

4.3.2 Objective functions

The objective function J is defined as a physical value that is optimised during the numerical optimisation process in the time horizon $[0, T]$, representing the performance of the system in a period T.

$$J = \Psi(\boldsymbol{x}'(T), T) + \int_0^T L(\boldsymbol{x}'(t), \beta(t), t)dt \tag{4.8}$$

where $\Psi(\boldsymbol{x}'(T), T)$ is the ending up state. Optimal control problems often include constraints that the solution must satisfy. These can be physical limitations (like maximum speed or force), safety requirements, or operational constraints. In this thesis, the emphasis is on the optimisation process, with constraints being of secondary importance. For simplicity, both the initial and final states of the system under study are defined as static, which implies that both the position, velocity, control commands and other state variables are set to zero. Therefore, a time-averaged objective function

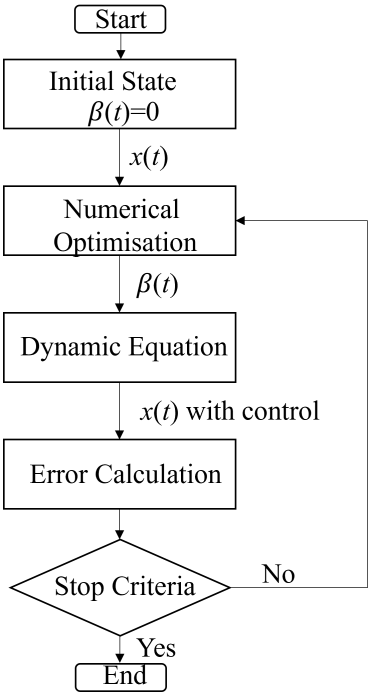

Figure 4.3: Flow chart of optimal declutching control process.

can be defined as,

$$\bar{J} = \frac{1}{T}\int_0^T L(\boldsymbol{x}'(t), \beta(t), t)dt \tag{4.9}$$

$\bar{J}$ reaches its maximum or minimum when H is maximised or minimised. As there are no constraints at the final state in this thesis's cases, each objective function only includes the time-average value of the Lagrangian function. To serve different objectives in varying optimisation scenarios, several alternative objective functions are investigated. The detailed expressions are listed in Chapter 5.

4.4 Summary

This chapter proposes a hybrid approach that combines a semi-active control strategy with an optimal control method. Such a methodology has been extensively utilised in the field of wave energy control, particularly for tuning the phase relationship between wave forces and the motion dynamics of floating wave energy converters. Herein,

we extend the application of this method to the control of multiple floating bodies, adapting it to fulfil a wide range of objectives.

The dynamic model under consideration is a state-space representation of multiple floating bodies, as derived in Chapter 3. In this framework, the proposed control method iteratively updates the system's state variables based on control commands (control variables). The objective functions and constraints related to this multi-body control problem are also introduced. The next chapter will have an in-depth discussion on choosing specific objective functions, establishing convergence criteria, and defining the conditions under which the control method is applicable within the context of a hinged box model.

Chapter 5

Optimal Phase Control Method of Multiple Floating Bodies

5.1 Introduction

This chapter conducts a series of in-depth analyses of the control mechanisms within a typical hinged-box system which is the same as Newman's model [24]. The hydrodynamic interactions, mechanical constraints and state-space representations are all considered based on the dynamic model in Chapter 3. The controlled motions of the system are demonstrated and analysed in regular wave conditions. In this study, it is assumed that wave excitation forces are already known in all time horizons.

5.2 Model validation

This section validates the established hinged multiple floating bodies model with the results of hinged boxes in Newman's research [24]. The same configuration of two hinged boxes is modelled in this research, as shown in Fig. 5.1. As stated in Chapter 3, the frequency-domain hydrodynamic coefficients, including wave forces, added mass, and radiation damping are acquired from a commercial software WADAM [78]. However, it is important to acknowledge that the linearisation assumptions restrict the analysis to exclude any effects from large displacements or angles. The responses for heave and

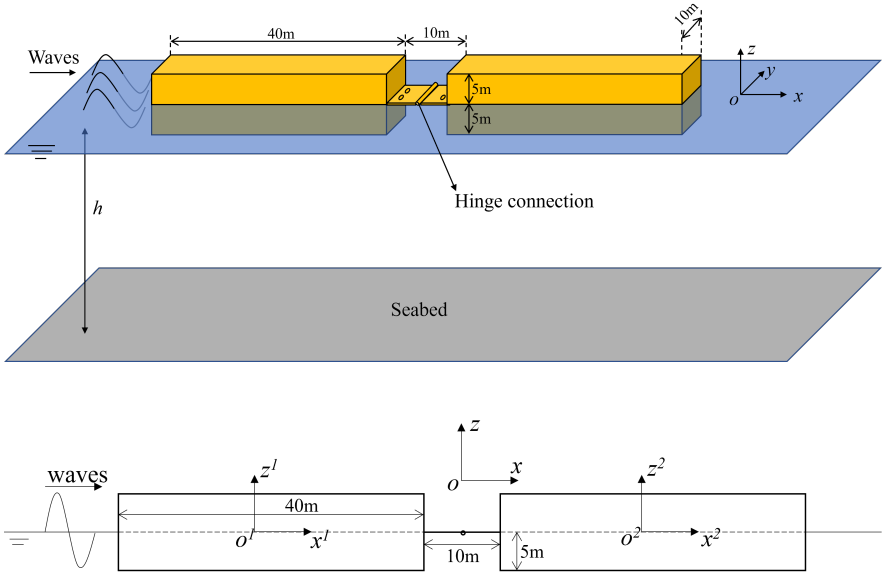

Figure 5.1: Configuration of two hinged boxes.

hinge deflection when the wave frequency is specified as 0.76 rad/s are computed in the time domain.

Because of the constraints at the hinge point, there are no relative motions in the surge, sway, heave, roll, and yaw directions at the hinge point. Hinge constrains the motions at the hinge point of the two bodies to be the same, except for the pitch direction. As illustrated in Fig. 5.2, the relative angle $\Delta\theta$ at the hinge point of the two bodies can be calculated from the difference between their respective pitch angles in the body-fixed coordinate system. Thus, the constraint equations are as follows,

$$\begin{cases} \eta_1^1 = \eta_1^2 \\ \eta_2^1 + R\sin\eta_6^1 = \eta_2^2 - R\sin\eta_6^2 \\ \eta_3^1 - R\sin\eta_5^1 = \eta_3^2 + R\sin\eta_5^2 \\ \eta_4^1 = \eta_4^2 \\ \eta_5^1 = \eta_5^2 - \Delta\theta \\ \eta_6^1 = \eta_6^2 \end{cases} \tag{5.1}$$

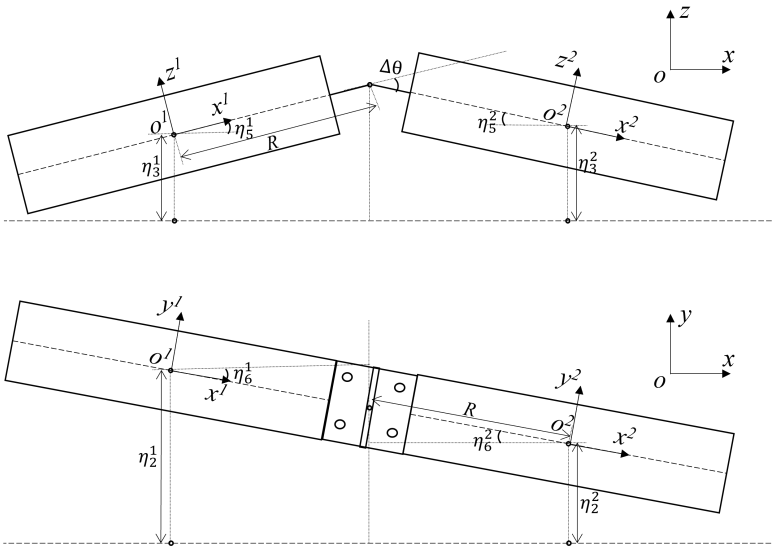

Figure 5.2: Relationship of motions in front view (upper) and top view (below) of the two-box system. For such a right-handed coordinate, the η_5^1 in the upper figure is positive, and the $\Delta\theta$ and η_5^2 are negative.

in which R is the value of distances from the CoGs of the bodies to the hinge point. According to Airy wave theory [79], the pitch amplitude follows the small-angle approximation, thus $\sin\eta_5$ and $\sin\eta_6$ can be written as η_5 and η_6. The constraint equation set can be linearised to Eq. 5.2, which can be expressed in matrix notation as Eq. 5.3.

$$\begin{cases} \eta_1^1 = \eta_1^2 \\ \eta_2^1 + R\eta_6^1 = \eta_2^2 - R\eta_6^2 \\ \eta_3^1 - R\eta_5^1 = \eta_3^2 + R\eta_5^2 \\ \eta_4^1 = \eta_4^2 \\ \eta_5^1 = \eta_5^2 - \Delta\theta \\ \eta_6^1 = \eta_6^2 \end{cases} \tag{5.2}$$

$$\boldsymbol{\eta}^2 = \begin{bmatrix} \eta_1^2 \\ \eta_2^2 \\ \eta_3^2 \\ \eta_4^2 \\ \eta_5^2 \\ \eta_6^2 \end{bmatrix} = \begin{bmatrix} 1 & 0 & 0 & 0 & 0 & 0 \\ 0 & 1 & 0 & 0 & 0 & 2R \\ 0 & 0 & 1 & 0 & -2R & 0 \\ 0 & 0 & 0 & 1 & 0 & 0 \\ 0 & 0 & 0 & 0 & 1 & 0 \\ 0 & 0 & 0 & 0 & 0 & 1 \end{bmatrix} \begin{bmatrix} \eta_1^1 \\ \eta_2^1 \\ \eta_3^1 \\ \eta_4^1 \\ \eta_5^1 \\ \eta_6^1 \end{bmatrix} + \begin{bmatrix} 0 \\ 0 \\ -R \\ 0 \\ 1 \\ 0 \end{bmatrix} [\Delta\theta] \tag{5.3}$$
$$= \boldsymbol{S}_{21}\boldsymbol{\eta}^1 + \boldsymbol{S}_{22}\boldsymbol{\Delta\theta}$$

which indicates that the motions of Box_2 can be represented by the motions of Box_1 and the relative angle $\Delta\theta$. The motion matrix of the system can be rewritten as,

$$\boldsymbol{\eta} = \begin{bmatrix} \boldsymbol{\eta}^1 \\ \boldsymbol{\eta}^2 \end{bmatrix} = \begin{bmatrix} \boldsymbol{I} & \boldsymbol{0} \\ \boldsymbol{S}_{21} & \boldsymbol{S}_{22} \end{bmatrix} \begin{bmatrix} \boldsymbol{\eta}^1 \\ \Delta\theta \end{bmatrix} = \boldsymbol{S}\boldsymbol{\eta}' \tag{5.4}$$

where $\boldsymbol{S}$ is the coefficient matrix of hinge constraints introduced in Chapter 3.

The result in Newman's research at a wave frequency of 0.76 rad/s is transformed into the time domain using Fourier transformation. Fig. 5.3 shows a comparison of the results of the present study and Newman's research, showing good agreement after convergence. Due to the damping effect with time, the initial condition of the system will eventually become negligible and thus have no significant influence on the system's response. It confirms the validity of the present method, which solves the time-domain motion equation of hinged bodies with a constraint matrix.

5.3 Selection of objective function

The objective function $\bar{J}$ is defined as a physical value that is optimised during the numerical optimisation process in the time horizon $[0, T]$, representing the performance of the system in a period T, as defined in the Eq. 4.8.

$\bar{J}$ reaches its maximum or minimum when H is maximised or minimised. As there are no constraints at the final state in this thesis's cases, each objective function only

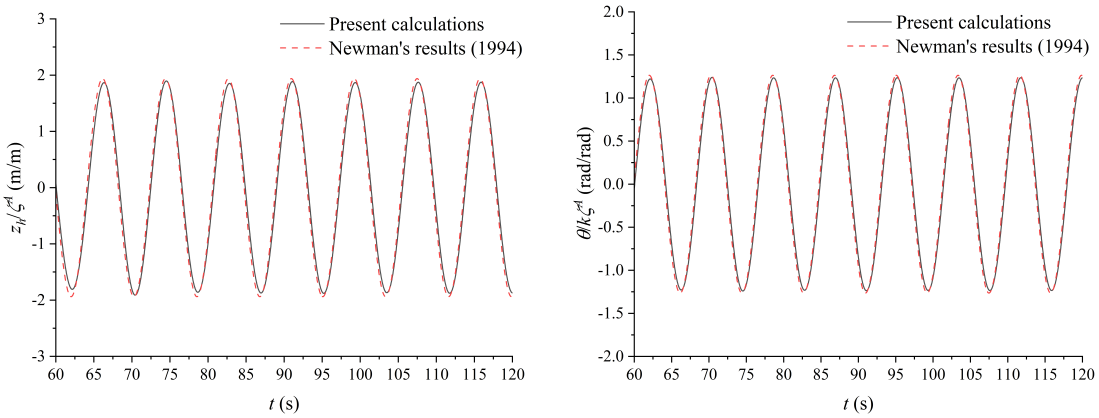

(a) Normalised heave motion. (b) Normalised angular deflection.

Figure 5.3: The time series for normalised heave motion and angular deflection at the hinge point.

includes the time-average value of the Lagrangian function. To serve different objectives in varying optimisation scenarios, several alternative objective functions are investigated, which are expressed by,

$$\min\left(\bar{J}_1\right) = \min\left(\overline{|\dot{\eta}_5^1|}\right) = \min\left(\frac{1}{T}\int_0^T |\dot{\eta}_5^1(t)|dt\right) \tag{5.5}$$

$$\max\left(\bar{J}_2\right) = \max\left(P_{\text{wave}}\right) = \max\left(\frac{1}{T}\int_0^T f_{e,5}^1(t)\dot{\eta}_5^1(t) + f_{e,5}^2(t)\dot{\eta}_5^2(t)dt\right) \tag{5.6}$$

$$\max\left(\bar{J}_3\right) = \max\left(\overline{|\Delta\dot{\theta}|}\right) = \max\left(\frac{1}{T}\int_0^T |\Delta\dot{\theta}(t)|dt\right) \tag{5.7}$$

$$\max\left(\bar{J}_4\right) = \max\left(P_{\text{PTO}}\right) = \max\left(\frac{1}{T}\int_0^T B_{\text{d}}(t)\Delta\dot{\theta}(t)^2 dt\right) \tag{5.8}$$

When $\bar{J}_1$ is applied, the physical meaning is that the average pitch speed of Box_1 is minimised. This corresponds to a scenario of stabilising platforms of floating wind turbines or photovoltaics in various wave conditions. When $\bar{J}_2$ is applied, the total power of wave force, $f_{e,5}\dot{\eta}_5$, is maximised. It corresponds to a scenario of increasing the conversion from wave energy to kinetic energy of multiple floating bodies and providing

a shielded area with fewer waves to protect other floating facilities. This is a common function of breakwaters. When $\bar{J}_3$ is applied, the average relative angular speed of rotation between the two boxes is maximised. Currently, no application in ocean engineering focuses on directly realising this objective. However, it might prove beneficial for minimising $\bar{J}_3$ to enhance the stability of structures such as floating bridges or solar panels. When $\bar{J}_4$ is applied, the physical meaning is that the energy absorption of PTO is maximised. It corresponds to a scenario of increasing the power output of WECs which harnesses relative pitch motion between sections. The selection of the objective function depends on the optimisation goal.

5.4 Number of iterations

To determine when the numerical optimisation reaches convergence, stop criteria are established for the selected performance indices. These stop criteria include a critical number of iterations and a critical error. The iteration of the control algorithm is stopped when $n = n_{\text{critical}}$ or $err < err_{\text{critical}}$ where n is the number of the current iteration, n_{critical} is the maximum number of iterations, err is the error of performance index and err_{critical} is the critical error.

The error of the performance index is expressed as follows,

$$err = \frac{std(\bar{J}\,(n-4:n))}{\bar{J}(n)} \times 100\% \tag{5.9}$$

where $\bar{J}$ is the performance index; $std\,(J\,(n-4:n))$ represents the Standard Deviation (STD) of the performance index in the latest five iterations. Once the STD is lower than the critical value, the index is considered to have reached its convergence, and the computation exits the iteration loop. The critical value is set as 1% of the last performance index in the loop in this thesis, namely err_{critical}=0.01. Furthermore, when the number of iterations reaches n_{critical}=100, the iteration also jumps to the end. The values of err_{critical} and n_{critical} result from the trade-off between computational time and convergence. The CPU time of each iteration is approximately 40.8 seconds. The process is also shown in Fig. 4.2. Fig. 5.4 shows the logarithmic scale of err under

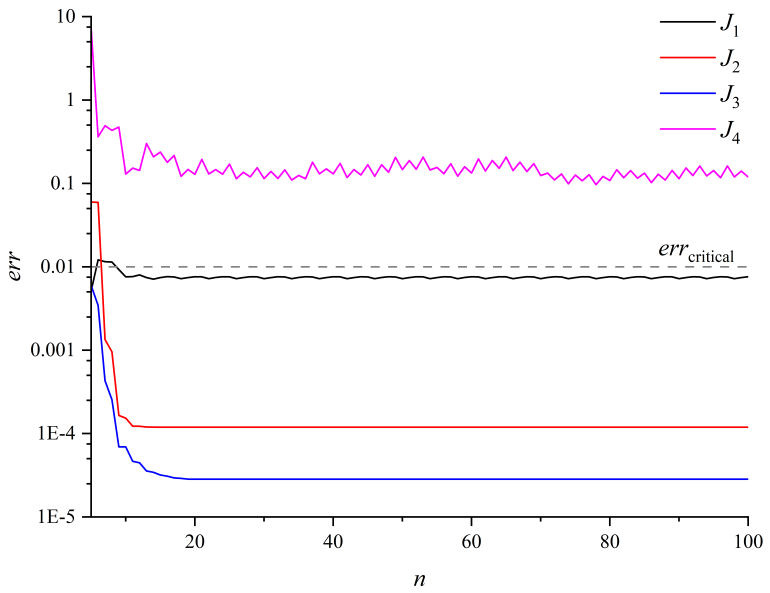

Figure 5.4: The convergence of different objective functions with the number of iterations (The *err* is shown in logarithmic scale).

different objective functions when the wave amplitude is 1 m and the wave frequency is 1 rad/s.

In Fig. 5.4, the *err* of each objective function decreases over time and eventually reaches below the critical value err_{critical}=0.01. The *err* reaches the critical value at different iteration steps, which means the convergence speed of the objective functions varies depending on the objective function selection. $\bar{J}_1$, $\bar{J}_2$, and $\bar{J}_3$ converge quickly and steadily, while $\bar{J}_4$ fails to converge under current criteria. This indicates that the numerical optimisation process for $\bar{J}_4$ requires more iterations to reach convergence compared to other objective functions.

When the objective functions converge quickly, the objective function is typically in a relatively simple form and can be easily optimised, referring to $\bar{J}_1$, $\bar{J}_2$, and $\bar{J}_3$. In these cases, the convergence is relatively fast, and the objective function can be considered to have reached a local optimum. The difference in their *err* after convergence is related to their function forms. On the other hand, when the objective functions converge slowly, such as $\bar{J}_4$, the reason is that it is more sensitive to the PTO control strategy, which introduces more complexity to the numerical optimisation process. According to

Table 5.1: Wave and PTO configurations.

Parameters	Dimensions
Regular wave amplitude, ζ	1 m
Regular wave frequency, ω	1 rad/s
PTO damping coefficient, B_{PTO}	5.2×10^8 Nm·s/rad
PTO restoring coefficient, K_{PTO}	0 Nm·rad

Eq. 5.8, the objective function of $\bar{J}_4$ contains multiple time-variant variables, $B_{\mathrm{d}}(t)$ and $\Delta\dot{\theta}(t)$. The time-variant variables vary in each iteration, thus the objective functions are optimised along a different trajectory in each iteration, which makes it more difficult to converge. The next section will provide a more detailed analysis of their performance.

5.5 Control effect

5.5.1 Control effect comparison

In this section, the configurations of incoming regular wave and PTO system are presented in Tbl. 5.1. The parameters are set to ensure a significant response and control effect under declutching control. The time horizon after convergence, 500 seconds to 540 seconds, is selected to demonstrate the time-domain results. This section focuses exclusively on wave forces and velocities in the pitch direction, which are affected by the PTO system.

Figure 5.5 compares the performance of different objective functions in four corresponding objectives. In Fig. 5.5a, only $\bar{J}_1$ leads to the reduction of $|\dot{\eta}_5^1|$ by 2.94%, while the other three cases result in an increase in $|\dot{\eta}_5^1|$ by more than 539.93%. Therefore, although $|\dot{\eta}_5^1|$ is only minimally optimised, it performs better than other objective functions. In Fig. 5.5b and 5.5c, among the objective functions applied to the control algorithm, $\bar{J}_2$ shows the best performance in maximising P_{wave} and $\bar{J}_3$ has the best performance in maximising $|\Delta\dot{\theta}|$. This suggests that $\bar{J}_2$ is the most effective objective function in maximising P_{wave}, and $\bar{J}_3$ is the most effective in maximising $|\Delta\dot{\theta}|$. In Fig. 5.5d, P_{PTO} experiences the greatest increase when applying $\bar{J}_4$, however, its optimality cannot be guaranteed due to its complexity and slow convergence, as analysed in the

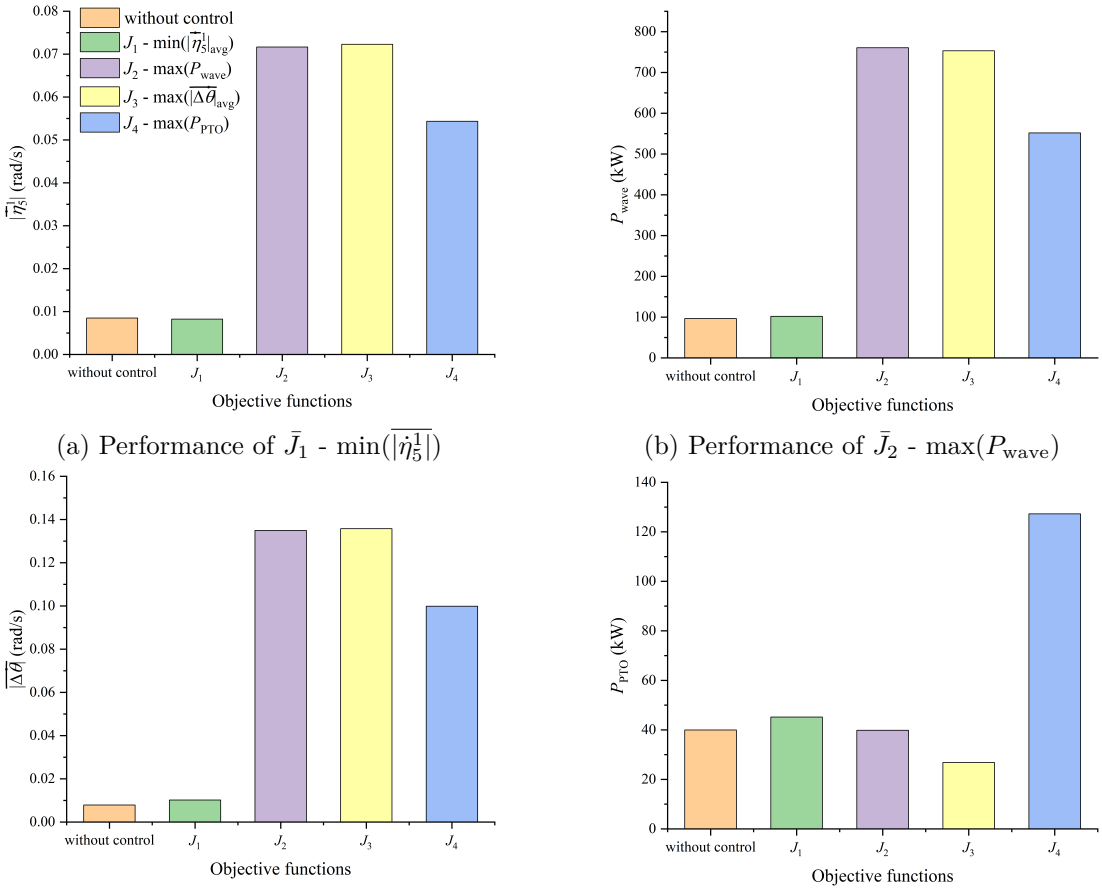

(a) Performance of $\bar{J}_1$ - min($|\overline{\dot{\eta}_5^1}|$)

(b) Performance of $\bar{J}_2$ - max(P_{wave})

(c) Performance of $\bar{J}_3$ - max($|\overline{\Delta\dot{\theta}}|$)

(d) Performance of $\bar{J}_4$ - max(P_{PTO})

Figure 5.5: Performance of $\bar{J}_1$ to $\bar{J}_4$ when applying different objectives.

previous section. In conclusion, each objective function can minimise or maximise its corresponding objective, except $\bar{J}_4$.

In Fig. 5.5a, $\bar{J}_2$ to $\bar{J}_4$ cannot optimise $|\dot{\eta}_5^1|$ to its minimum, indicating that the control effect of $\bar{J}_2$ to $\bar{J}_4$ contradicts that of $\bar{J}_1$. The control effect of $\bar{J}_2$ to $\bar{J}_4$ is to maximise their objectives, resulting in the increase of $|\dot{\eta}_5^1|$ as a by-product. The results of $\bar{J}_2$ and $\bar{J}_3$ are similar in Fig. 5.5a, 5.5b and 5.5c. This implies that $\bar{J}_2$ and $\bar{J}_3$ have similar effects, i.e., the maximisation of wave power extraction and relative rotational speed have similar conditions. However, the performance of objective function $\bar{J}_2$ is 7.76% better than $\bar{J}_3$ when maximising P_{wave} in Fig. 5.5b, while $\bar{J}_3$ is 10.01% better than $\bar{J}_2$ when maximising $\overline{|\Delta\dot{\theta}|}$ in Fig. 5.5c. This suggests that each performance index

can only be optimised when applying its corresponding objective function. The results under other objective functions are suboptimal.

5.5.2 Control effect of J_1

As previously mentioned, $\bar{J}_1$, the pitch motion of Box_1, can be slightly optimised specifically under the current conditions. Figure 5.6 illustrates an example of the control command for $\bar{J}_1$. The command is occasionally 1 throughout the simulation, indicating that the declutching control is successfully applied. When the velocity of Box_1 is larger than that of Box_2, Box_2 provides a damping effect on Box_1 through the PTO between them. However, when the velocity of Box_1 is smaller than that of Box_2, Box_2 provides an actuating effect on Box_1. In essence, the directions of PTO force and Box_1's velocity determine whether the force serves as a damping or an actuating force. If the directions are opposite, the PTO force provides a damping force. Conversely, if they are the same, the PTO force provides an actuating force.

The velocities at the wave frequency of 1 rad/s are shown in Fig. 5.7. However, it is found that the control does not function effectively in this wave frequency. Conversely, the presence of control actually results in an increase in pitch motion. Figure 5.8 shows that when without control, the PTO force is nearly anti-phase with the velocity of Box_1. The declutching control is trying to tune the PTO force to be perfectly anti-phase with the velocity of Box_1, providing a maximum damping force to Box_1.

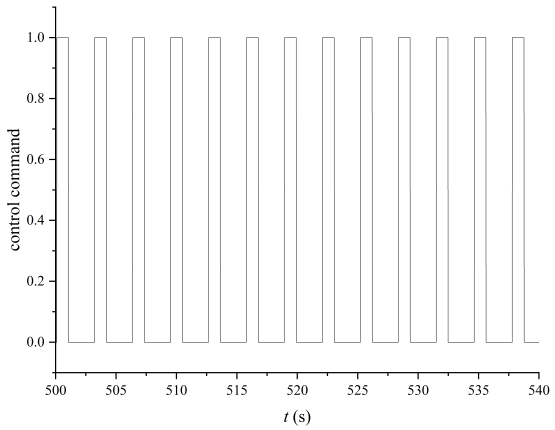

Figure 5.6: Control command when applying $\bar{J}_1$ as the objective function.

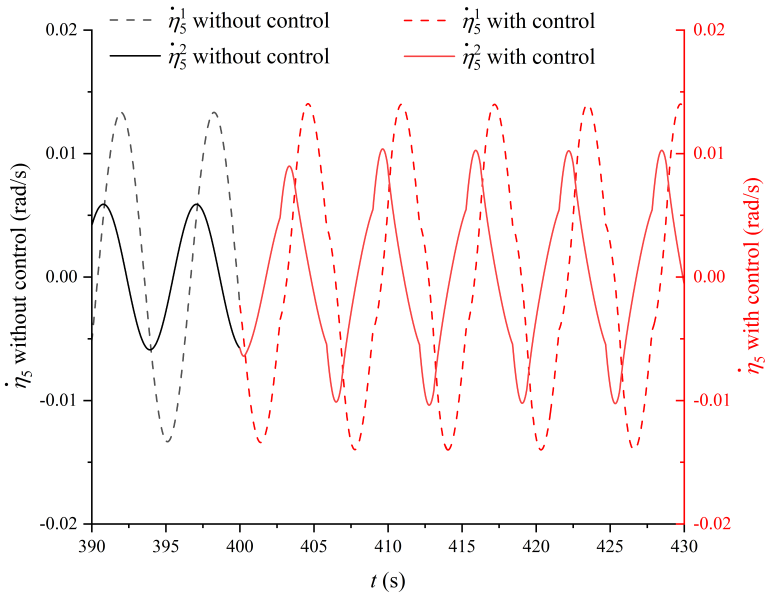

Figure 5.7: The time history of the velocities of the two boxes when ω=1 rad/s.

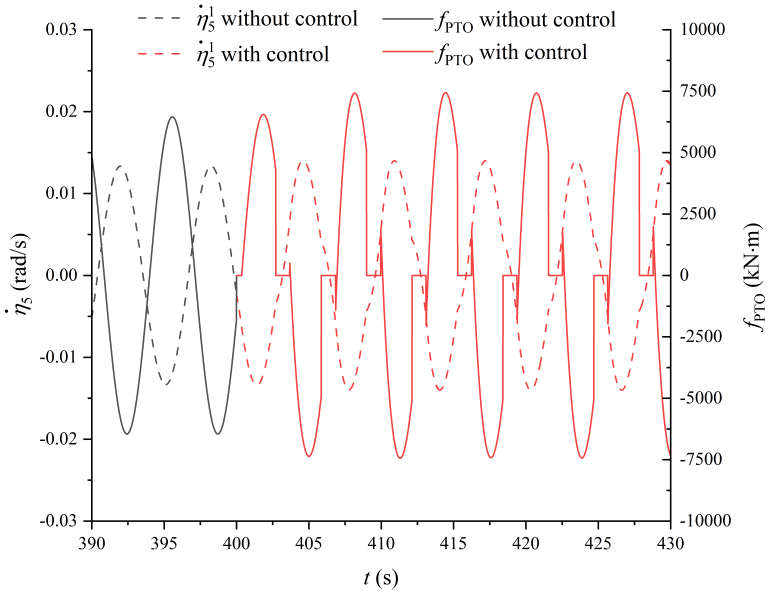

Figure 5.8: The relationship of velocity and PTO force of Box_1 when ω=1 rad/s.

However, there are still sections where the PTO force and the velocity of Box_1 are in phase, leading to an increase in the velocity of Box_1. This issue appears to be caused by inherent limitations within the optimisation algorithm used.

In another special wave frequency of 1.1 rad/s, it is possible to observe an obvious

motion mitigation of Box_1. At this wave frequency, the responses of the two boxes are the same initially, as shown in Fig. 5.9. The declutching control releases the two boxes, making their velocities to be different from each other. The velocity of Box_1 is decreased while that of Box_2 is increased with control. Figure 5.10 shows that there is almost no in-phase horizon between the PTO force and velocity of Box_1 under the current control algorithm. The current control algorithm ensures that the PTO no longer provides actuating force to Box_1.

The phase relationships of wave forces and pitch velocities of the two boxes under $\bar{J}_1$, as illustrated in Fig. 5.11, demonstrate a reduction in wave power absorbed by Box_1, while there's an increase in the power absorbed by Box_2. This energy redistribution, evident between Box_1 and Box_2, is achieved through the implementation of phase control, which adjusts the timing of energy absorption between the two boxes.

5.5.3 Control effect of J_2

$\bar{J}_2$ represents the total power calculated by the product of wave force and body velocity. In most frequencies, the wave force and the body velocity are not in phase with each other. As a result, each of the boxes extracts and dissipates wave energy

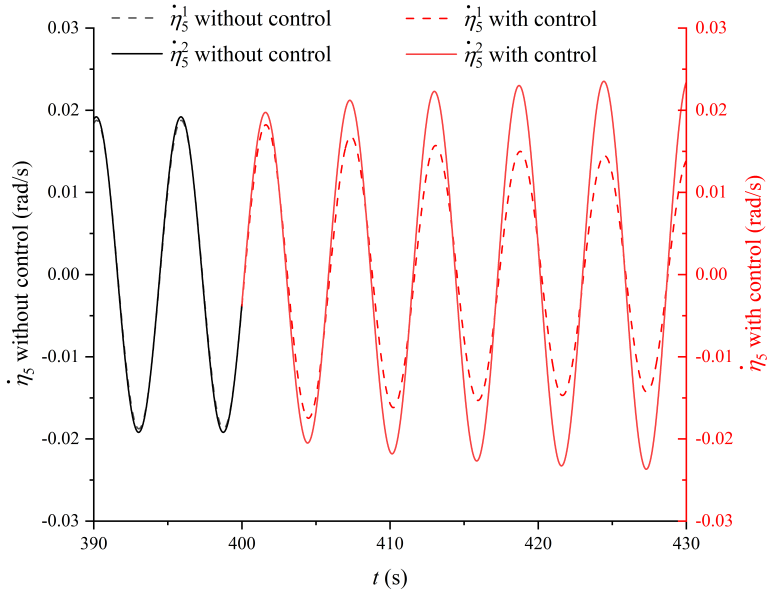

Figure 5.9: The phase relationship when $\omega = 1.1$ rad/s under objective function $\bar{J}_1$.

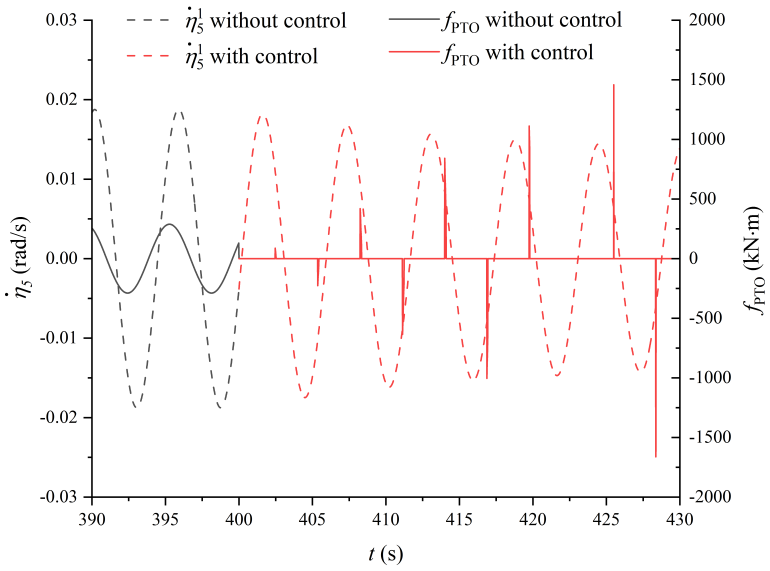

Figure 5.10: The relationship of velocity and PTO force of *Box*_1 when ω=1.1 rad/s.

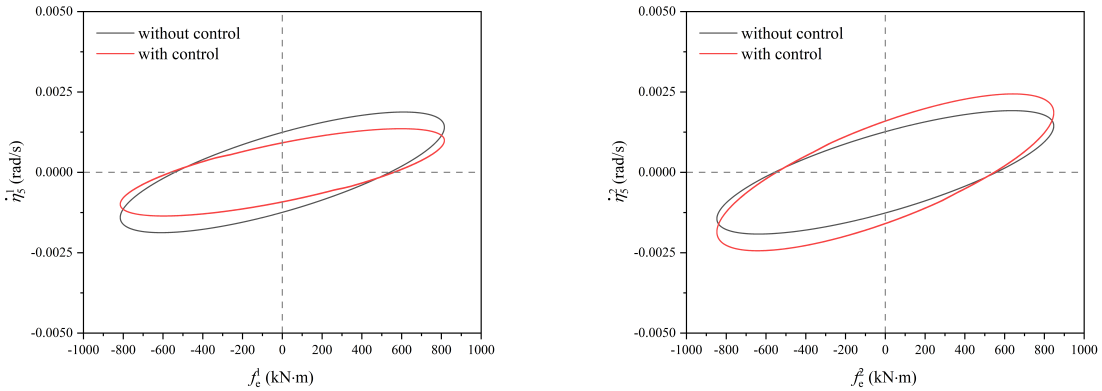

(a) Phase relationship of *Box*_1.

(b) Phase relationship of *Box*_2.

Figure 5.11: The phase relationship of wave forces and pitch velocities of the two boxes under $\bar{J}_1$.

in different time horizons. The wave force f_e will not be influenced by the control algorithm, thus $\bar{J}_2$ is only influenced by the amplitude of velocities and the phase relationship between the wave force and velocity. The effect of declutching control depends on the weighting between the two factors.

According to Fig. 5.12, in the case without control, the wave force and velocity of the boxes are not in phase or anti-phase at the current wave frequency. From the energy conservation point of view, in some time horizons, the system absorbs energy

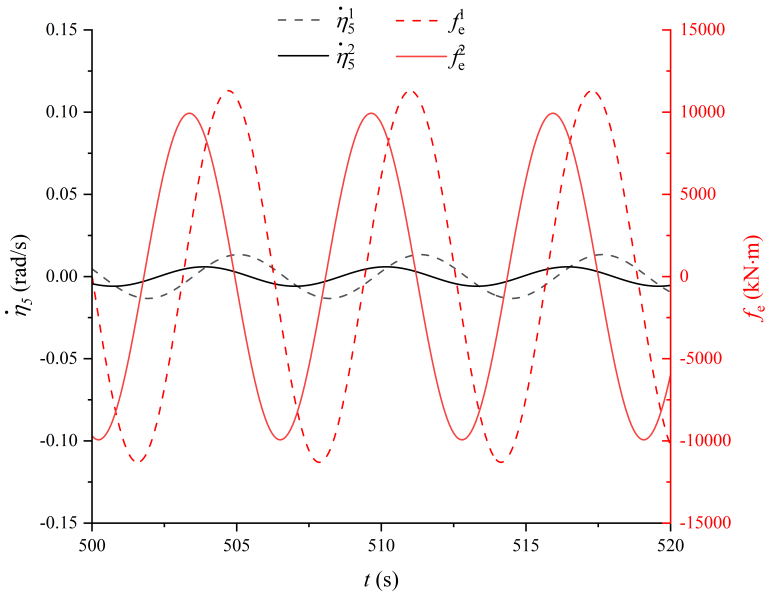

(a) Amplitudes of wave force and velocity without control.

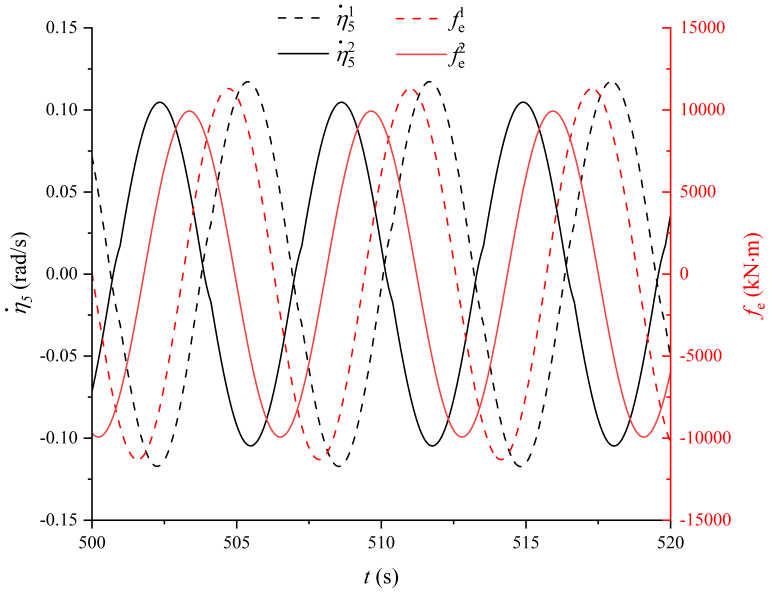

(b) Amplitudes of wave force and velocity with control.

Figure 5.12: The time-domain results with and without control of the two boxes when $\bar{J}_2$ is applied as the objective function.

from the waves, while in others the system dissipates energy to the environment. At the current wave frequency, the weight of amplitudes of velocities is higher, resulting in a slightly changed force-velocity phase relationship and a noticeable increase in the

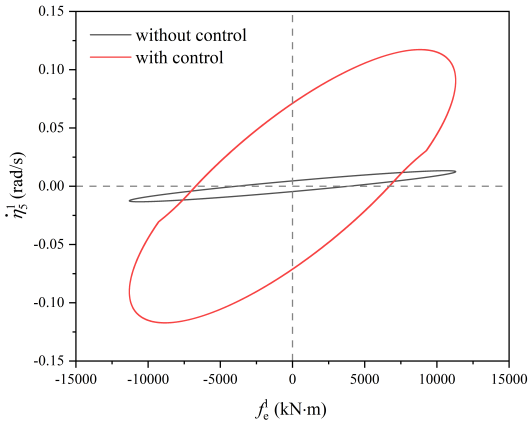

(a) Phase relationship of Box_1.

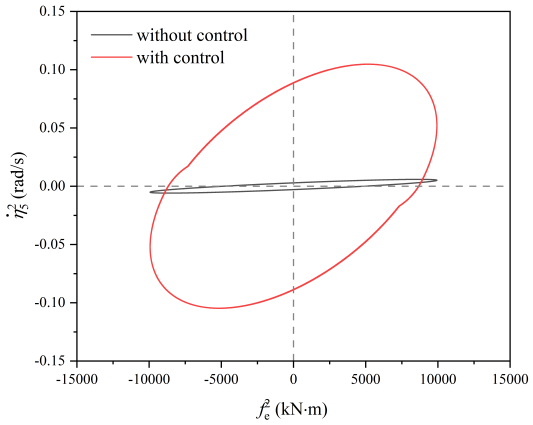

(b) Phase relationship of Box_2.

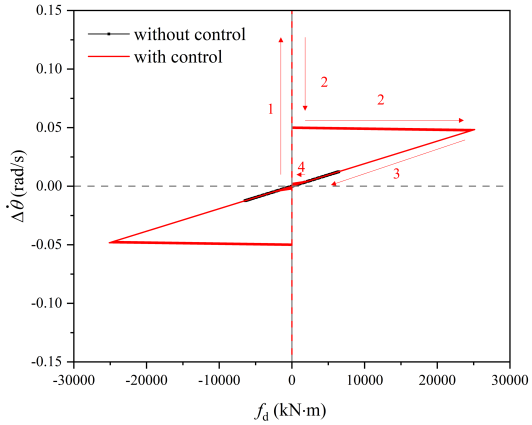

(c) Phase relationship of the relative angular velocity and the PTO force.

Figure 5.13: The phase relationship of wave forces and pitch velocities of the two boxes under $\bar{J}_2$.

velocity amplitudes when control is applied.

Figure 5.13 gives a phase relationship of this trend. The phase relationships in Fig. 5.13a and 5.13b indicate the boxes have reached steady periodical motions. The areas enclosed between curves and x-axis represent the power of wave forces. In quadrants I and III, the wave forces do positive work to the box, whereas in quadrants II and IV, the wave forces do negative work. With optimal declutching control, the positive power extracted from the waves and the negative power released to the wave are both increased. However, the total power increases compared to the case without control.

Figure 5.13c shows the control results when applying $\bar{J}_2$ as the objective function.

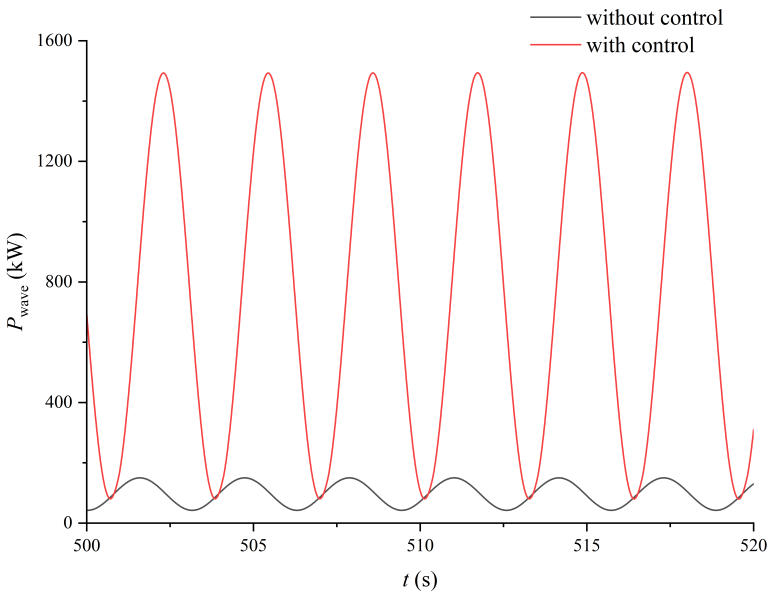

Figure 5.14: Total wave power extracted by boxes when ω=1 rad/s.

The damping force of PTO under declutching control is $f_{\mathrm{d}}(t) = B_{\mathrm{d}}(t)\Delta\dot{\theta}(t)$. In Fig. 5.13c, $\Delta\dot{\theta}$ varies regularly with f_{d}. The area under the curves in this plot represents the power of PTO force. Notably, the horizontal and vertical lines in the plot represent the switch between the binary state of 0 and 1 in declutching control. As the switching time is negligible, these lines can be excluded when computing the power. During the unloading of f_{d}, $\Delta\dot{\theta}$ increases along vertical line 1. Subsequently, $\Delta\dot{\theta}$ undergoes a sudden decrease along the vertical portion of line 2 as f_{d} is reloaded. Meanwhile, f_{d} transiently accelerates to a constant value along the horizontal portion of line 2. While reducing $\Delta\dot{\theta}$, f_{d} exerts positive power on the PTO system (line 3). Once $\Delta\dot{\theta}$ is too small, f_{d} is unloaded again (line 4). The lines in quadrant 3 undergo the same process as in quadrant 1.

Figure 5.14 provides further clarification on the change in extracted wave power. The positions of peak and valley of the wave power extraction in different from those without control. The average wave power is increased by 689.90%, which can also be observed in Fig. 5.7.

In another special wave frequency of 0.8 rad/s, the wave force and velocity of Box_1 are initially in phase with the current wave frequency, whereas those of Box_2 are anti-

phase (in 5.15a). The weighting of force-velocity phase is higher at this frequency, thus the control effect will be different from above. The wave forces perform positive work on Box_1 and negative work on Box_2. From the energy conservation point of view,

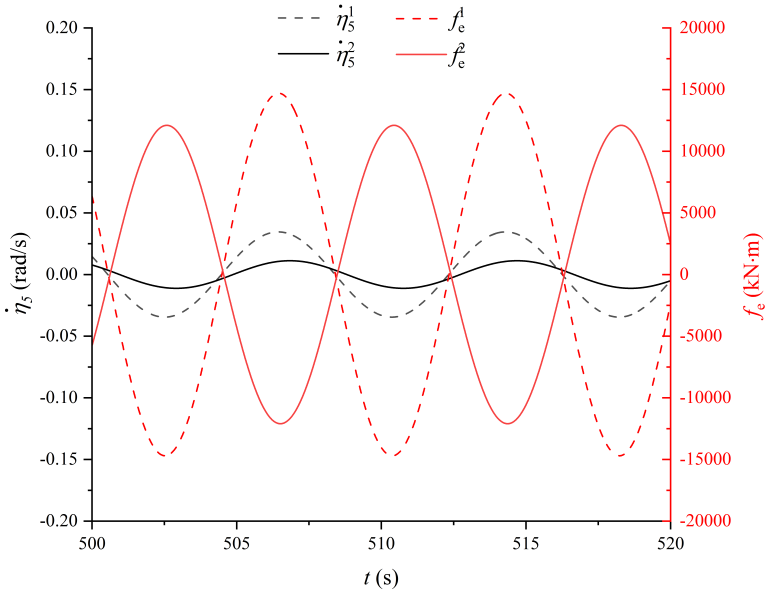

(a) Phase relationship of wave force and velocity without control.

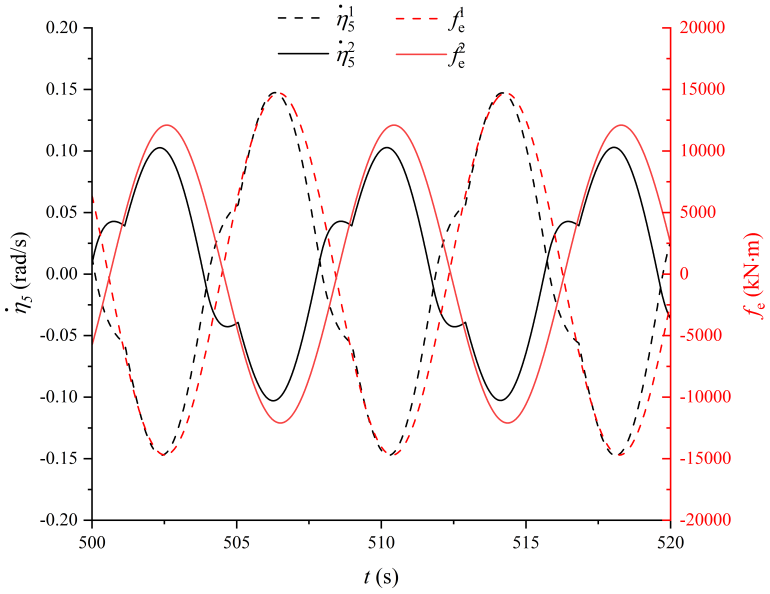

(b) Phase relationship of wave force and velocity with control.

Figure 5.15: The time-domain results with and without control of the two boxes when ω=0.8 rad/s.

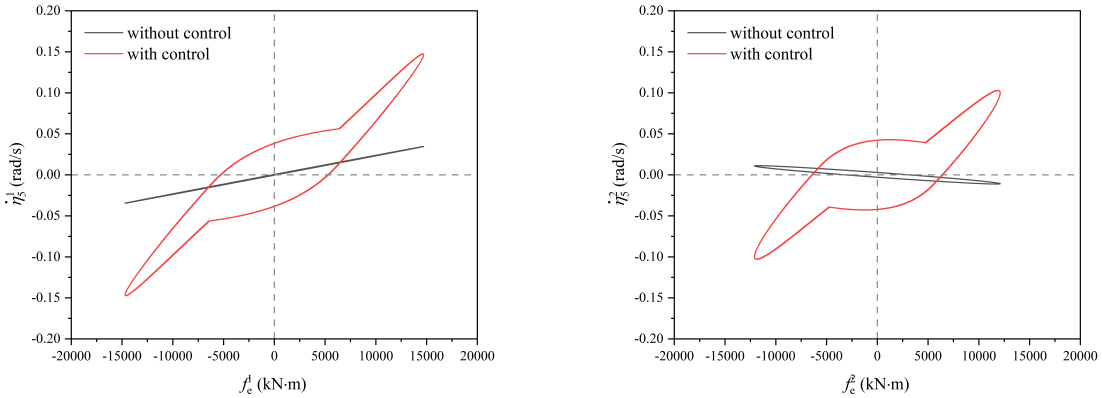

(a) Phase relationship of *Box*_1. (b) Phase relationship of *Box*_2.

Figure 5.16: The phase relationship of wave forces and pitch velocities of the two boxes when ω=0.8 rad/s.

*Box*_1 keeps absorbing energy from the waves, while *Box*_2 keeps dissipating energy to the environment. The optimal declutching control tunes the phase between the wave force and body velocity to maximise $\bar{J}_2$. The in-phase horizon of *Box*_2 increases while that of *Box*_1 decreases slightly. The amplitudes of velocities are also increased. The phase relationships in Fig. 5.16 indicate that with optimal declutching control, the positive power extracted from the waves and the negative power released to the wave are both increased. However, the total power increases compared to the case without control. Figure 5.17 provides further clarification on the change in extracted wave power. The positive and negative wave power are both increased, and the average wave power is increased.

5.5.4 Control effect of J_3

$\bar{J}_3$ represents the relative angular velocity between two boxes. Figure 5.18 shows that when without control, the average relative angular speed $\left|\Delta\dot{\theta}\right|$ is monotonically decreasing with B_{PTO} in regular waves, implying the increase of damping force will cause a reduction in relative motions. It can be anticipated that when B_{PTO} tends to be infinite, the relative angular velocity between the hinged bodies will tend to be 0. Since declutching control can reduce the average value of B_{PTO}, it can effectively maximise $\left|\Delta\dot{\theta}\right|$. It should be noted that Fig. 5.18 only depicts the trend of $\left|\Delta\dot{\theta}\right|$. The

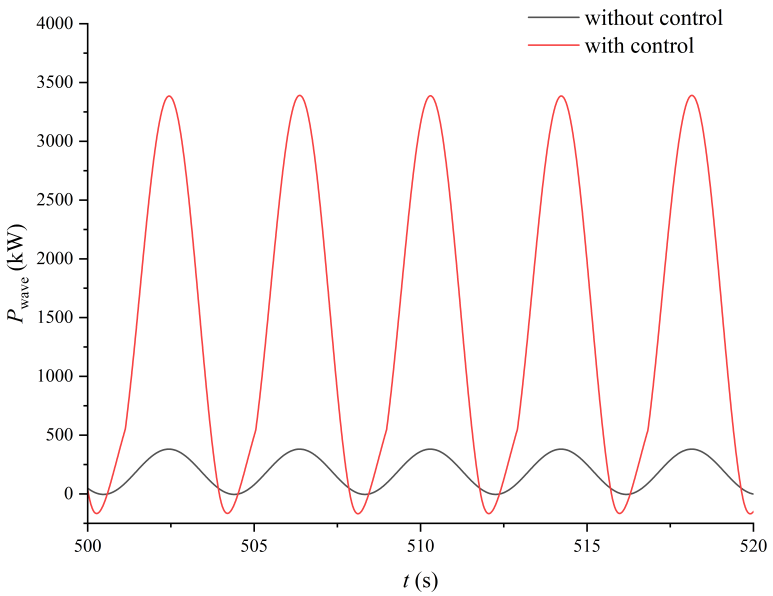

Figure 5.17: Total wave power extracted by boxes when ω=0.8 rad/s.

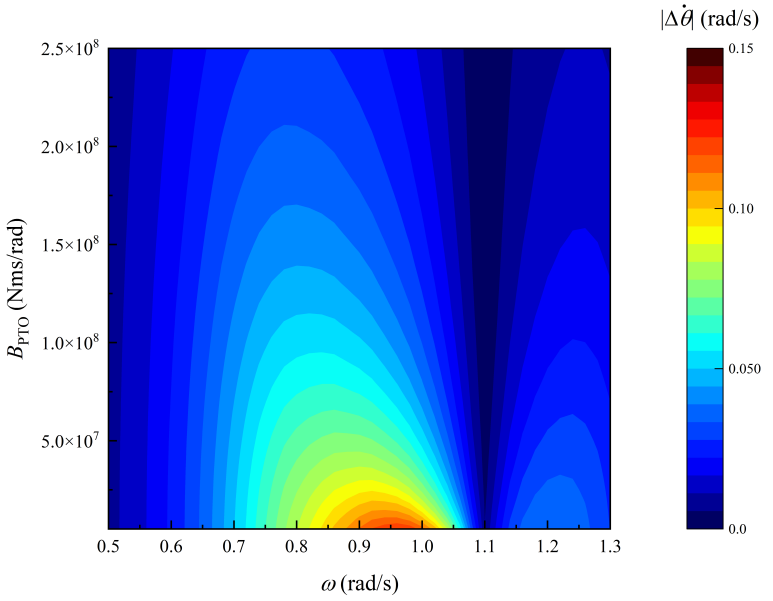

Figure 5.18: Average relative angular speed under different PTO damping coefficients and wave frequencies without declutching control.

B_{PTO} used for control in this section, which is 5.2×10^8 Nm·s/rad, is not included in this figure.

Figure 5.19 shows the phase relationship of the velocities of the two boxes and their

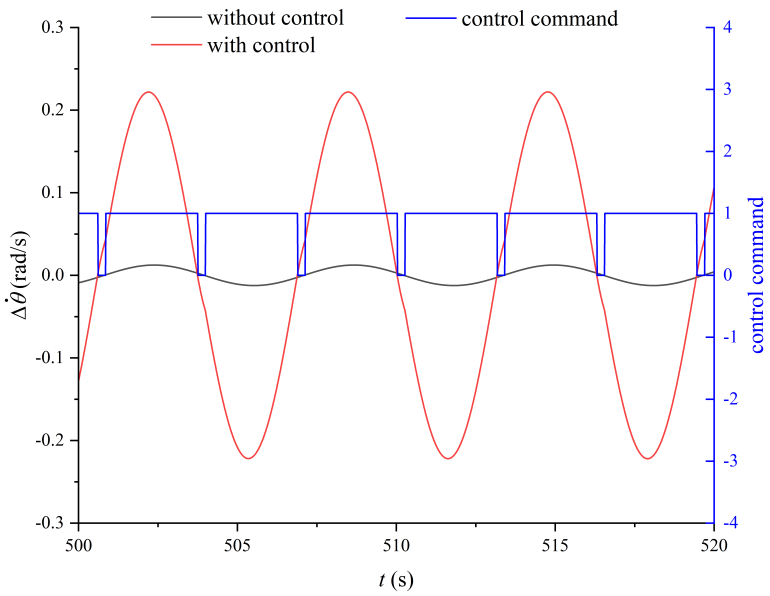

Figure 5.19: The time-domain results with and without control of the two boxes when $\bar{J}_3$ is applied as the objective function.

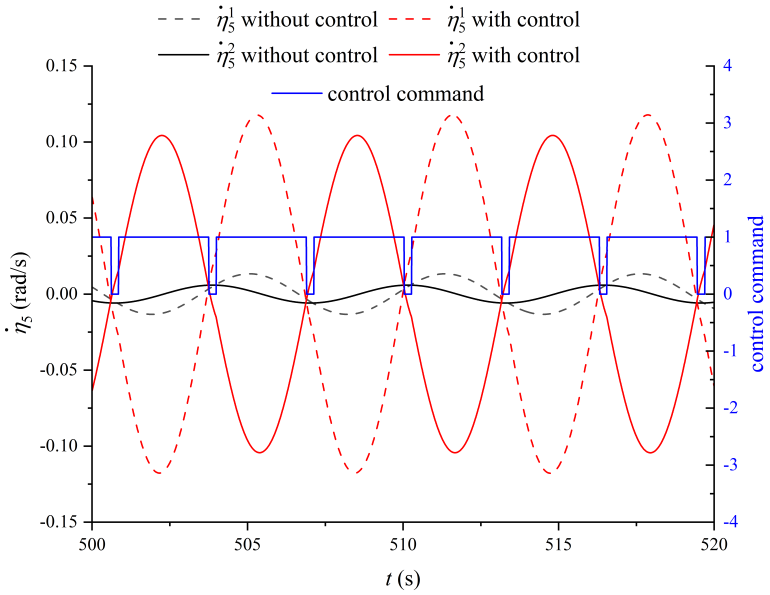

Figure 5.20: The time-domain results of the relative angular velocity with and without control. The results are compared with the control command (blue line).

relationship with the control command. The maximisation of $\left|\Delta\dot{\theta}\right|$ depends on the velocity amplitude of each box and the velocities' phase relationship. The velocities initially have a phase difference without control, however, with the application of the

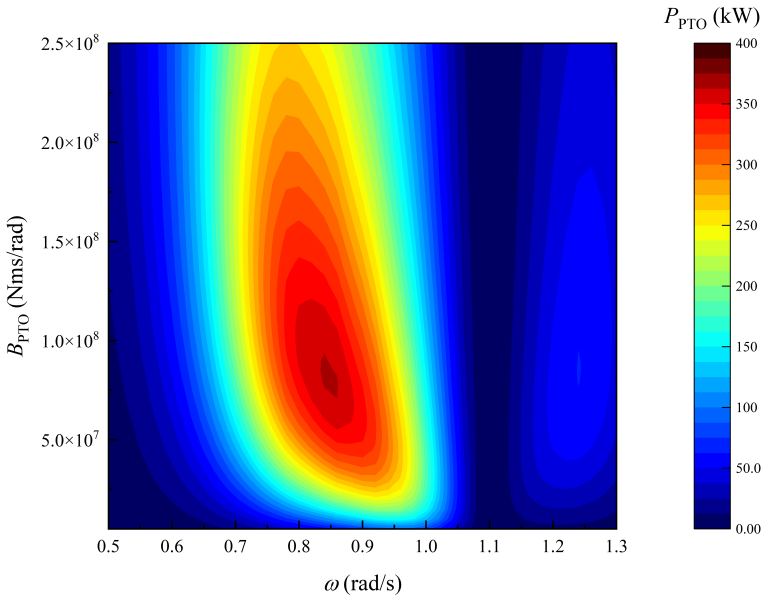

Figure 5.21: Power absorption under different PTO damping coefficients and wave frequencies without declutching control.

control strategy, they eventually become anti-phase. When the control command is 1, the optimal declutching control increases the amplitude of the velocities and tunes them anti-phase to maximise $\left|\Delta\dot{\theta}\right|$. When the velocities increase in opposite directions, $\left|\Delta\dot{\theta}\right|$ also increases, and no control is needed, thus the command is 0 during this time period. When both velocities decrease and $\left|\Delta\dot{\theta}\right|$ starts to decrease, the control command turns back to 1. The time history of $\Delta\dot{\theta}$ in Fig. 5.20 demonstrates the amplification effect of the declutching control on the relative angular velocity.

5.5.5 Control effect of J_4

In a single-body system, the velocity of the body is equivalent to the velocity of the PTO, therefore, the in-phase relationship between the body velocity and wave force leads to the maximisation of PTO power output. However, in a multi-body system, the PTO system is installed at the hinge connection between bodies, and the power is generated from the relative motion. Thus, optimising the PTO power output $\bar{J}_4$ of a multi-body system is different from optimising wave energy absorption $\bar{J}_2$.

Figure 5.21 illustrates the sensitivity of average power to the PTO damping coeffi-

cient B_{PTO} in regular waves without control. According to Eq. 3.4, the average power is determined by B_{PTO} and relative angular velocity $\Delta\dot{\theta}$. The damping coefficient B_{PTO} influences both the velocity $\Delta\dot{\theta}$ and the PTO power output, therefore, the influence of B_{PTO} is nonlinear and noticeable. There is one maximum power absorption at each wave frequency when without control. When B_{PTO} is set to the damping coefficient of 8.5×10^7 Nm·s/rad and the wave frequency is at 0.84 rad/s, the system reaches its maximum electric power output.

Optimal declutching control can realise the effect of tuning dynamically the average damping coefficient to its optimum. In Fig. 5.22c, $\Delta\dot{\theta}$, the relative rotation velocity, shows an irregular variation in relation to the controlled damping force f_{d}. However, the summation of the positive power (total power of PTO) is still enhanced. This effect can be directly observed in Fig. 5.23, which demonstrates the power output of PTO force under declutching control of $P_{\mathrm{PTO}}(t) = f_{\mathrm{d}}(t)\Delta\dot{\theta}(t)$. Although the average time spent producing positive power decreases, both the instantaneous power and the total power generated are higher.

Figure 5.24 demonstrates the power distribution in the time horizon of 500 s to 544 s, which is approximately 7 wave periods. The results show that the optimal declutching control enhances both the total wave power absorbed by the hinged box system and the power output generated by the system. The summation of power generated by inertial force, radiation force, restoring force, and PTO force is proximate to the total wave power. The proportions of inertial and restoring power are low because kinetic and potential energy does not accumulate over entire periods. Since the radiation force and PTO force are non-conservative, their average power increases with the chosen time horizon. In the current time horizon, the percentage of PTO power increases from 8.86% to 15.68%, indicating that the distribution of wave energy components is beneficial to energy absorption under the optimal declutching control method.

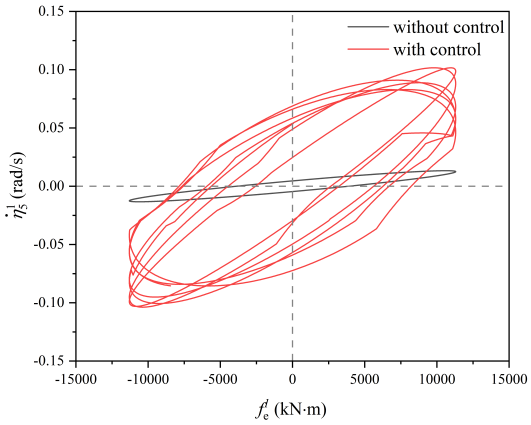

(a) Phase relationship of Box_1.

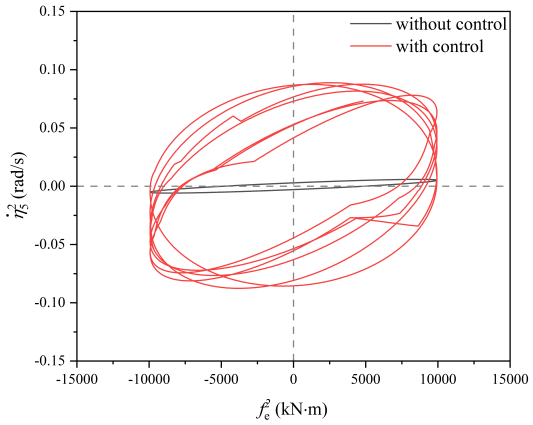

(b) Phase relationship of Box_2.

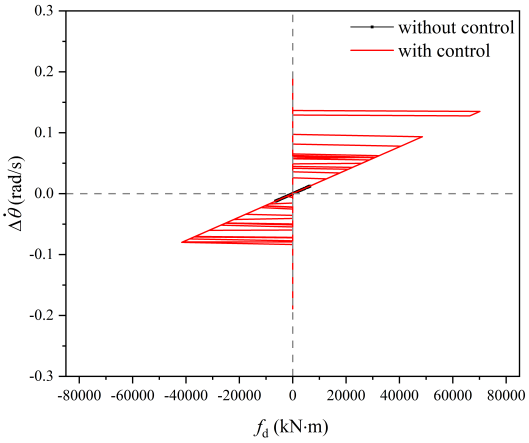

(c) Phase relationship of the relative angular velocity and the PTO force.

Figure 5.22: The phase relationship of wave forces and pitch velocities of the two boxes under $\bar{J}_4$.

5.6 Control effect in different wave frequencies

Figure 5.25 illustrates the numerical optimisation effects of different performance indices in different wave frequencies. The results are optimised under their respective objective functions. In general, Fig. 5.25 shows when the optimal declutching control is applied to the system, all the objectives can be achieved. However, it should be noted that the effect of the control depends on the wave conditions. It indicates that in certain wave frequencies, the control strategy proposed in this study can effectively be applied to control the multiple floating bodies with different application scenarios.

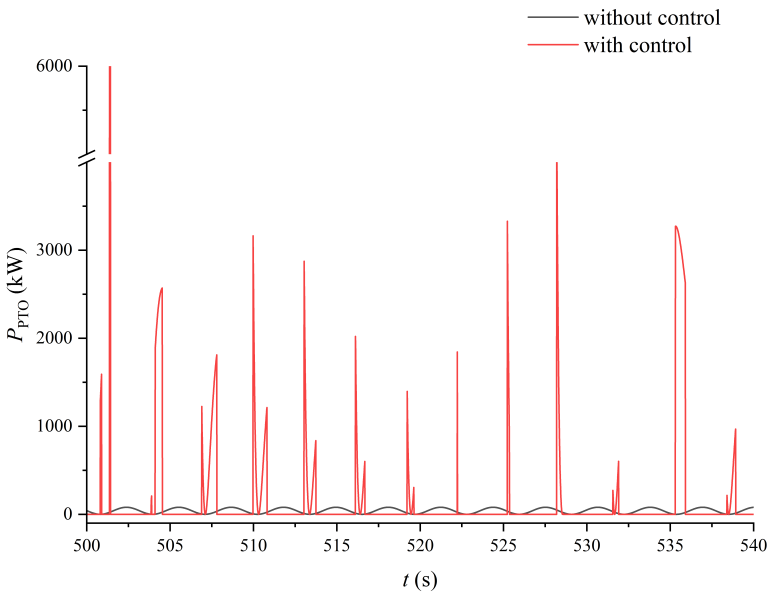

Figure 5.23: Time history of the total power absorbed by PTO.

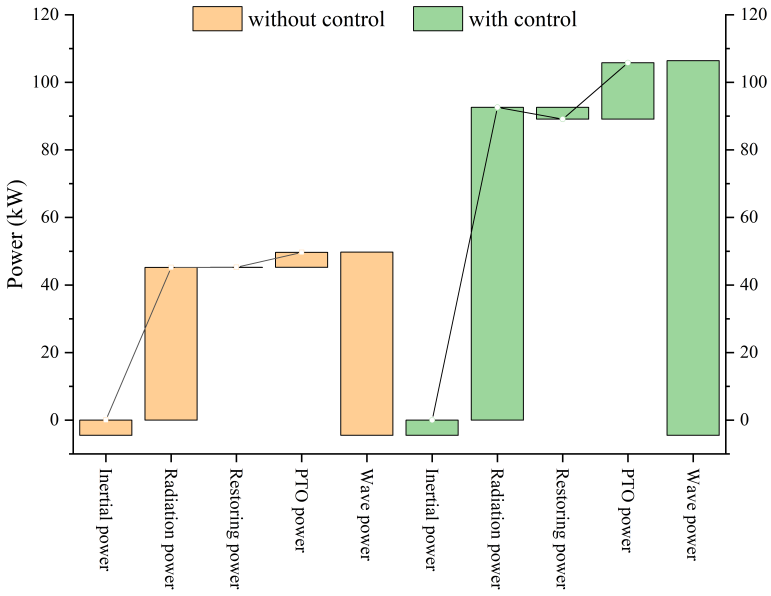

Figure 5.24: The distribution of wave energy extracted or dissipated by the hinged box system without (left) and with control (right).

In Fig. 5.25a, $|\dot{\eta}_5^1|$ can be optimised at frequencies ranging from 1.0 to 1.15 rad/s. The wavelength in this range is approximately equal to the distance between the CoGs of the boxes, which is 50 m. Therefore, the boxes experience similar wave forces, and their velocities are also similar. As stated in previous section, the PTO provides an

actuating force to the Box_1 which amplifies Box_1's motion in this condition. The declutching control releases the two boxes and minimises $|\dot{\eta}_5^1|$ by reducing the total force in the direction of its velocity. In other wave frequency ranges, the PTO force acting on Box_1 provides a damping effect most of the time to reduce its motion. Therefore, declutching control cannot reduce the pitch speed of Box_1 by releasing the PTO force at these frequencies. In the process of numerical optimisation, the control command for $\bar{J}_1$ is 0 nearly throughout the simulation under these wave conditions, indicating that the objective has reached its optimum. In this situation, applying declutching control will increase $|\dot{\eta}_5^1|$.

In Fig. 5.25b, P_{wave} can be maximised at most wave frequencies except 1.1 to 1.25 rad/s. In the frequency range of 1.1 to 1.25 rad/s, the wave forces of the boxes have similar magnitude, and so do the velocities of the boxes. However, declutching control has a converse effect on the velocity phase of the two boxes. While the phase of Box_1 moves forward, that of Box_2 will move backwards and vice versa. They cannot be in phase with their wave force simultaneously. Thus, the convergence in this range will be slow and reach the largest iteration number n_{critical}. The results with control will be not well optimised. In other wave frequencies, there are larger differences in the boxes' velocity amplitudes and phases, thus their weightings are different. This leads to a clear numerical optimisation direction and faster convergence.

Figure 5.25c shows that $\left|\Delta\dot{\theta}\right|$ can be effectively optimised at all wave frequencies under $\bar{J}_3$. The optimal declutching control process can tune the average value of $B_{\text{d}}(\beta, t)$ to the desired optimal B_{PTO}. According to Fig. 5.18, the decrease of B_{PTO} will cause an increase in $\left|\Delta\dot{\theta}\right|$. The declutching control can reduce the average B_{PTO} at any wave frequency, therefore, optimal declutching control is applicable in all the wave frequencies. When the wave frequency is around 0.8 rad/s, the wavelength (100 m) is approximately twice the distance (50 m) between the CoGs of boxes. Therefore, the boxes experience opposing wave forces, and the directions of their velocities are also opposite. In Fig. 5.25c, the best performance can be observed around 0.8 rad/s in the curve without control. The peak of the curve with control is at a different frequency (0.88 rad/s) because the average damping coefficient is lower with control.

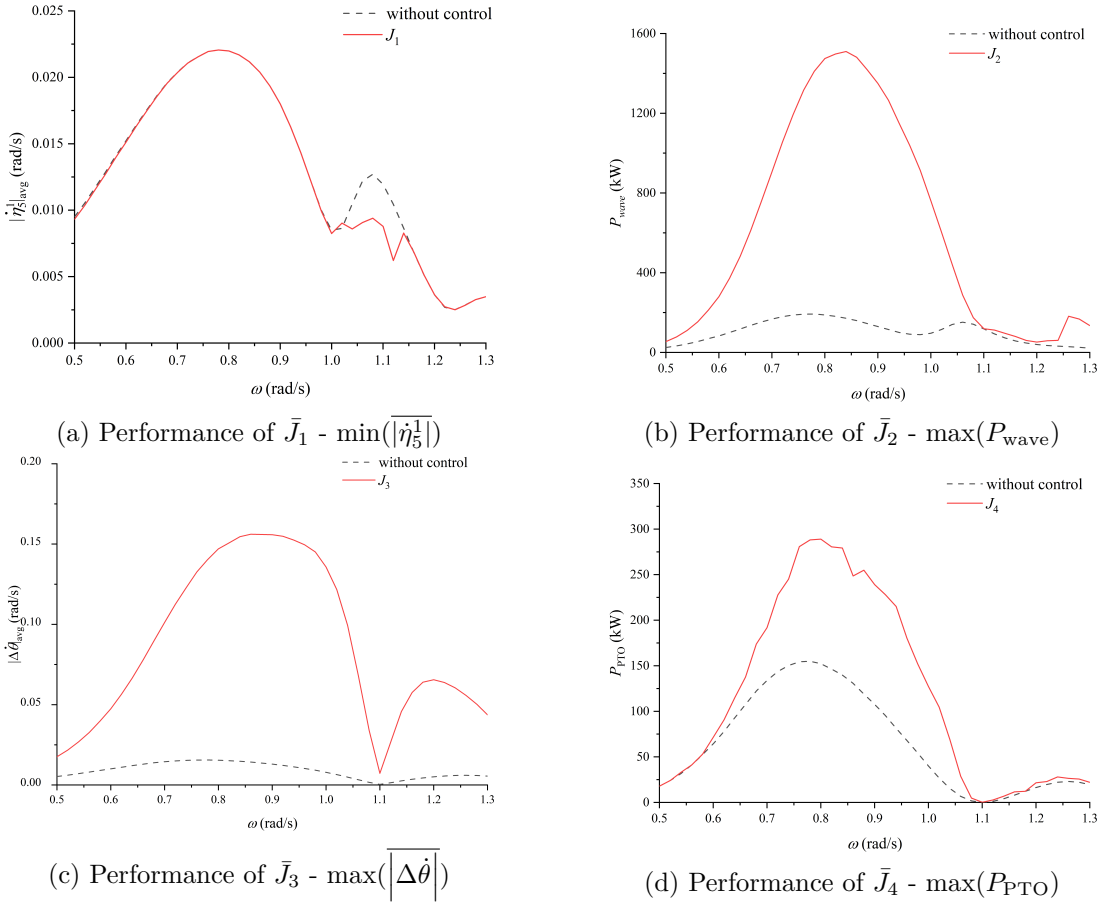

(a) Performance of $\bar{J}_1$ - min($\overline{|\dot{\eta}_5^1|}$)

(b) Performance of $\bar{J}_2$ - max(P_{wave})

(c) Performance of $\bar{J}_3$ - max($\overline{\left|\Delta\dot{\theta}\right|}$)

(d) Performance of $\bar{J}_4$ - max(P_{PTO})

Figure 5.25: Performances of different objective functions in different wave frequencies.

Figure 5.25d illustrates that the power generation of PTO is improved when $\bar{J}_4$ is applied as an objective function of the control system. The improvement covers a wide wave frequency range from 0.6 to 1.1 rad/s. The best control performance is observed at frequencies around 0.8 rad/s, where the P_{PTO} without control is the highest, which is also shown in Fig. 5.21. The declutching control shortens the oscillation period of the floating body, making it resonant at high-frequency waves. The optimal frequency, at which the best control performance occurs, is determined by the PTO power absorption characteristics of the system. However, as stated in the previous section, the objective function of $\bar{J}_4$ contains multiple time-variant variables, $B_{\text{d}}(\beta, t)$ and $\Delta\dot{\theta}(t)$, therefore, $\bar{J}_4$ is difficult to converge under the current optimal control method. The discontinuity and nonlinearity of objective function increase the complexity of this control strategy.

Although P_{PTO} is well increased with the objective function $\bar{J}_4$, the result cannot be regarded as optimal.

5.7 Robustness validation in irregular waves

This section discusses the application of the developed control method under irregular wave conditions. Regular waves can be used to develop, evaluate, and exemplify the control method, but they do not exist in reality. Therefore, the validation of the control approach is necessary under irregular wave conditions, to ensure its applicability and effectiveness in practice. Herein, we present the time-domain results of various parameters like velocities, positions, forces, powers, and so on, in irregular waves.

Irregular waves were modelled using a superposition of several regular waves with random phases [82]. The generated wave profile was ensured to statistically represent real sea states by matching with the energy spectrum of standard sea states. The Jonswap wave spectrum is selected to generate irregular waves in this section. The significant wave height Hs is 3.05 m, and the peak period Tp is 8.9 s, which are representative conditions for a rough sea state. Selecting such a sea state aims to validate

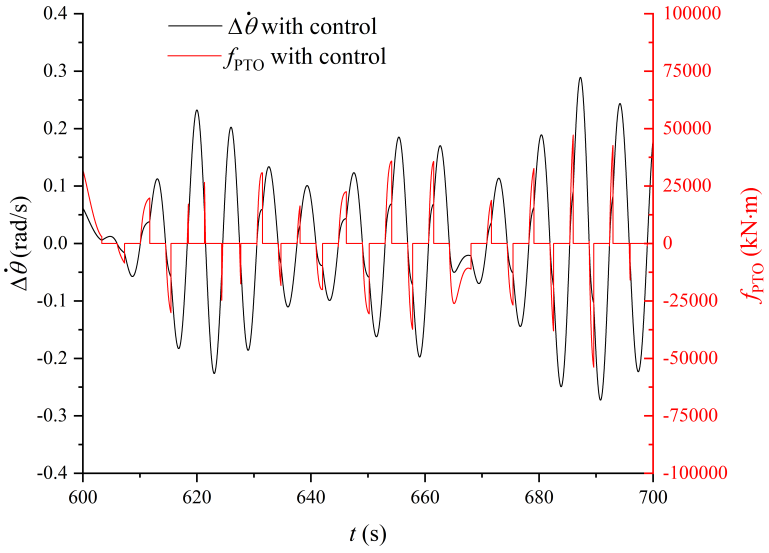

Figure 5.26: Time history of the relative rotational velocity and the PTO force in irregular waves.

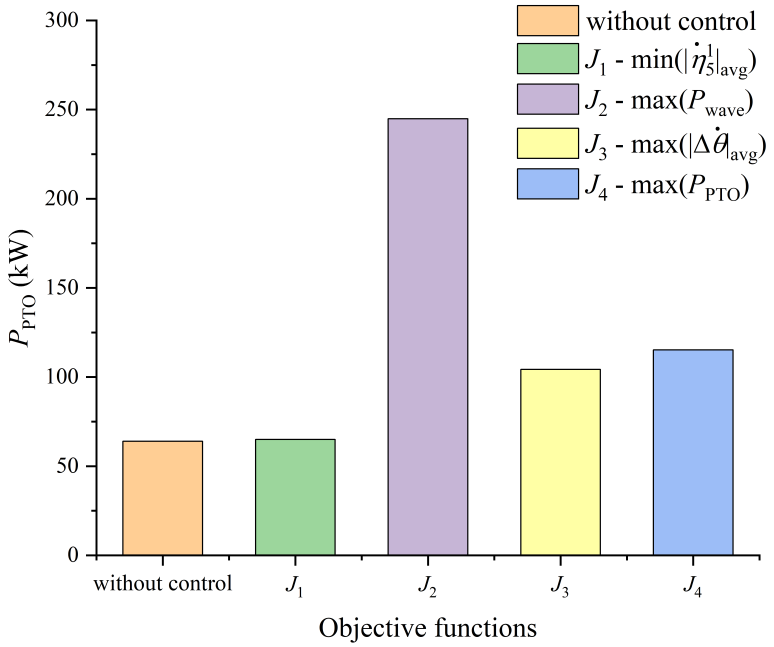

Figure 5.27: Comparison of the total power absorbed by PTO in irregular waves.

the control method's performance and robustness. Analysis of other sea states (mild, moderate, and high) could be conducted in further research to provide a comprehensive assessment of the system's capabilities. Take objective function $\bar{J}_2$ for example, the results $\Delta\dot{\theta}$ and f_{PTO} maintain the relationship of partly in-phase with our control method, which can be revealed from Fig. 5.26.

When averaged over time, the results from irregular waves were compared under different objective functions, as shown in Fig. 5.27. Similar to the control effect in Fig. 5.7 (d), the energy extracted by the PTO of $\bar{J}_2$ to $\bar{J}_4$ shows a remarkable 63.02% to 282.88% improvement when the system operated in irregular waves, implying the robustness and adaptability of the control method. The higher values of P_{PTO} in irregular waves validate the control method's efficiency in enhancing the power extraction of PTO. In comparison with other objective functions, $\bar{J}_4$ demonstrates the second-best performance in enhancing P_{PTO} (80.23%). As stated in the previous section, the objective function of $\bar{J}_4$ contains multiple time-variant variables, making it difficult to converge. The convergence under $\bar{J}_2$ and $\bar{J}_4$ is compared in Fig. 5.28, where $\bar{J}_2$ shows a better convergence. Therefore, the power extraction performance under $\bar{J}_2$ is better.

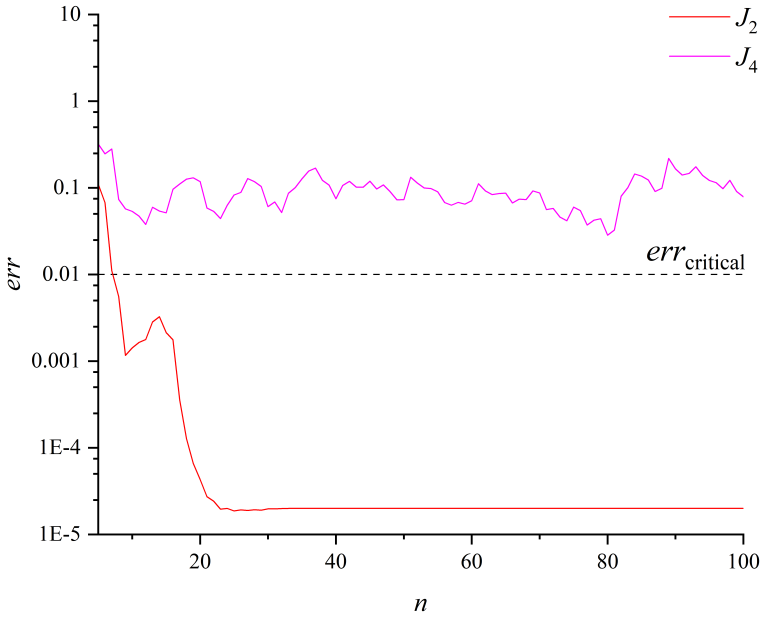

Figure 5.28: The convergence of $\bar{J}_2$ and $\bar{J}_4$ in irregular waves (The *err* is shown in logarithmic scale).

5.8 Extended discussion of a three-body system

The model of a hinged three-body system can be illustrated as a segment of N-body system, as shown in Fig. 5.29. For a three-body system, the total constraint matrix is the product of the individual constraint matrices. Consequently, the system state matrix can be reformulated as,

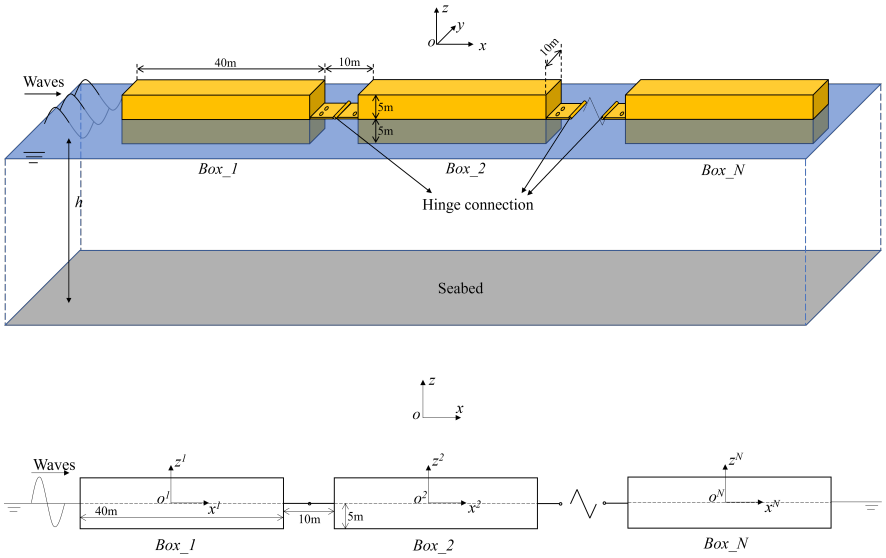

Figure 5.29: Configuration of N hinged boxes.

$$
\begin{aligned}
\boldsymbol{\eta} = \begin{bmatrix} \boldsymbol{\eta}^1 \\ \boldsymbol{\eta}^2 \\ \boldsymbol{\eta}^3 \end{bmatrix} &= \begin{bmatrix} \boldsymbol{I} & \boldsymbol{0} & \boldsymbol{0} \\ \boldsymbol{0} & \boldsymbol{I} & \boldsymbol{0} \\ \boldsymbol{0} & \boldsymbol{S}_{21} & \boldsymbol{S}_{22} \end{bmatrix} \begin{bmatrix} \boldsymbol{\eta}^1 \\ \boldsymbol{\eta}^2 \\ \boldsymbol{\Delta\theta}^2 \end{bmatrix} \\
&= \begin{bmatrix} \boldsymbol{I} & \boldsymbol{0} & \boldsymbol{0} \\ \boldsymbol{0} & \boldsymbol{I} & \boldsymbol{0} \\ \boldsymbol{0} & \boldsymbol{S}_{21} & \boldsymbol{S}_{22} \end{bmatrix} \begin{bmatrix} \boldsymbol{I} & \boldsymbol{0} & \boldsymbol{0} \\ \boldsymbol{S}_{21} & \boldsymbol{S}_{22} & \boldsymbol{0} \\ \boldsymbol{0} & \boldsymbol{0} & \boldsymbol{I} \end{bmatrix} \begin{bmatrix} \boldsymbol{\eta}^1 \\ \boldsymbol{\Delta\theta}^1 \\ \boldsymbol{\Delta\theta}^2 \end{bmatrix} \\
&= \begin{bmatrix} \boldsymbol{I} & \boldsymbol{0} & \boldsymbol{0} \\ \boldsymbol{S}_{21} & \boldsymbol{S}_{22} & \boldsymbol{0} \\ \boldsymbol{S}_{21}\boldsymbol{S}_{21} & \boldsymbol{S}_{21}\boldsymbol{S}_{22} & \boldsymbol{S}_{22} \end{bmatrix} \begin{bmatrix} \boldsymbol{\eta}^1 \\ \boldsymbol{\Delta\theta}^1 \\ \boldsymbol{\Delta\theta}^2 \end{bmatrix} = \boldsymbol{S} \begin{bmatrix} \boldsymbol{\eta}^1 \\ \boldsymbol{\Delta\theta}^1 \\ \boldsymbol{\Delta\theta}^2 \end{bmatrix} = \boldsymbol{S}\boldsymbol{\eta}'
\end{aligned}
\tag{5.10}
$$

The motion equation remains the same form as Eq. 3.15 with an extended input $\boldsymbol{f}_{\mathrm{e}}(t) = [f_{\mathrm{e}}^1(t), f_{\mathrm{e}}^2(t), f_{\mathrm{e}}^3(t)]^{\mathrm{T}}$ and state vector $\boldsymbol{\eta}'(t) = [\eta^1(t), \Delta\theta^1(t), \Delta\theta^2(t)]^{\mathrm{T}}$. The input regular waves have the same configuration as in Section 5.5. The amplitude of the wave excitation force on Box_3, denoted as $f_{\mathrm{e}}^3(t)$, is relatively smaller than those acting on Box_1 and Box_2. The expanded DoF of the three-body system is

8. Besides, the interactions among the three bodies should also be considered in the analysis.

Each pair of adjacent bodies is interconnected by a single PTO unit. Under the assumption that both PTOs have an identical configuration, the total power output of the two units is expressed as follows,

$$P_{\mathrm{PTO}} = \frac{1}{T}\int_0^{\mathrm{T}} \left[(B_{\mathrm{PTO}} + \beta^1 B_{\mathrm{c}})(\Delta\dot{\theta}^1)^2 + (B_{\mathrm{PTO}} + \beta^2 B_{\mathrm{c}})(\Delta\dot{\theta}^2)^2\right] dt \tag{5.11}$$

where β^1 and is the control command for the PTO between Box_1 and Box_2, while β^2 corresponds to the control command for the PTO between Box_2 and Box_3.

The optimal control for the three-body system is implemented using objective function $\bar{J}_4$, which represents the maximisation of the total PTO power output in Eq. 5.11. The control command results are illustrated in Fig. 5.30. This figure shows that the two PTOs have different control behaviours during the control process, aiming to maximise the overall system performance. Figure. 5.31 displays the variation of err and P_{PTO} with iteration. The results indicate a slow convergence, yet an overall improvement in

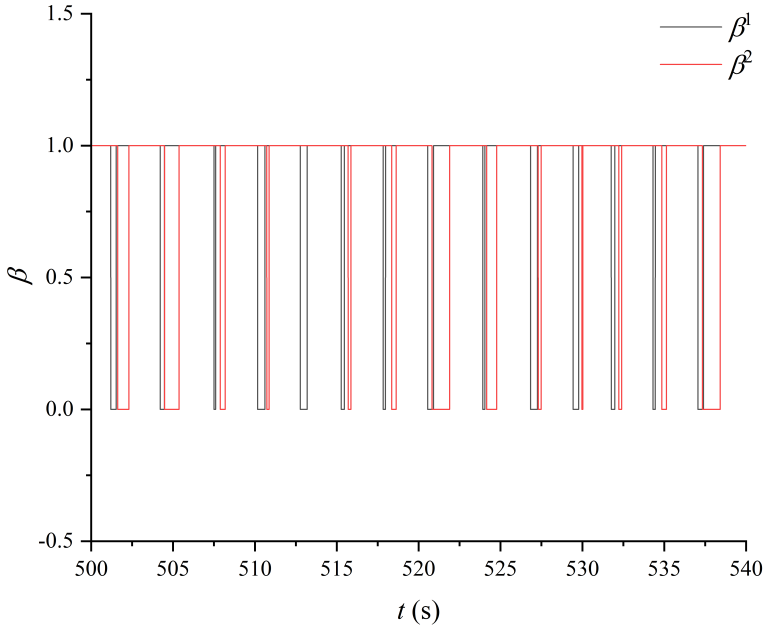

Figure 5.30: The control command of three-body optimal control under $\bar{J}_4$.

performance is observed.

The phase relationship between the PTO force and the relative rotational velocity under declutching control is depicted in Fig. 5.32. In this figure, the shaded area denotes the power generated by the PTO. The duration in which the PTO force is

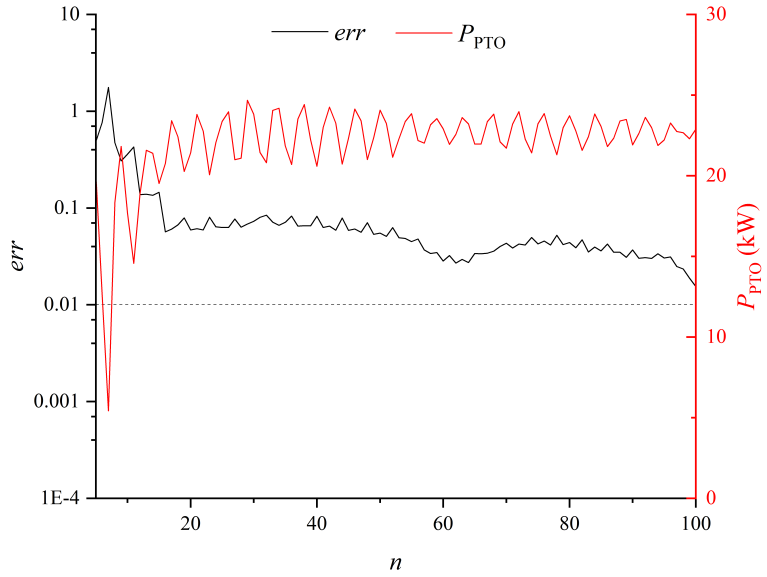

Figure 5.31: The variation of err and P_{PTO} with iteration.

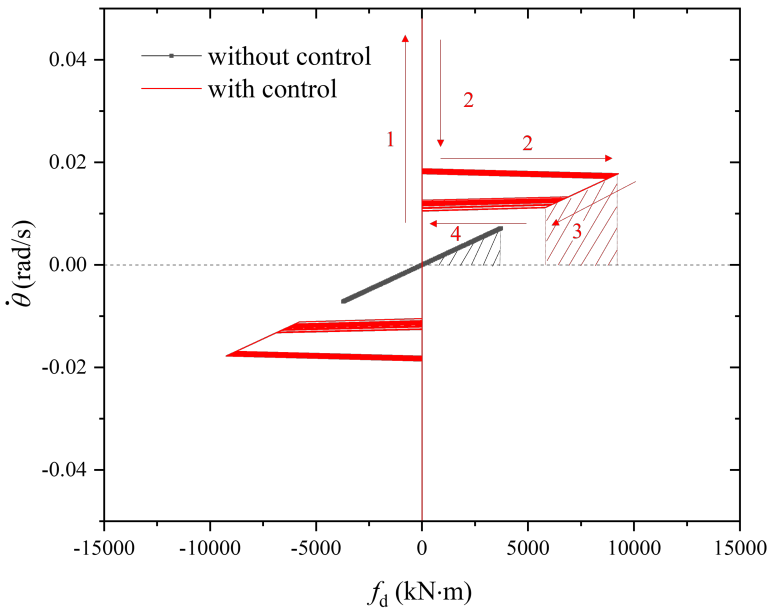

Figure 5.32: Phase relationship of the $\Delta\dot{\theta}$ and f_{d} for the three-body system.

active and does work is not increased; however, its amplitude is significantly higher, leading to a higher total power output. This observation demonstrates the effective expandability of the three-body system. It indicates that some conclusions drawn from the study of two-hinged box systems remain applicable and valid in this more complex configuration.

5.9 Summary

This chapter takes a hinged-box system as a case study of floating multi-body system control to investigate whether the proposed control method can achieve the objectives, and evaluate the effectiveness of control method. Each objective function demonstrates a better control effect on its respective performance indices compared to the others. The number of iterations is determined by setting a critical error threshold to determine if the computation has converged.

However, the solution of optimising $\bar{J}_4$ does not have good convergence as this objective function has multiple time-variant variables that are related to control. When the trajectories vary significantly, PMP makes it possible to experience lengthy iterations and fail to converge to an optimum. The proposed control method's effect is sensitive to the form of objective functions. It is necessary to try some alternative global optimisation methods, which will be discussed in chapter 7.

Chapter 6

Motion Control of Multiple Floating Bodies

6.1 Introduction

The energy transition within the floating multi-body system can also be utilised to mitigate the motion of individual bodies in the system. The mechanical energy (kinetic and potential) of the floating platform can be transferred to the attached structure or absorbed by the PTO system with a proper control strategy. The stabilisation of the platform is crucial to the enhancement and fluctuation reduction of the wind turbine's power output.

6.2 Case study 1: SS-ring system

6.2.1 Modelling of SS-ring system

The computational model is the OC4 semi-submersible (SS) platform neglecting the pontoons and cross braces between columns for simplicity. Since the main objective is to reduce the wave-induced motion, the wind turbines mounted on the floating platforms are neglected. However, the mass distribution remains consistent with the design that includes the wind turbine.

Table 6.1: Dimensions of the semi-submersible platform and ring [4]

Parameters	Dimensions
Depth to platform base below SWL (total draft)	20 m
Elevation of main column (tower base) above SWL	10 m
Elevation of offset column above SWL	12 m
Spacing between offset columns	50 m
Length of upper columns	26 m
Length of base columns	6 m
Depth to top of base columns below SWL	14 m
Diameter of main column	6.5 m
Diameter of offset (upper) columns	12 m
Diameter of base columns	24 m
Ring outer diameter	20 m
Ring inner diameter	10 m
Ring draft	4 m

The heave ring works by providing additional hydrodynamic damping to reduce the heave motion of the structure. Traditional heave plates are typically fixed beneath the columns or pontoons of the platform by a truss structure [83, 84]. In this case, the heave ring is located at the water surface and surrounds the central column. It is designed to be movable along the z-axis relative to the semi-submersible platform and is connected to the platform with a slide connection. There is a PTO device at the connection point, containing a spring and a damper in the heave direction. A similar concept was applied in a hybrid Spar-Torus Combination [1].

The global and body-fixed coordinate systems are illustrated in Fig. 6.1. The origins of the body-fixed coordinate systems are located at the centre of gravity of each body, respectively. The primary DoF for the semi-submersible platform's motion is in z direction. The water depth is set to 200 m in this case.

The parameters of the OC4 semi-submersible platform and the heave ring are presented in Tbl. 6.1. SWL is the abbreviation of Still Water Line. Different from the tuned heave plates, the damping coefficient of the damper is not predefined as a constant. Instead, it varies between 0 and B_{PTO} with the current declutching control method.

Within the SS-ring system, the relative motion in z direction remains unrestricted.

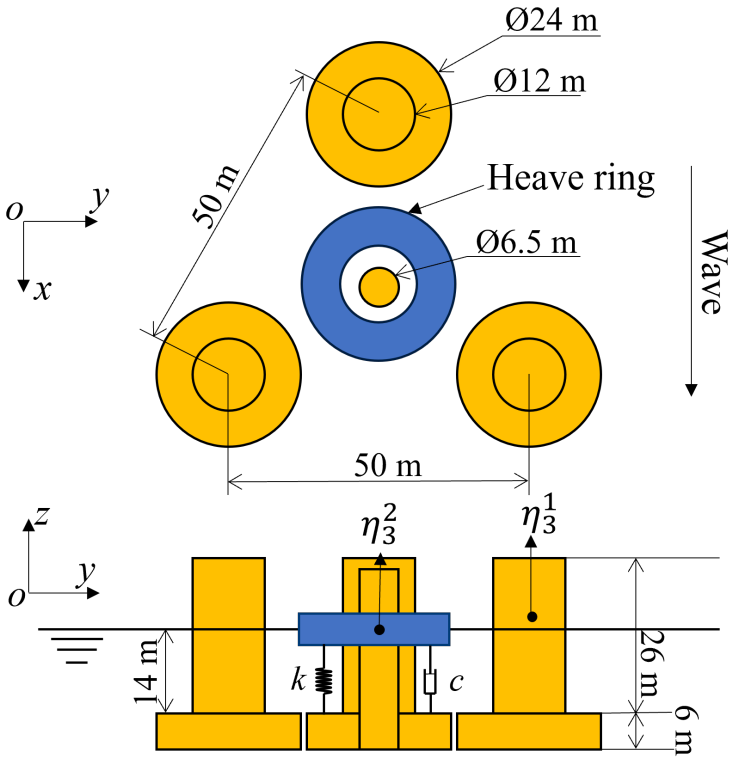

Figure 6.1: Front view (left) and side view (right) of the semi-submersible platform and the heave ring.

$f_{\mathrm{PTO}} = B_{\mathrm{PTO}}\Delta\dot{z}(t)$, where $\Delta\dot{z}(t)$ is the relative translational velocity in z direction between the two bodies herein. Because of the constraints from the slide connection, relative motions in the other directions of the two bodies are the same, except for the heave direction. The relative translation between the two connected bodies can be calculated from the difference between their respective heave motions in the body-fixed coordinate system. Therefore, the constraint equations are,

$$\begin{cases} \eta_1^1 = \eta_1^2 \\ \eta_2^1 = \eta_2^2 \\ \eta_3^1 = \eta_3^2 + \Delta z \\ \eta_4^1 = \eta_4^2 \\ \eta_5^1 = \eta_5^2 \\ \eta_6^1 = \eta_6^2 \end{cases} \tag{6.1}$$

$$\begin{aligned} \boldsymbol{\eta}^2 = \begin{bmatrix} \eta_1^2 \\ \eta_2^2 \\ \eta_3^2 \\ \eta_4^2 \\ \eta_5^2 \\ \eta_6^2 \end{bmatrix} &= \begin{bmatrix} 1 & 0 & 0 & 0 & 0 & 0 \\ 0 & 1 & 0 & 0 & 0 & 0 \\ 0 & 0 & 1 & 0 & 0 & 0 \\ 0 & 0 & 0 & 1 & 0 & 0 \\ 0 & 0 & 0 & 0 & 1 & 0 \\ 0 & 0 & 0 & 0 & 0 & 1 \end{bmatrix} \begin{bmatrix} \eta_1^1 \\ \eta_2^1 \\ \eta_3^1 \\ \eta_4^1 \\ \eta_5^1 \\ \eta_6^1 \end{bmatrix} + \begin{bmatrix} 0 \\ 0 \\ -1 \\ 0 \\ 0 \\ 0 \end{bmatrix} [\Delta z] \\ &= \boldsymbol{S}_{21}\boldsymbol{\eta}^1 + \boldsymbol{S}_{22}\boldsymbol{\Delta z} \end{aligned} \tag{6.2}$$

where the motions of plate $\boldsymbol{\eta}^2$ can be represented by the motions of semi-submersible platform $\boldsymbol{\eta}^1$ and the relative translation Δz. The matrix notation can be expressed as,

$$\boldsymbol{\eta} = \begin{bmatrix} \eta^1 \\ \eta^2 \end{bmatrix} = \begin{bmatrix} \boldsymbol{I} & \boldsymbol{0} \\ \boldsymbol{S}_{21} & \boldsymbol{S}_{22} \end{bmatrix} \begin{bmatrix} \boldsymbol{\eta}^1 \\ \boldsymbol{\Delta z} \end{bmatrix} = \boldsymbol{S}\boldsymbol{\eta}' \tag{6.3}$$

where I is the identity matrix; $\boldsymbol{\eta}'$ is the motion with constraint. Substituting Eq. 6.3 to Eq. 3.20, the motions with slide connection can be solved.

The heave motion of the platform is sensitive to the wave frequency and the damping coefficient of PTO. Figure 6.2 presents the average heave speed of the semi-submersible platform under different PTO damping coefficients and wave frequencies. No control is applied to the system in this subsection. Since the SS-ring system has small damping across most wave frequency ranges, the heave results only have an obvious increase near the resonance frequency of 0.62 rad/s. Besides, the heave speed amplifies with

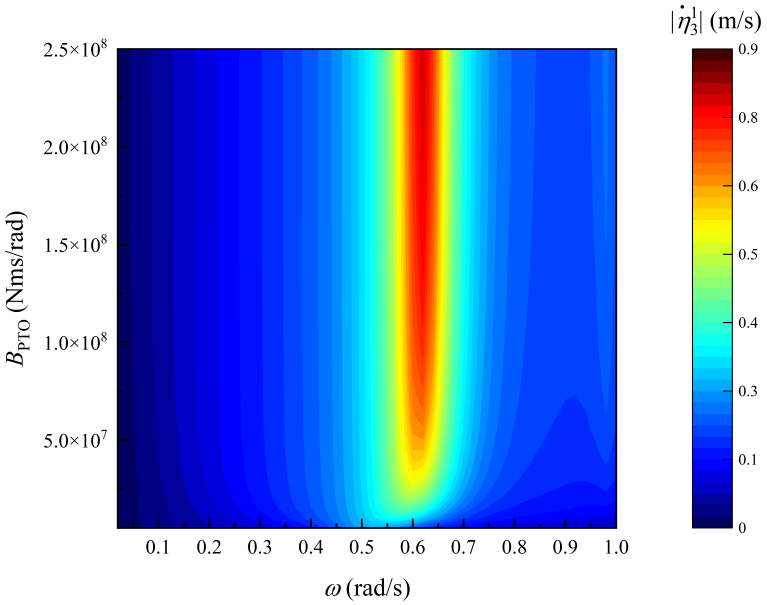

Figure 6.2: Average heave speed of semi-submersible platform under different PTO damping coefficients and wave frequencies (no control applied).

B_{PTO}. As B_{PTO} reaches infinity, the platform and ring can be considered as being welded together. In this situation, the heave speed converges to a constant value.

Another performance index, the time-averaged power absorption of the PTO, is defined as follows,

$$P_{\mathrm{PTO}} = \frac{1}{T}\int_0^T B_{\mathrm{PTO}}(t)\Delta\dot{z}(t)^2 dt \tag{6.4}$$

Figure 6.3 shows the average power absorption of the PTO system under different PTO damping coefficients and wave frequencies. The PTO power absorption peaks at a B_{PTO} of 2×10^7 N $\cdot$ s/m. This value of B_{PTO} can be regarded as the best configuration of a PTO system for power generation without control, however, in this thesis, the P_{PTO} is not the focus of optimisation. In the next subsection, when applying the optimal declutching control method, B_{PTO} will be replaced by B_{d}, which varies over time.

6.2.2 Control results in regular waves

The objective function to be minimised is the time-averaged heave speed of the semi-submersible platform,

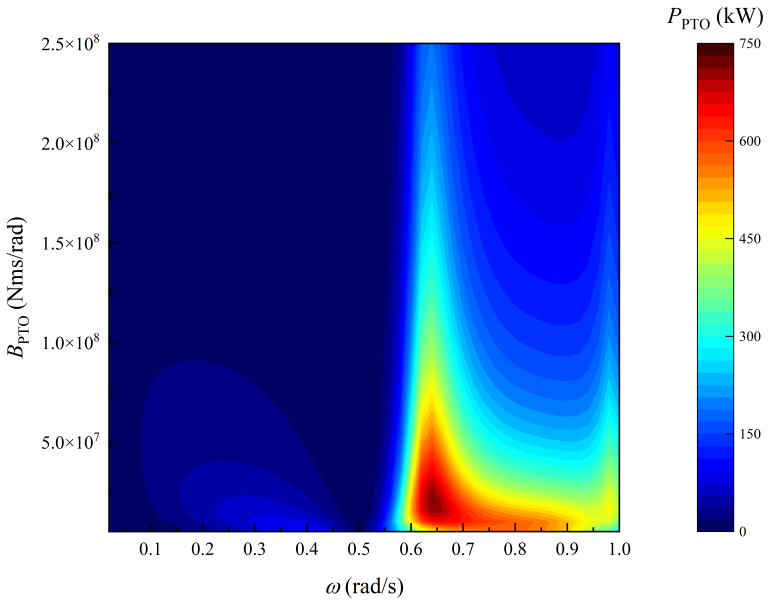

Figure 6.3: Average power absorption of PTO under different PTO damping coefficients and wave frequencies (no control applied).

$$\min\left(\bar{J}\right) = \min\left(v_{\mathrm{heave}}\right) = \min\left(\frac{1}{T}\int_0^T \left|\dot{\eta}_3^1\right| dt\right) \tag{6.5}$$

With this objective function, the optimal control command can be calculated in MATLAB with the optimal declutching control method. The initial damping coefficient is set to the value of 5×10^6 Nm·s/rad. The restoring coefficient is set to 0 N/m. The controlled heave motion is calculated in wave frequencies range from 0.02 –1 rad/s.

Figures 6.4 and 6.5 compare the controlled results with results under different damping coefficients. In Fig. 6.4, v_{heave} in part of wave frequencies higher than 0.5 rad/s are slightly minimised. The reason is that the declutching control can effectively reduce the average value of B_{PTO}. The peak of the heave response curve moves left. Therefore, the higher frequencies can be optimised. The tendency of P_{PTO} is the same. The peak of the result with a constant B_{PTO} is not accurately presented because of the insufficiently fine interval of wave frequency. The condition when B_{PTO} is 5×10^8 Nm·s/rad is regarded as welded.

In Fig. 6.4, the controlled result is not as low as the result without damping between 0.4 –0.46 rad/s, which means the results are sub-optimal. This is because the PMP can

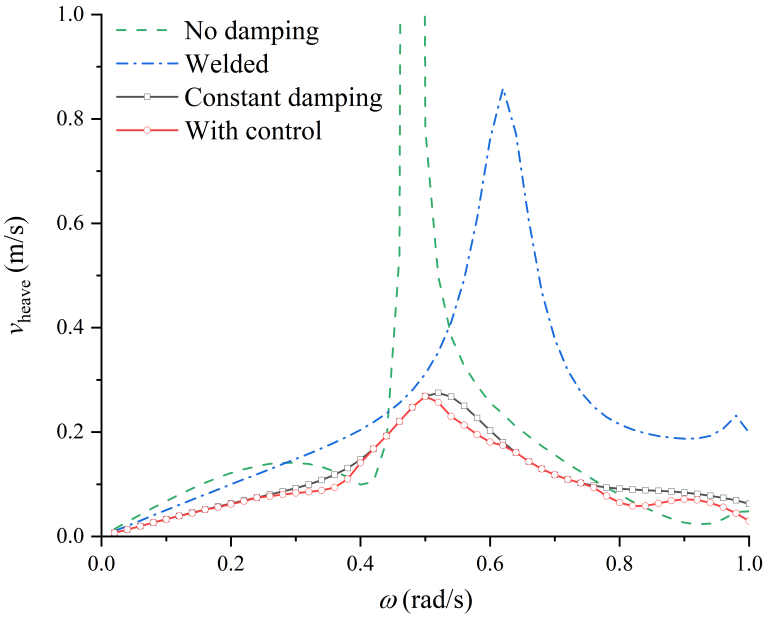

Figure 6.4: The v_{heave} of the semi-submersible platform in different wave frequencies (Green dash line: No damping; Blue dash-dot line: Welded; Black solid line with square symbol: Constant damping; Red solid line with round symbol: With control) when B_{PTO} is 5×10^6 Nm·s/rad. Some irrelevant resonant peaks are not shown in the figure.

only find local optima. The results with control are highly sensitive to the time step, initial state, and final state. This difference is also discussed in the next chapter.

The controlled results when B_{PTO} is 1×10^8 Nm·s/rad in Fig. 6.5 have different conclusions. Comparing the results in Fig. 6.4 and 6.5, the heave motion depends on the selection of the damping coefficient. A low damping coefficient (5×10^6 Nm·s/rad) leads to a decrease in heave motion in wave frequencies between 0.5 and 0.64 rad/s, which is higher than the natural frequency with constant damping. In contrast, a high damping coefficient (1×10^8 Nm·s/rad) allows for the simultaneous reduction of heave motion and increase in PTO power in wave frequencies between 0.5 and 0.64 rad/s, which is lower than the natural frequency with constant damping.

The time domain results of the platform's heave speed are shown in Fig. 6.6 and 6.7. The control command β is also compared. The controlled heave velocity is on average lower than the velocity without control. The control command β is a discrete function of 0 and 1, representing whether the damping force is loaded to the platform.

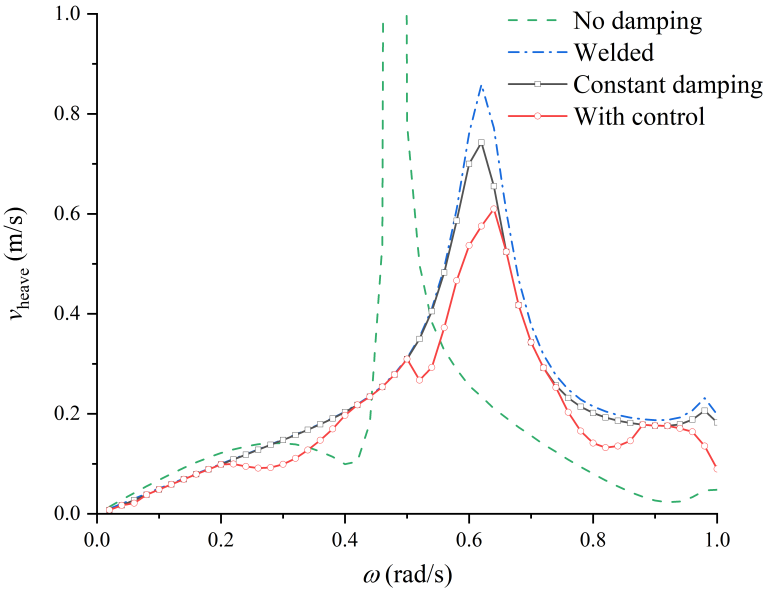

Figure 6.5: The v_{heave} of the semi-submersible platform in different wave frequencies (Green dash line: No damping; Blue dash-dot line: Welded; Black solid line with square symbol: Constant damping; Red solid line with round symbol: With control) when B_{PTO} is 1×10^8 Nm·s/rad. Some irrelevant resonant peaks are not shown in the figure.

The heave ring has a relatively large size, which provides large hydrodynamic damping to the system. The declutching control significantly reduces the platform's average damping. In an almost undamped system, the controlled motion in the time domain tends to be periodic, but not sinusoidal. In Fig. 6.6 and 6.7, the results under control are approximate to the response without damping. The profile of the controlled curve changes to a "beat vibration" pattern, a phenomenon typically observed in forced, undamped oscillations. It is important to note that the system parameters of the semi-submersible platform stay unchanged. Consequently, the observed variation in frequency is attributable to the resultant force of the wave force and the PTO's damping force. As the average $\dot{\eta}_3^1(t)$ of the platform decreases, there is a corresponding reduction in the control time, and conversely, an increase in $\dot{\eta}_3^1(t)$ results in a longer control duration.

While the control implementation results in a reduction of the average $\dot{\eta}_3^1(t)$, it also leads to an increase in the fluctuation of the heave motion. This phenomenon can

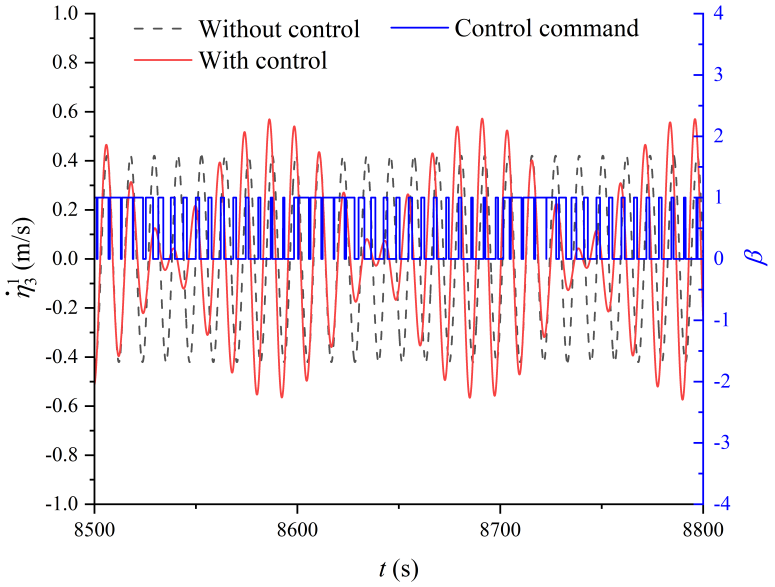

(a) The control effect on heave velocity.

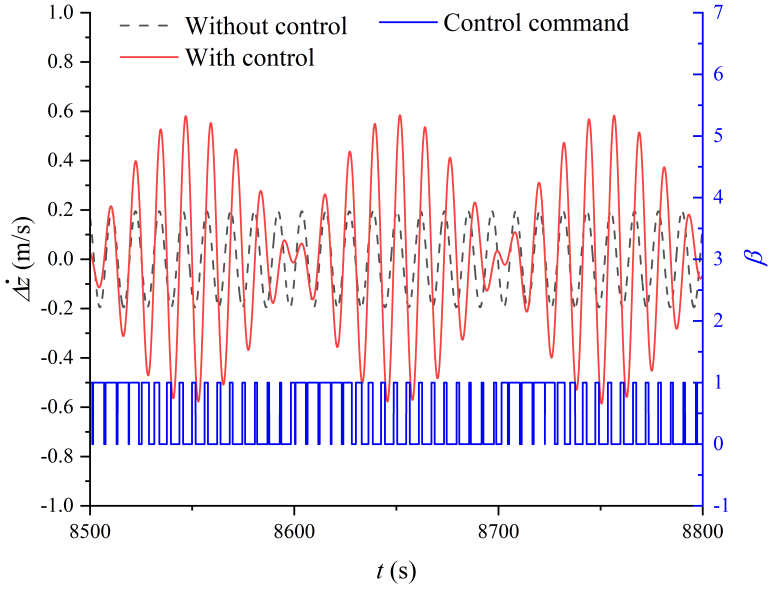

(b) The control effect on relative heave velocity.

Figure 6.6: Time domain results for $\dot{\eta}_3^1(t)$, $\Delta\dot{z}$, and the corresponding control command β when B_{PTO} is 5×10^6 Nm·s/rad.

be attributed to that our objective function is defined to minimise the average heave speed. This issue is related to fatigue and dynamic loading concerns, and requires further attention in future research.

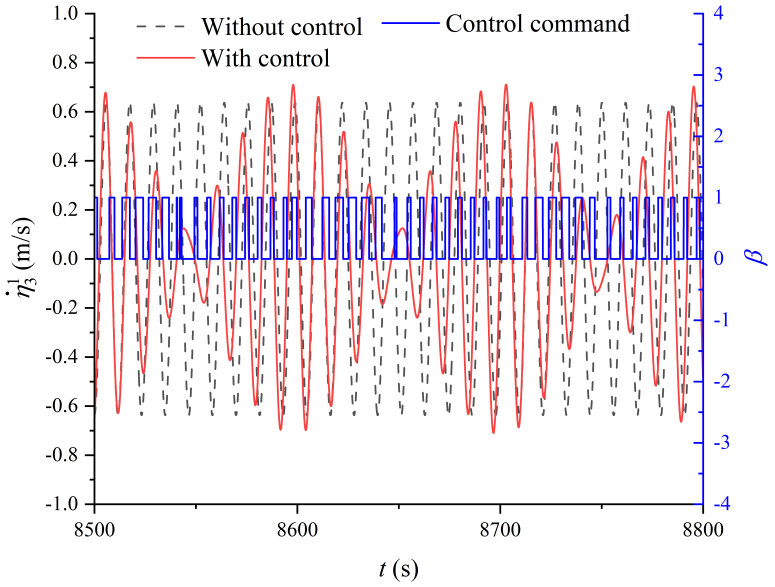

(a) The control effect on heave velocity.

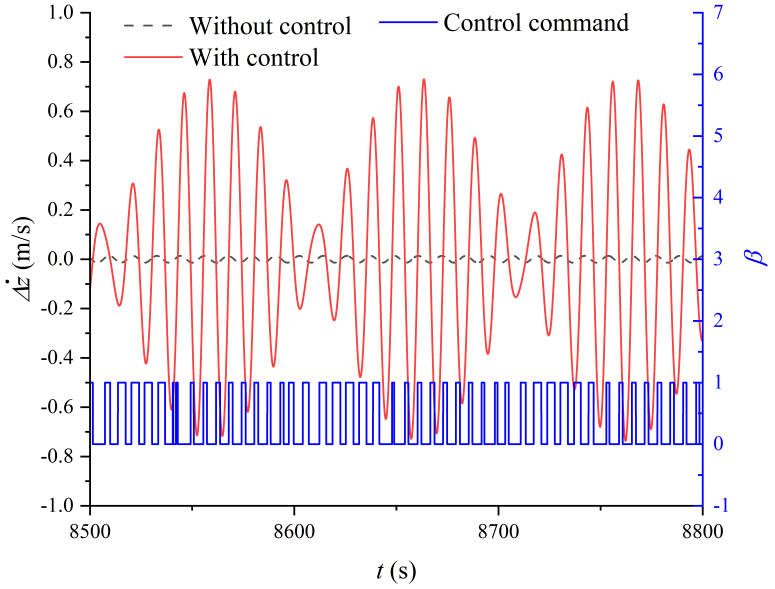

(b) The control effect on relative heave velocity.

Figure 6.7: Time domain results for $\dot{\eta}_3^1(t)$, $\Delta\dot{z}$, and the corresponding control command β when B_{PTO} is 1×10^8 Nm·s/rad.

6.2.3 Analysis in irregular waves

In the controlled environment of regular waves, achieving an optimal control result is more straightforward. The predictability and uniformity of regular waves allow for

Table 6.2: Typical irregular wave conditions [5].

	$H_s(m)$	$T_p(s)$	γ
Load 1	1.22	6	3.3
Load 2	1.98	7.5	3.3
Load 3	3.05	8.9	3.3

a control strategy that can be finely tuned to the wave's frequency. This periodic behaviour in regular waves is helpful to the calculation of an optimal average B_{PTO} and leads to efficient control. However, the irregular waves introduce complexity due to the stochastic nature of the ocean, with many different frequencies and amplitudes present simultaneously. The control system must adapt to a wide range of conditions, and a periodic control command may no longer be adequate.

The real-world applicability of the model is proven when it is tested against these irregular wave conditions. The average significant wave height, H_s, spectral peak periods, T_p, and peakedness parameter, γ, of three sea states generated using the Jonswap spectrum are listed in Tbl. 6.2.

The relationship of forces exerted on a semi-submersible platform is depicted in Fig. 6.8. It indicates that the wave forces experienced by the platform are partly, but not perfectly counteracted by the PTO damping forces. When the two forces are in phase, the net force will lead to the opposite effect of motion mitigation. However, there is still a notable reduction in the overall heave motions of the platform. Fig. 6.9 details the heave motion mitigation effect under three different load cases in irregular waves. The reduction effect across all cases suggests that the control strategy is indeed dampening the heave motion effectively. The results prove the control method's robustness and relevance for practical engineering applications. By proving effective in these scenarios, the model demonstrates its potential for real-world deployment.

6.3 Case study 2: spar-plate system

This optimal phase control can be specifically used to mitigate the motion of a spar-type FWT platform by adding an auxiliary hinged plate at its bottom base. The

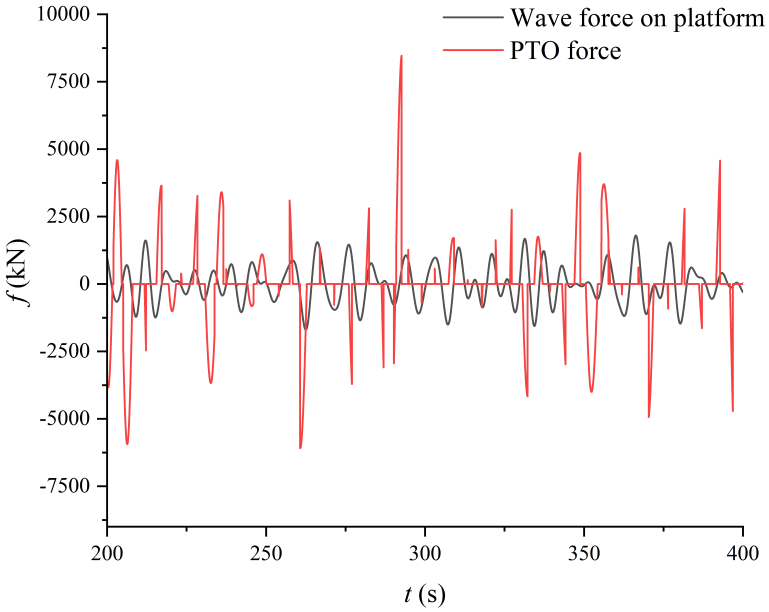

Figure 6.8: Forces on the semi-submersible platform in irregular waves of Load 1.

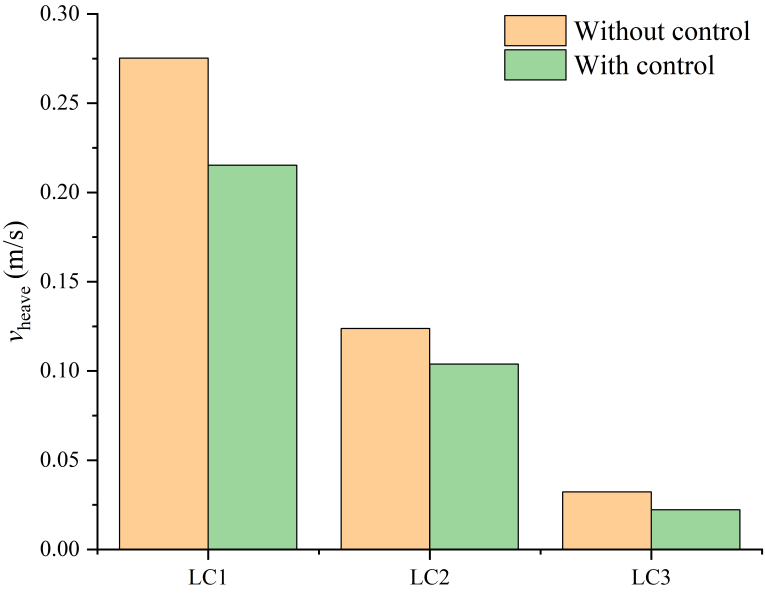

Figure 6.9: The control effect of v_{heave} in irregular waves.

predominant motion of spar-type FWT is in pitch and surge direction. A small-sized plate is designed to effectively increase the added mass and mitigate the motion of the spar-type FWT. This is achieved through converting mechanical energy into electric energy via a PTO system and proper control strategy.

Table 6.3: Dimensions of the spar-type platform and plate [6].

Parameters	Dimensions
Depth to platform base below SWL (total draft)	120 m
Elevation to platform top (tower base) above SWL	10 m
Depth to top of taper below SWL	4 m
Depth to bottom of taper below SWL	12 m
Platform diameter above taper	6.5 m
Platform diameter below taper	9.4 m
Platform mass, including ballast	8,029,202 kg
CM location below SWL along platform centreline	89.9155 m
Platform pitch inertia about CM	4,229,230,000 $\text{kg} \cdot \text{m}^2$
Plate length	9.4 m
Plate width	18.8 m

6.3.1 Modelling of hinged spar-plate system

The computational model includes two rigid bodies: an OC3-Hywind spar-type floating platform and a rectangular plate with a notch. The plate is hinged at the bottom of the spar. The front view, side view, and dimensions of the hinged system model are illustrated in Fig. 6.10. The parameters of the spar-type platform and plate are listed in Tbl. 6.3. In this case, despite the plate's relatively small size, it may provide a large hydrodynamic damping moment because of the long force arm. A PTO device is installed at the hinge point to absorb energy from the relative pitch motion between the platform and plate.

The body-fixed coordinate system origins are located at the CoG of each body, respectively. Wave propagates along the positive x-axis. For waves in this direction, the primary motion DoF of the spar-type platform is pitch and surge. It should be noted that a limitation of the current design is its dependency on wave direction; it is most effective when the wave angle is at 0 degrees.

In the hinged spar-plate system, the unrestricted direction is pitch. $f_{\text{PTO}} = -B_{\text{PTO}}\Delta\dot{\theta}(t)^2$, where $\Delta\dot{\theta}(t)$ is the relative angular velocity in the pitch direction between the two bodies herein.

Because of the constraints at the hinge point, the only permissible relative motion is the rotation along y-axis at the hinge point. Hinge constrains the motions at the hinge

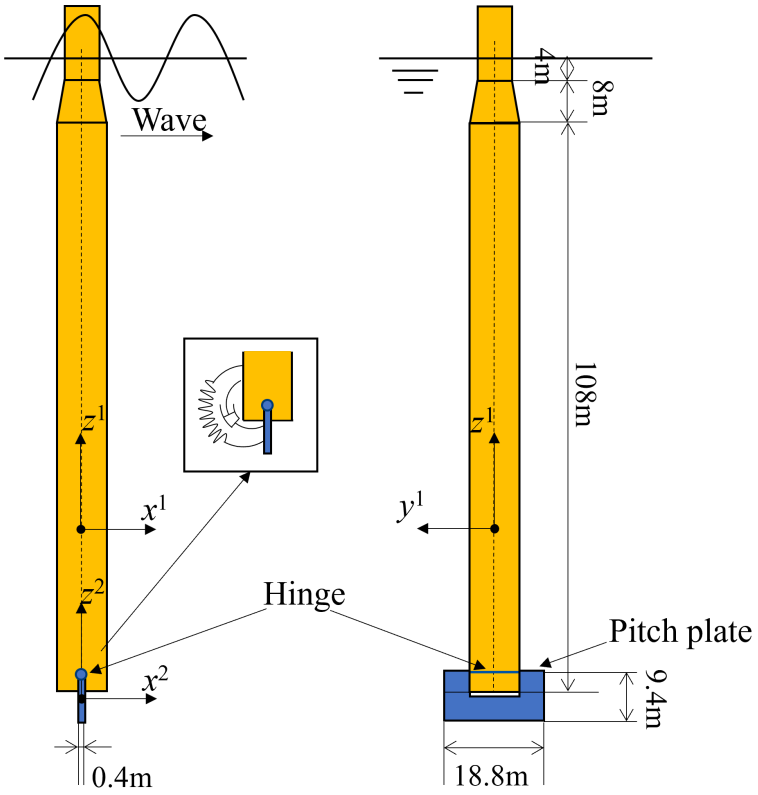

Figure 6.10: Front view (left) and side view (right) of the spar-plate system.

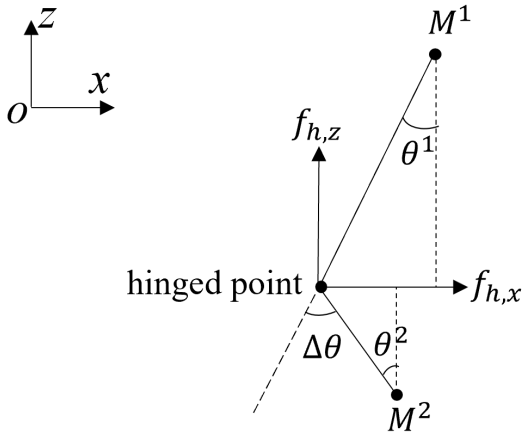

Figure 6.11: Relationship of pitch motion at the hinge point.

point of the two bodies to be the same, except for the pitch direction. As illustrated in Fig. 6.11, the relative rotational angle at the hinge point of the two hinged bodies can be calculated from the difference between their respective pitch angles in the body-fixed

coordinate system, therefore, the constraint equations are,

$$\begin{cases} \eta_1^1 - R\sin\eta_5^1 = \eta_1^2 + r\sin\eta_5^2 \\ \eta_2^1 + R\sin\eta_4^1 = \eta_2^2 - r\sin\eta_4^2 \\ \eta_3^1 = \eta_3^2 \\ \eta_4^1 = \eta_4^2 \\ \eta_5^1 = \eta_5^2 - \Delta\theta \\ \eta_6^1 = \eta_6^2 \end{cases} \tag{6.6}$$

where R is the distance from the CoG of the spar-type platform to the hinge point; r is the distance from the CoG of the plate to the hinge point. The pitch amplitude follows the small-angle approximation, thus $\sin\eta_5$ and $\sin\eta_4$ can be written as η_5 and η_4. The constraint equation set can be linearised to Eq. 6.7. It can be expressed in matrix notation as Eq. 6.8,

$$\begin{cases} \eta_1^1 - R\eta_5^1 = \eta_1^2 + r\eta_5^2 \\ \eta_2^1 + R\eta_4^1 = \eta_2^2 - r\eta_4^2 \\ \eta_3^1 = \eta_3^2 \\ \eta_4^1 = \eta_4^2 \\ \eta_5^1 = \eta_5^2 - \Delta\theta \\ \eta_6^1 = \eta_6^2 \end{cases} \tag{6.7}$$

$$\begin{aligned} \boldsymbol{\eta}^2 = \begin{bmatrix} \eta_1^2 \\ \eta_2^2 \\ \eta_3^2 \\ \eta_4^2 \\ \eta_5^2 \\ \eta_6^2 \end{bmatrix} &= \begin{bmatrix} 1 & 0 & 0 & 0 & -(R+r) & 0 \\ 0 & 1 & 0 & R+r & 0 & 0 \\ 0 & 0 & 1 & 0 & 0 & 0 \\ 0 & 0 & 0 & 1 & 0 & 0 \\ 0 & 0 & 0 & 0 & 1 & 0 \\ 0 & 0 & 0 & 0 & 0 & 1 \end{bmatrix} \begin{bmatrix} \eta_1^1 \\ \eta_2^1 \\ \eta_3^1 \\ \eta_4^1 \\ \eta_5^1 \\ \eta_6^1 \end{bmatrix} + \begin{bmatrix} -r \\ 0 \\ 0 \\ 0 \\ 1 \\ 0 \end{bmatrix} [\Delta\theta] \\ &= \boldsymbol{S}_{21}\boldsymbol{\eta}^1 + \boldsymbol{S}_{22}\boldsymbol{\Delta\theta} \end{aligned} \tag{6.8}$$

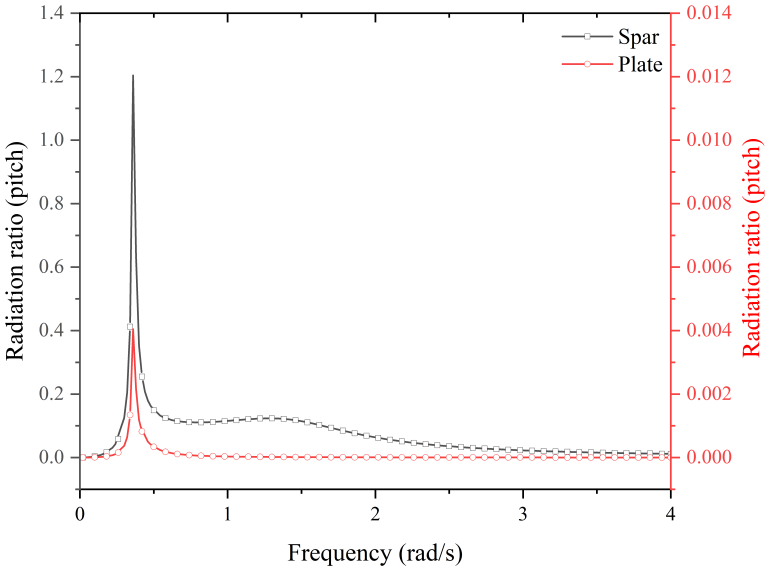

Figure 6.12: Radiation ratio of the spar-type platform and the plate under different wave frequencies.

where the motions of plate $\boldsymbol{\eta}^2$ can be represented by the motions of spar-type platform $\boldsymbol{\eta}^1$ and the relative angle $\Delta\theta$. The expression in matrix notation is,

$$\boldsymbol{\eta} = \begin{bmatrix} \eta^1 \\ \eta^2 \end{bmatrix} = \begin{bmatrix} \boldsymbol{I} & \boldsymbol{0} \\ \boldsymbol{S}_{21} & \boldsymbol{S}_{22} \end{bmatrix} \begin{bmatrix} \boldsymbol{\eta}^1 \\ \boldsymbol{\Delta\theta} \end{bmatrix} = \boldsymbol{S}\boldsymbol{\eta}' \tag{6.9}$$

Substituting Eq. 6.9 to the dynamic equation 3.20 in Chapter 3, the motions with hinge connection can be solved.

The radiation forces can be derived from the velocities. The ratio of radiation force to total excitation force in pitch direction is shown in Fig. 6.12. The radiation ratio of the spar platform is much larger than that of the hinged plate. Although the waterline section area of the hinged spar-plate system is small, the fluid memory effect is still not neglectable.

Figures 6.13 and 6.14 present the performance of the platform and PTO under different PTO damping coefficients and wave frequencies when without control. In Fig. 6.13, the platform's pitch speed, $\left|\dot{\eta}_5^1\right|$, has two distinct peaks corresponding to the change of damping coefficient B_{PTO}. The first peak, illustrated in the left sub-figure of Fig. 6.13, occurs when B_{PTO} is extremely large (2×10^8 Nm·s/rad), approaching

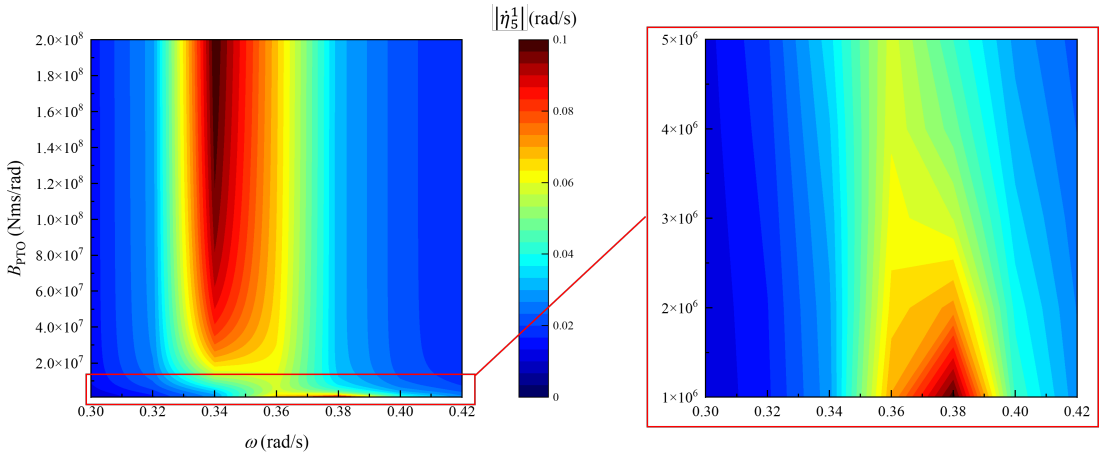

Figure 6.13: Left: Pitch speed of the spar-type platform under different PTO damping coefficients and wave frequencies; Right: zoom-in at low B_{PTO}.

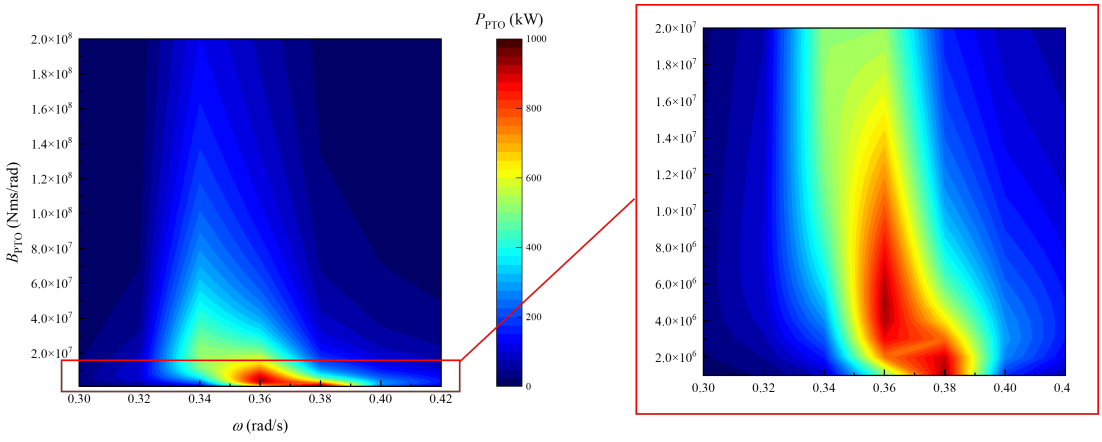

Figure 6.14: Left: Power absorption of PTO under different PTO damping coefficients and wave frequencies; Right: zoom-in at low B_{PTO}.

infinite. In this situation, the platform and plate behave as if they are rigidly connected or welded. As a consequence, the platform is subjected to an increased total wave force. Conversely, the second peak, illustrated in the right sub-figure of Fig. 6.13, occurs when B_{PTO} is markedly small (1×10^6 Nm·s/rad), approaching 0. In this situation, there is very limited damping force acting on the platform, allowing the platform and plate to move independently. Thus, when B_{PTO} is set to an appropriate value, the pitch motion of the platform can be minimised when without control, especially in regular waves.

The damping of this PTO device only exists in the pitch. The hydraulic PTO force is approximate to friction (Coulomb) damping form, as demonstrated in Eq. 6.10,

$$P = B_{\mathrm{PTO}} \Delta\dot{\theta}^2 \tag{6.10}$$

The average power absorption of the PTO system is determined by two factors: the damping coefficient, B_{PTO}, and the relative angular velocity at the hinge point, $\Delta\theta$. However, B_{PTO} also has influence on $\Delta\theta$. Figure 6.14 compares the power absorption under different damping coefficients and regular wave frequencies. From this figure, we can find that one peak of the power absorption at $B_{\mathrm{PTO}} = 5.5 \times 10^6$ Nm·s/rad. It is important to note that the vertical axis starts from 1×10^5 Nm·s/rad. Therefore, this scale may not precisely capture the position of the other peak. The damping coefficient of 5.5×10^6 Nm·s/rad corresponds to the position for minimal platform pitch motion in Fig. 6.13. This implies the plate not only mitigates the platform's motion but also concurrently generates energy herein, a phenomenon observed even when without any control. However, to guarantee the effectiveness of the design across varying wave conditions, the implementation of a control mechanism is necessary.

6.3.2 Control results in regular waves

The characteristics of the controlled motion amplitude and power absorption of the spar-plate system are investigated in regular waves. The results under optimal declutching control are discussed in this subsection. In this section, B_{PTO} is chosen as a moderate value of 3×10^7 Nm·s/rad for a more obvious control effect.

The objective function in optimal control is v_{pitch}, the time-averaged pitch speed of the spar-type platform, which is defined as,

$$\min\left(\bar{J}\right) = \min\left(v_{\mathrm{pitch}}\right) = \min\left(\frac{1}{T}\int_0^T \left|\dot{\eta}_5^1\right| dt\right) \tag{6.11}$$

Figure 6.15a demonstrates that the spar-type platform's motion curve can be effectively influenced by the hinged plate or B_{PTO} even though the plate size and mass are both very small. Among the four curves representing different PTO damping scenarios, the controlled v_{pitch} exhibits the lowest value. The performance index v_{pitch} peaks when the wave frequency reaches one of the system's natural frequencies, 0.34 rad/s.

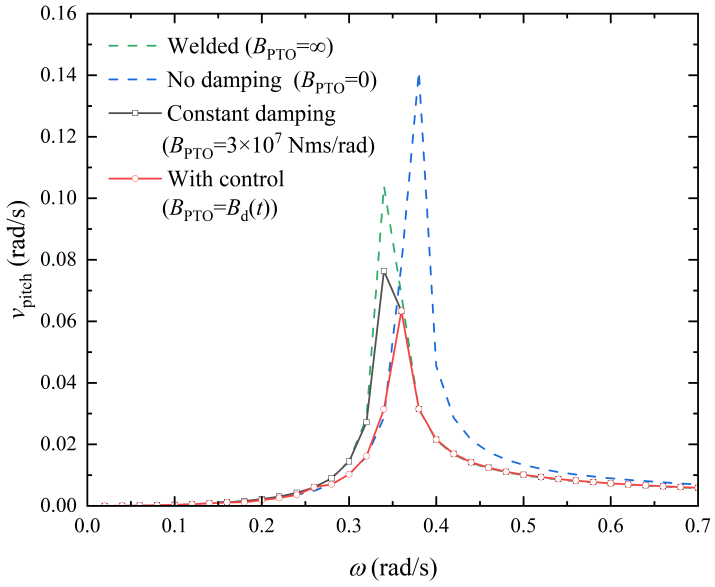

(a) Average pitch speed of the spar-type platform.

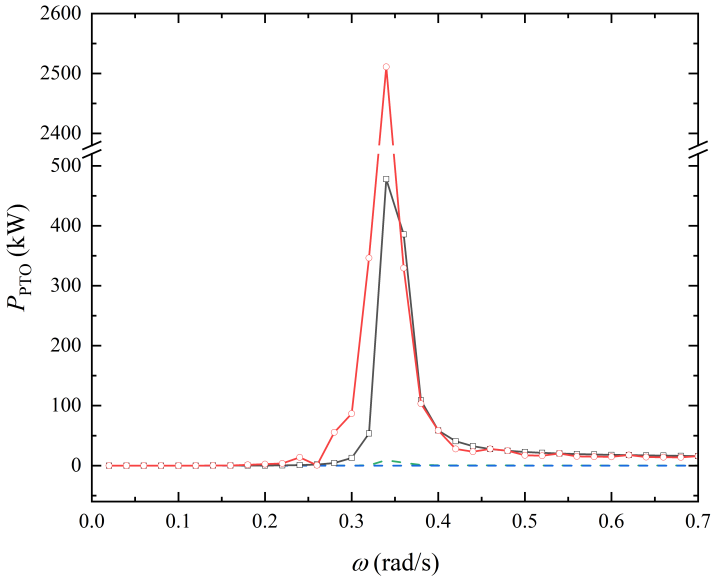

(b) Average power absorption of PTO.

Figure 6.15: Performance indices in different wave frequencies (Green dash line: No damping; Blue dash-dot line: Welded; Black solid line with square symbol: Constant damping; Red solid line with round symbol: With control) when B_{PTO} is 3×10^7 Nm·s/rad.

When resonance happens, the platform experiences maximum pitch motion, and the maximum percentage of wave energy is transferred to mechanical energy. Accordingly,

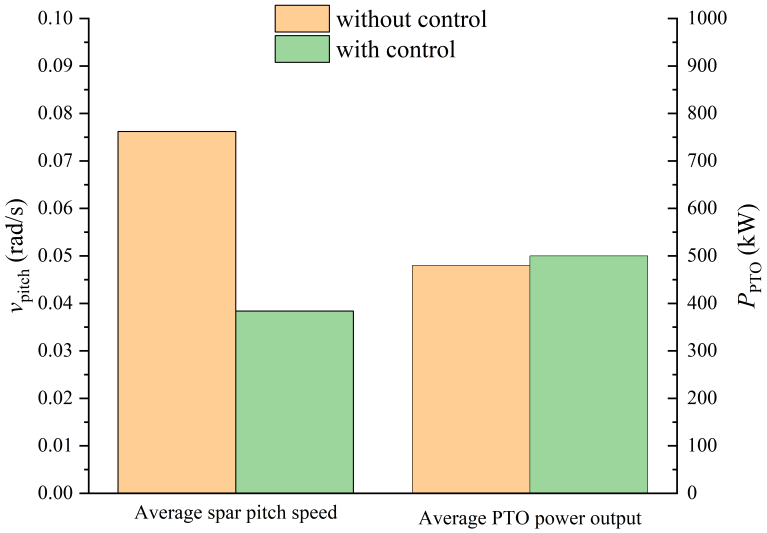

Figure 6.16: Performance indices when declutching control are applied to the spar-plate system.

the peak of P_{PTO} is also at 0.34 rad/s. The P_{PTO} is obviously enhanced in relatively lower frequencies. The magnitudes of these peaks are much larger than those of other frequencies, which are beyond the realistic range, and therefore they can be omitted from the analysis. However, the control effect is most obvious at 0.34 rad/s and the control mechanism is worthy of analysis herein.

Figure 6.16 presents the v_{pitch} and P_{PTO} at a wave frequency of 0.34 rad/s. It reveals that v_{pitch} is optimised to the minimum from 0.0762 rad/s to 0.0265 rad/s using optimal declutching control. The performance of declutching control effectively realises the motion control for this system. Simultaneously, another performance index investigated herein, P_{PTO}, is increased from 480 kW to 500 kW.

The mechanical energy of the spar-type platform originates from wave energy. As seen in Fig. 6.16, under optimal declutching control, 500 kW of the wave energy is converted into electric energy by PTO, 4.2% higher than results without control. The hinged spar-plate system can be regarded as a more effective WEC under the current control method.

The time history result of declutching control is shown in Fig. 6.17. Since the average damping of the system is reduced with declutching control, the motion response

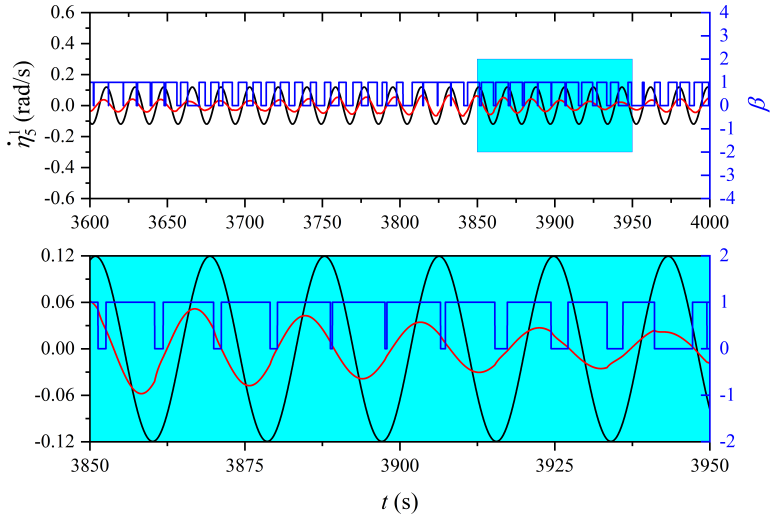

Figure 6.17: Time history of the spar-type platform pitch speed without and with declutching control (ω=0.34 rad/s, $B_{\mathrm{PTO}} = 3 \times 10^7$ Nm·s/rad).

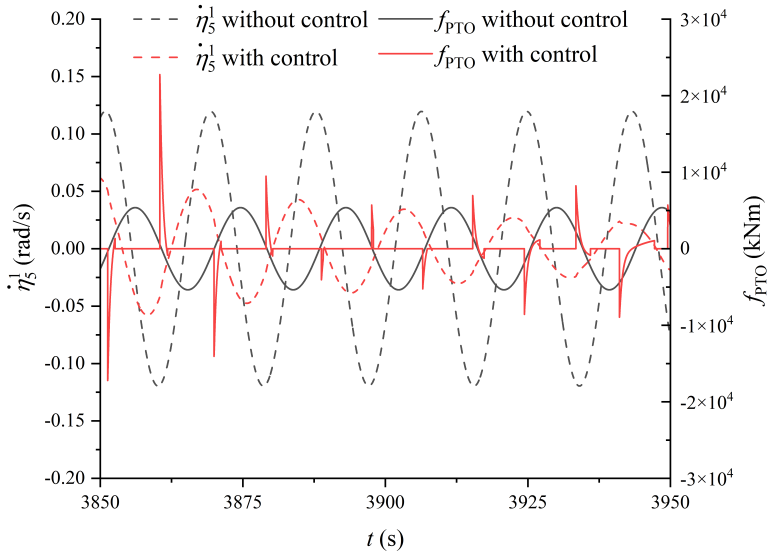

Figure 6.18: Phase relationship of spar-type platform's pitch velocity and PTO force.

needs a longer time to converge. Therefore, a time horizon from 3600 to 4000 seconds is selected within the entire simulation duration to ensure the convergence of response. The response under optimal declutching control is also periodic after convergence. The horizon from 3850 to 3950 seconds is zoomed in to show the responses and control commands clearly.

Fig. 6.18 reveals that the motion mitigation is related to the tuning of the phase

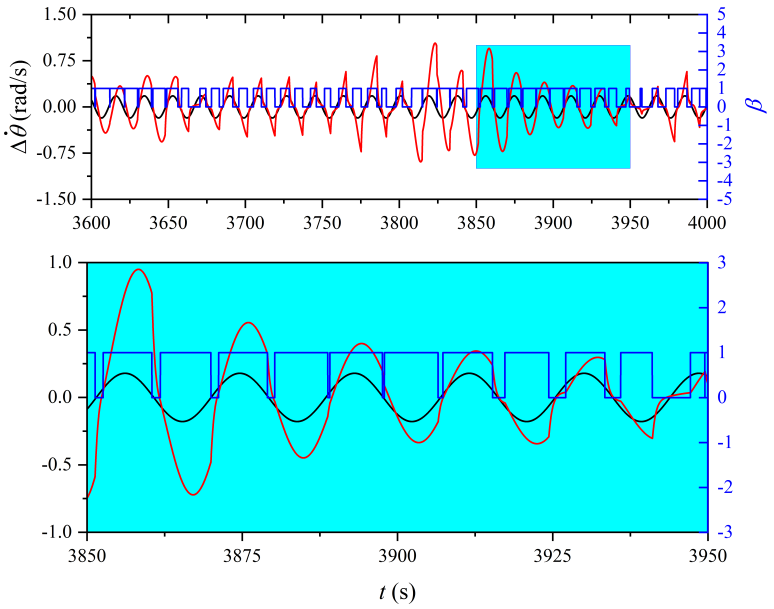

Figure 6.19: Time history of the relative angular velocity without and with declutching control (ω=0.36 rad/s, $B_{\mathrm{PTO}} = 3 \times 10^7$ Nm·s/rad, black line: without control, red line: with control, blue line: control command). When the control command is activated, $\Delta\dot{\theta}$ will have a surge of amplitude.

of the PTO damping force. Specifically, the controlled PTO force is anti-phase relative to the pitch velocity of the spar platform, continuously providing resistance to the platform's pitch motion. This aligns with the explanations on the control of $\bar{J}_1$ in Chapter 5. Although the plate is much smaller compared to the spar platform, it can exert a sufficient control force to mitigate the pitch motion.

The zoom-in figure in Fig. 6.19 shows the relationship of $\Delta\dot{\theta}$ and the control command clearly. In Fig. 6.19, when command control is 1 (activated), the PTO is switched off and the damping force is 0 constantly. The relative angular velocity surges in a short time without the constraint of damping. The mechanical energy of the plate accumulates until its velocity is large enough. Then the PTO is switched on again when command control turns to 0 (unactivated). The damping force is loaded again, and the PTO starts to extract mechanical energy.

A noticeable reduction in surge motions is also observed. In contrast to a sliding hinge mechanism in the SS-ring system that primarily releases heave motion, the hinged pitch plate shows the capability to attenuate motion in multiple directions. For floating

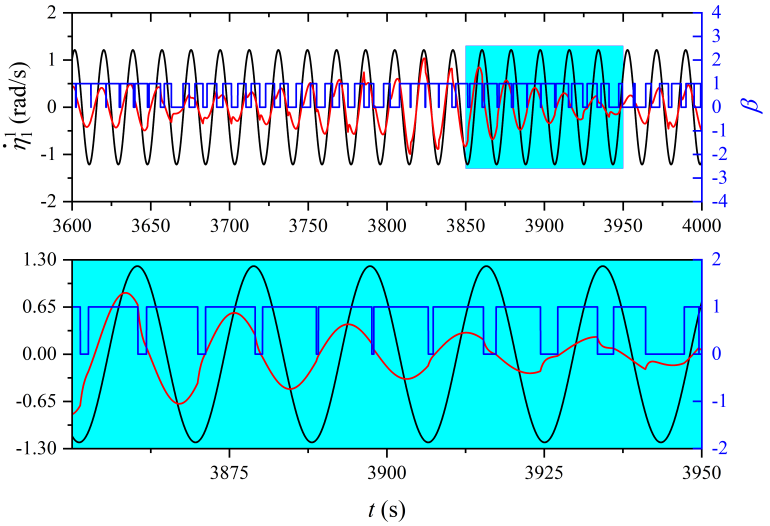

Figure 6.20: Time history of the spar-type platform surge speed without and with declutching control (ω=0.34 rad/s, $B_{\mathrm{PTO}} = 3 \times 10^7$ Nm·s/rad, black line: without control, red line: with control, blue line: control command).

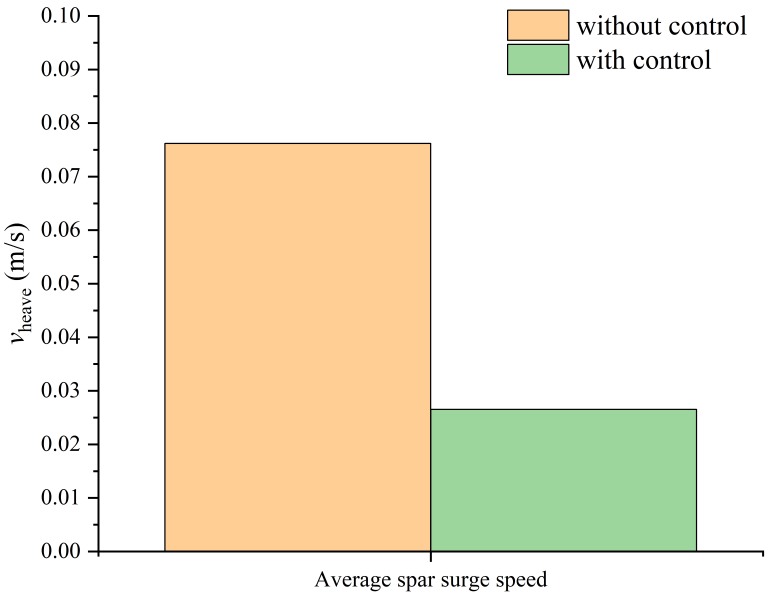

Figure 6.21: Average spar-type platform surge speed when declutching control is applied to the spar-plate system.

wind turbines, achieving stabilisation in the surge direction is crucial for mitigating the fluctuations of relative wind speed of the rotor encounters. This is important for reducing the FWT's power output fluctuations. Consequently, this leads to an

enhancement in the overall performance of spar-type FWTs.

6.3.3 Analysis in irregular waves

The results in irregular are shown in Fig. 6.22 and Fig. 6.23, providing a validation of the performance of the spar-plate systems under optimal declutching control. It is generally anticipated that motion mitigation would be more challenging in irregular waves due to their varying wave periods. This unpredictability can lead to less effective control when compared to the more uniform and predictable regular waves.

In Fig. 6.22 and Fig. 6.23, despite less effective motion mitigation in irregular waves, there is a concurrent increase in power output as a "by-product" , from 4.7 kW to 6.5 kW. This implies that the system is able to capture more energy from the irregular waves. Optimal declutching control appears to effectively balance these two aspects: mitigating motion to a reasonable extent while also enhancing power output. This phenomenon can be called "killing two birds with one stone" , which indicates the control succeeds in converting a greater amount of the mechanical energy of platform to the electrical energy. These results validate the adaptability of the control system to variable sea conditions, making it a promising solution for real-world applications. It should be noted that the current design of the plate and PTO system is primarily intended for the study of control mechanisms and has not been fully optimised. A more appropriate design of the plate mass and PTO damping coefficient could potentially enhance the control effects significantly, improving both motion mitigation and power output. These will be discussed in the subsequent section.

6.3.4 Parametric analysis

The previous cases have proved that optimal declutching control can effectively realise the motion control of floating multi-body systems. However, it still needs further discussion of parameters influencing the optimal declutching control's effectiveness. The performance of the auxiliary plate is influenced by the PTO damping, spring stiffness and plate mass. The initial rotational PTO damping B_{PTO} is set as 5.5×10^{6} Nm·s/rad.

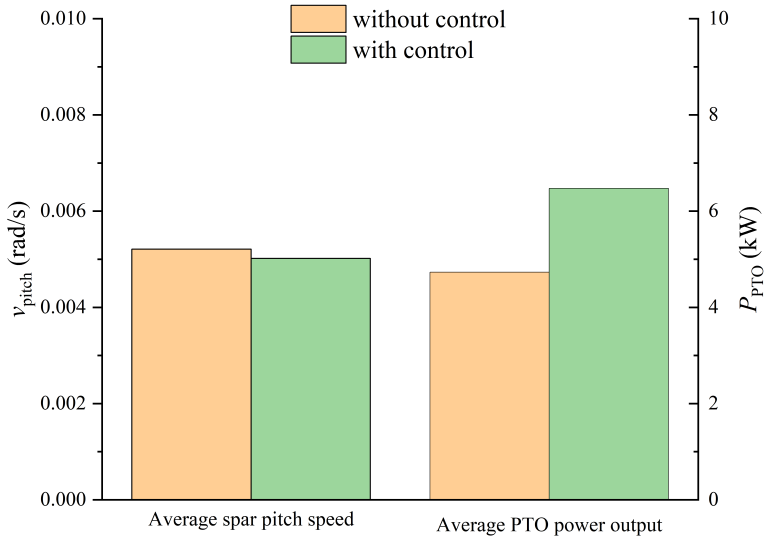

Figure 6.22: The control effect in irregular waves.

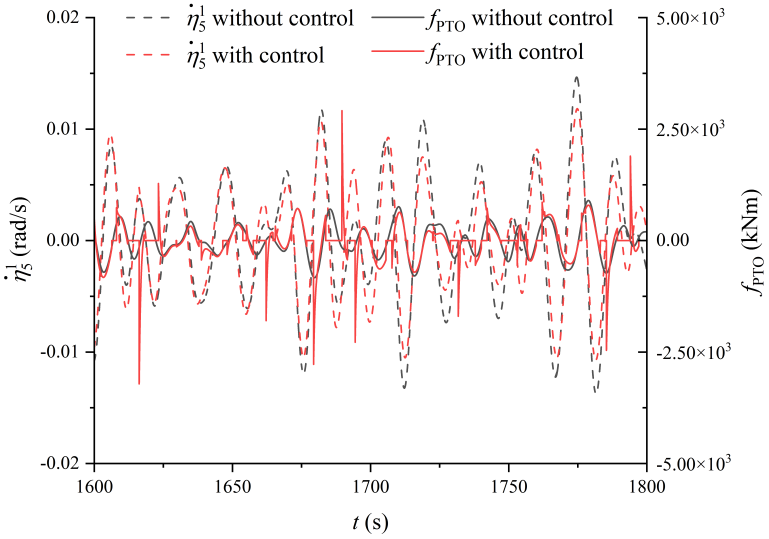

Figure 6.23: Time domain results of the spar-plate system in irregular waves.

Plate mass

The plate mass is non-dimensionalised by the mass of platform. The ratio of inertia moment in the pitch direction between plate and spar-type platform is defined as,

$$r_{\mathrm{M}} = \frac{I_{55}^2 + m_{55}^2}{I_{55}^1 + m_{55}^1} \tag{6.12}$$

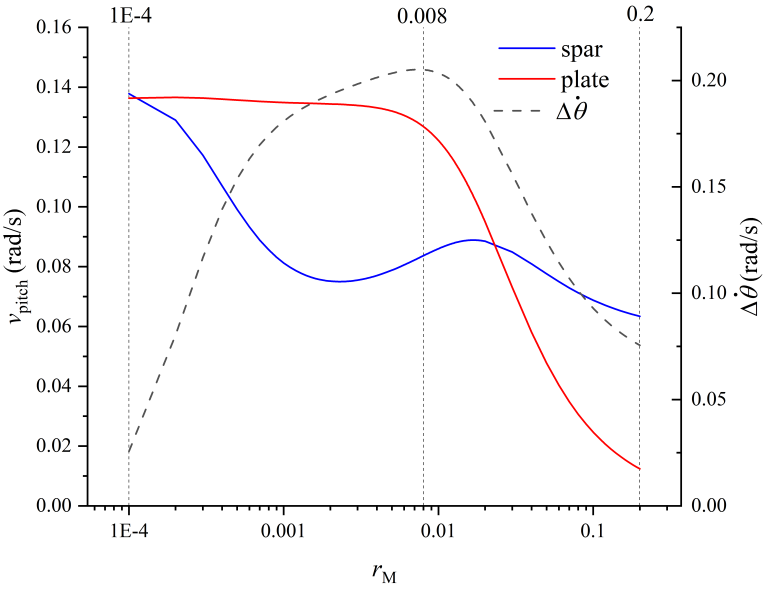

Figure 6.24: The pitch velocity of the spar-type platform and plate, and their relative pitch speed under different mass ratios (The r_{M} is shown in logarithmic scale).

where I_{55}^1 is the platform's moment of inertia in pitch direction; m_{55}^1 is the platform's added moment of inertia in infinite frequency in pitch direction; I_{55}^2 is plate's moment of inertia in pitch direction; m_{55}^2 is the plate's added moment of inertia in infinite frequency in pitch direction. In the initial design of the spar-plate system, the r_{M} was determined to be 1.38×10^{-4}, indicating a notably small plate size. In the physical world, with the enlargement of the plate size, the plate mass and added mass (moment of inertia) will be accordingly increased. Therefore, r_{M} can also represent the plate size, assuming constant density.

All results are calculated at a resonant wave frequency of 0.34 rad/s. Figure 6.24 shows the performance of v_{pitch} and $\Delta\dot{\theta}$ without control under different r_{M}. The x-axis of Fig. 6.24 is set in logarithmic scale to zoom in on the small mass ratio.

As illustrated in Fig. 6.24, when without control and r_{M}<0.008, v_{pitch} decreases with r_{M} and $\Delta\dot{\theta}$ increases with r_{M}. The platform and plate experience identical wave phases, due to their alignment in a vertical plane. When plate mass is small, the B_{PTO} is large enough to minimise $\Delta\dot{\theta}$. If the plate mass is increased, the damping force cannot limit the relative motion between the platform and plate anymore because of

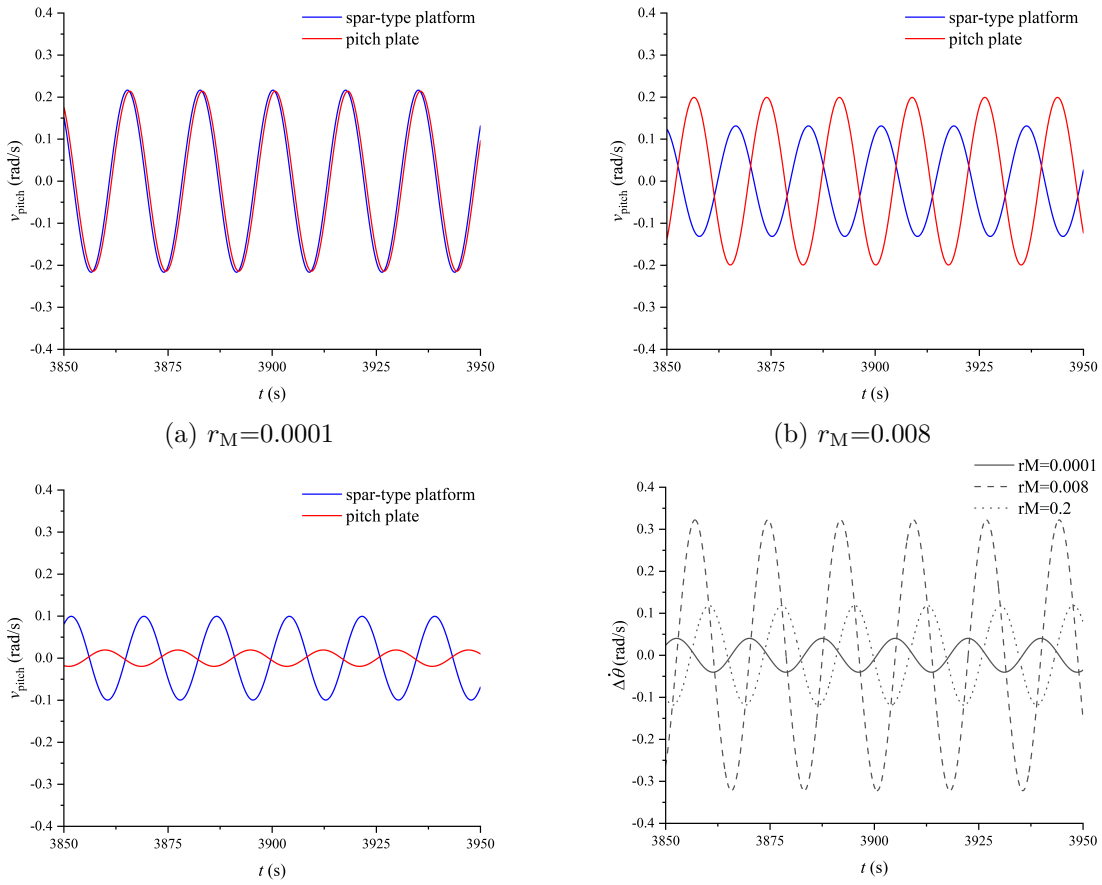

(a) r_{M}=0.0001

(b) r_{M}=0.008

(c) r_{M}=0.2

(d) $\Delta\dot{\theta}$ when r_{M}=1×10^{-4}, 0.008, and 0.2

Figure 6.25: The phase relationship of pitch velocity of spar-type platform and plate when r_{M}= (a)1×10^{-4}, (b)0.008, and (c)0.2. (d)The relative pitch velocity under the above three mass ratios.

the increased inertia of the plate. In Fig. 6.25a and 6.25b, with the increase of r_{M} and the decrease of PTO damping effect, the phase difference of the two bodies' motion increases. This implies that the relative pitch motion, $\Delta\theta$, between the two bodies would be increased. The increased $\Delta\theta$ will provide more damping force to the platform and hence decrease its motion. The increase of $\Delta\theta$ is also reflected in the increase of $\Delta\dot{\theta}$ in Fig. 6.24. When r_{M}=0.008, the response of the plate is anti-phase with the platform. $\Delta\dot{\theta}$ reaches its maximum at this r_{M}. When r_{M}>0.008, the mass of the plate is the dominant influence factor and the PTO damping effect can be neglected. The increase of plate mass results in the reduction of motion. Therefore, the decreased $\Delta\theta$

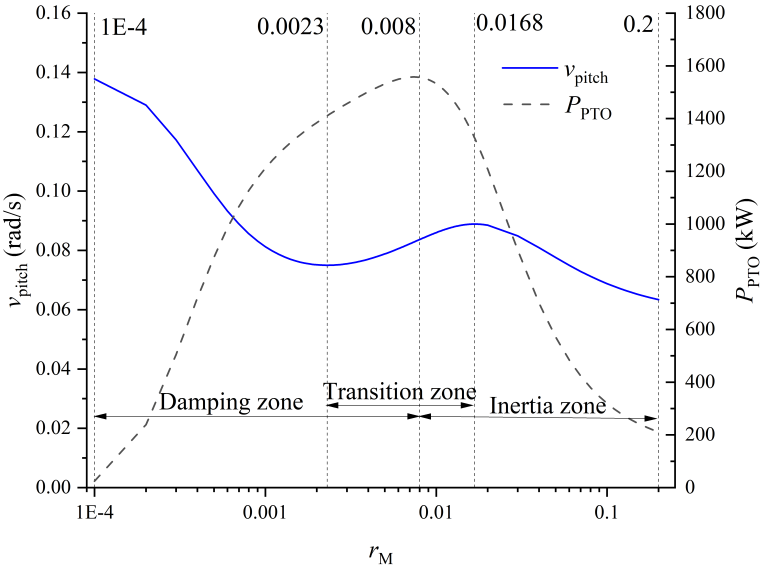

Figure 6.26: The pitch velocity of the spar-type platform and the PTO power output under different mass ratios (The r_M is shown in logarithmic scale).

results in a further decrease of v_{pitch}.

The P_{PTO} is directly related to the relative pitch velocity $\Delta\dot{\theta}$. Consequently, the resulting trends in Fig. 6.26 align closely with those depicted in Fig. 6.24. These trends can be categorised into three distinct zones. The left zone (r_M ranges from 1×10^{-4} to 0.008) is the "Damping force zone" where the effect of PTO damping is dominant. The right zone (r_M ranges from 0.008 to 0.2) is the "Inertia force zone" where the effect of plate mass is dominant. Between them is the "Transition zone" (r_M ranges from 0.0023 to 0.0168) where the dominance of PTO damping is transited to the plate mass.

Figure 6.27a shows that the control algorithm maintains to reduce v_{pitch} in the "Damping force zone" . This suggests that the pitch plate can still control the platform's motion effectively even when the plate mass is much smaller than the spar mass. However, the control effect reduces with r_M. When the mass ratio is larger than 0.005, the system enters the "Inertia force zone" . In this zone, the efficacy of control in optimising motion becomes markedly small. The reduction in control efficacy is because the relative magnitude of the damping force is considerably smaller than the inertia force and thus has limited influence on the motion performance. The dividing line

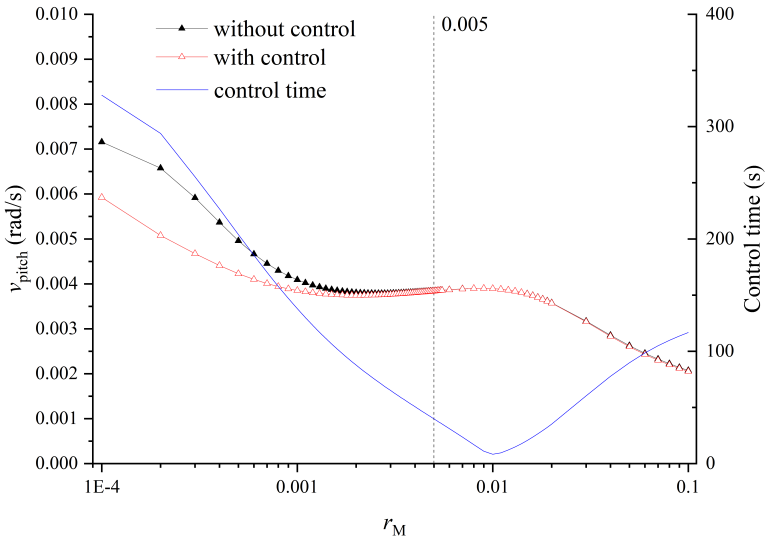

(a) v_{pitch} of spar-type platform.

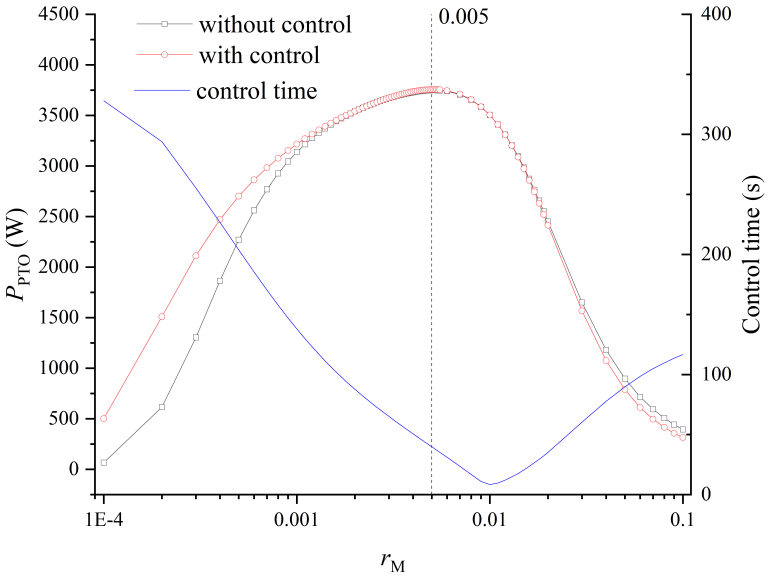

(b) P_{PTO} of PTO.

Figure 6.27: Performance indices under different plate mass ratios. (a) Average pitch speed of the spar-type platform; (b) Average power absorption of PTO.

at 0.005, differing slightly from the previously noted 0.008, is attributed to potential variations in the system's performance when under control.

When r_{M} grows, the average power absorption increases, but the declutching time length goes down. With the increase of r_{M}, it grows harder for the plate to accelerate

when declutching control happens. The amplitude of relative angular velocity becomes smaller. The necessity of control declines, which is reflected in the reduction of control time. Less declutching indicates the average B_{PTO} is larger. The control time reduces to 0 when r_{M} reaches 0.005. The system absorbs the most energy when r_{M}=0.005. When plate mass continues to grow, the average B_{PTO} stops growing, however, the relative angular velocity will continue decreasing, thus the power begins to decrease.

PTO damping coefficient

During the optimisation in the declutching control, B_{PTO} and $\Delta\dot{\theta}$ both vary with the value of the control command. The average value of B_{PTO} depends on the control time length. Therefore, the effect of control is directly decided by the declutching control time length (or power take-off time length). In order to get the best performance in declutching control, we need to compare the power absorption under declutching optimal control with different B_{PTO}.

The current configuration sets r_{M} at 1.38×10^{-4}. With such a low plate mass, B_{PTO} has a negligible influence on the natural frequency of the spar-type platform, while significantly affecting the plate's natural frequency. When B_{PTO} is sufficiently large, the relative angular velocity of the spar and plate becomes 0. In such a situation, the motion of this hinged system can be regarded as a "welded" mode.

When not applying control to the system, the power absorption is observed to reach its peak at the wave frequency of 0.34 rad/s, as shown in Fig. 6.28a. The motion mitigation effect at lower frequencies ($\leq$ 0.34 rad/s) is better than at higher frequencies ($>$ 0.34 rad/s). Consequently, a more detailed comparative analysis is needed for the results obtained under a wave frequency of 0.34 rad/s across various B_{PTO}.

Figure 6.29 demonstrates a comparison of results with and without control. The control results in Fig. 6.29a show that, with the increase of B_{PTO}, the effect of damping force gradually grows, becoming sufficiently large enough to influence the motion of the platform. The controlled v_{pitch} has a little variation with the increase of B_{PTO}. This is because the average damping coefficient with declutching control can remain consistent, regardless of the magnitude of B_{PTO}. At high B_{PTO} values, the controlled pitch speed

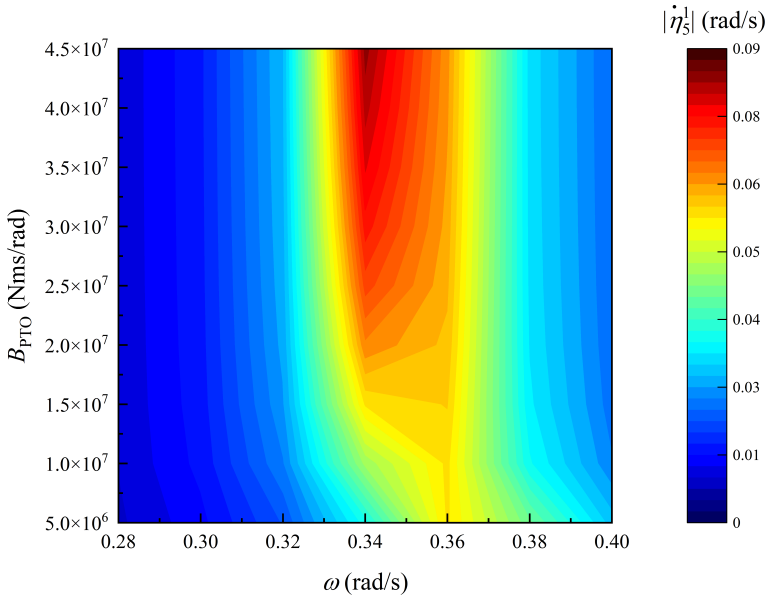

(a) Without control.

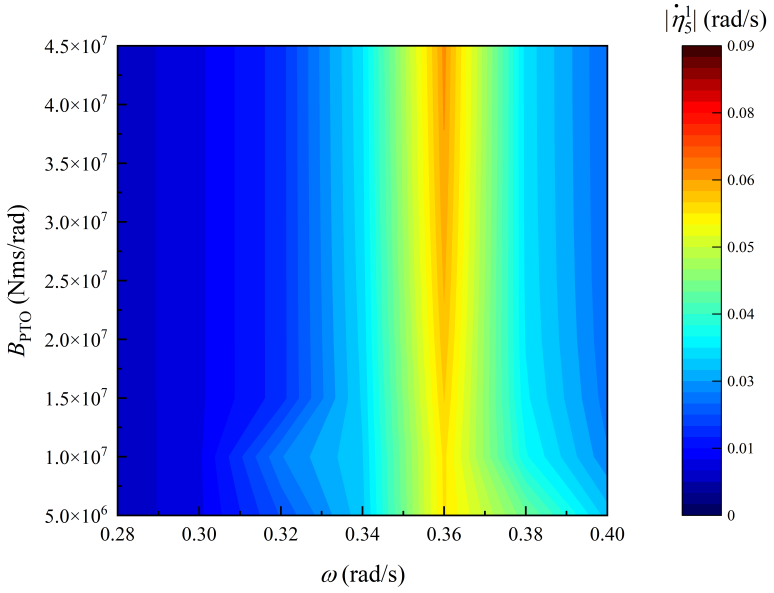

(b) With control.

Figure 6.28: The contour plot of v_{pitch} under different PTO damping and wave frequencies.

presents similar values to each other.

The results in Fig. 6.29b also imply that B_{PTO} hardly has an influence on the control effect when its amplitude is large enough. The reason is that when B_{PTO} is

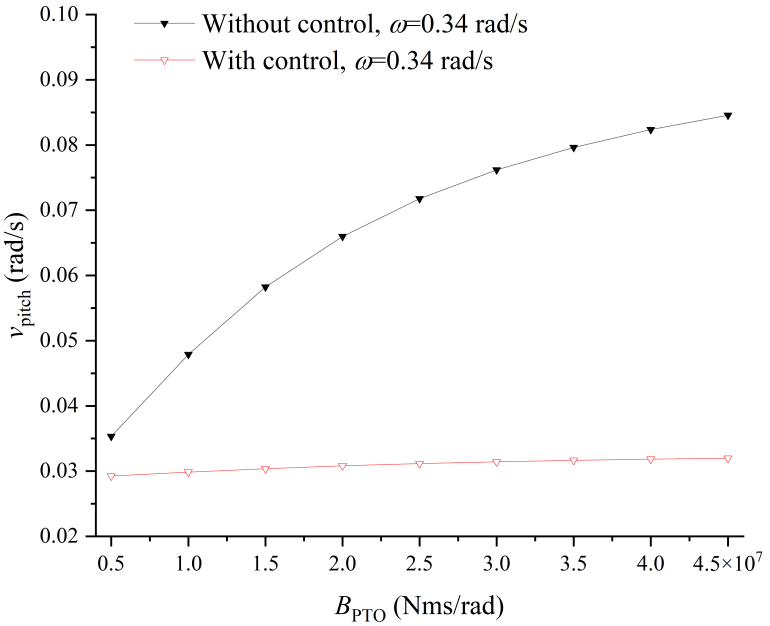

(a) v_{pitch} of the spar-type platform.

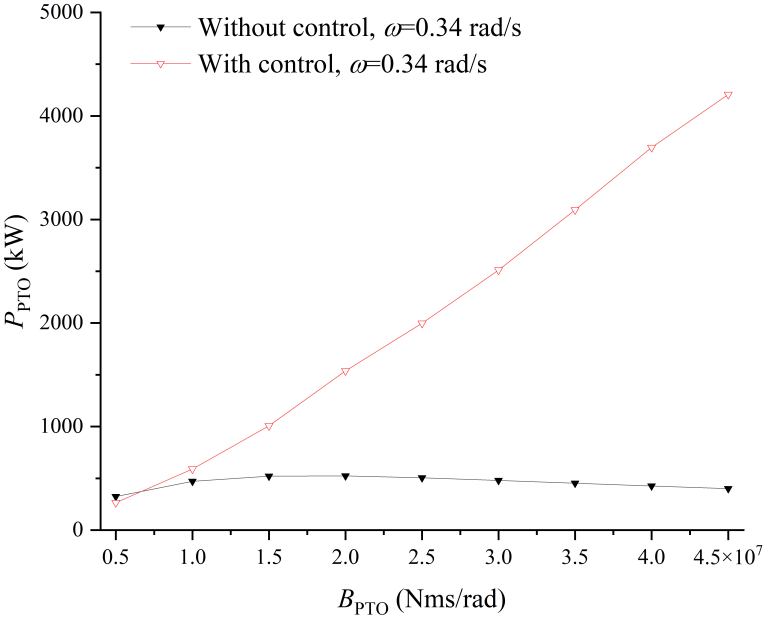

(b) P_{PTO} of the PTO system.

Figure 6.29: The performance under different PTO damping of the spar-plate system when wave frequency is at 0.34 rad/s.

adequately large, the behaviour of declutching control becomes more similar to that of latching control. When the control command is 0, the bodies are effectively latched

together. Conversely, when the control command is 1, the relative rotational motion between the bodies is released.

6.4 Summary

The proposed control method successfully achieves motion mitigation across various scenarios. Each of the individual cases in this chapter has distinct configurations of connections and primary motion directions. Despite these differences, all cases consistently validate the function of our method in mitigating motion. In addition, the mass of the auxiliary structure and the damping coefficient of the PTO system are key factors influencing the effectiveness of the control strategy.

Chapter 7

Control of Multiple Floating WECs

7.1 Introduction

Aiming to solve the challenges with the discontinuous objective function $\bar{J}_4$ and issues of convergence encountered in section 5.5, this chapter explores the application of various optimal control methods in achieving effective control over a real-world multi-body WEC. Given that the dynamics of two-body hinged boxes have been extensively analysed in Chapter 5, this chapter primarily focuses on the dynamics and control of a three-body WEC.

7.2 Dynamic model of a three-body hinge-barge WEC

A detailed derivation of the dynamic equations and constraint matrices of a three-body system can be referred to in section 5.8. The case of the three-body system validates the extendibility of the proposed control method in a multi-body system consisting of more than two bodies. The motion can be solved with Eq. 3.20, however, the constraint matrix and control algorithm need updating.

In this chapter, a full-scale model based on the McCabe Wave Pump design [85, 86] is analysed. The computational model is a hinge-barge WEC composed of three

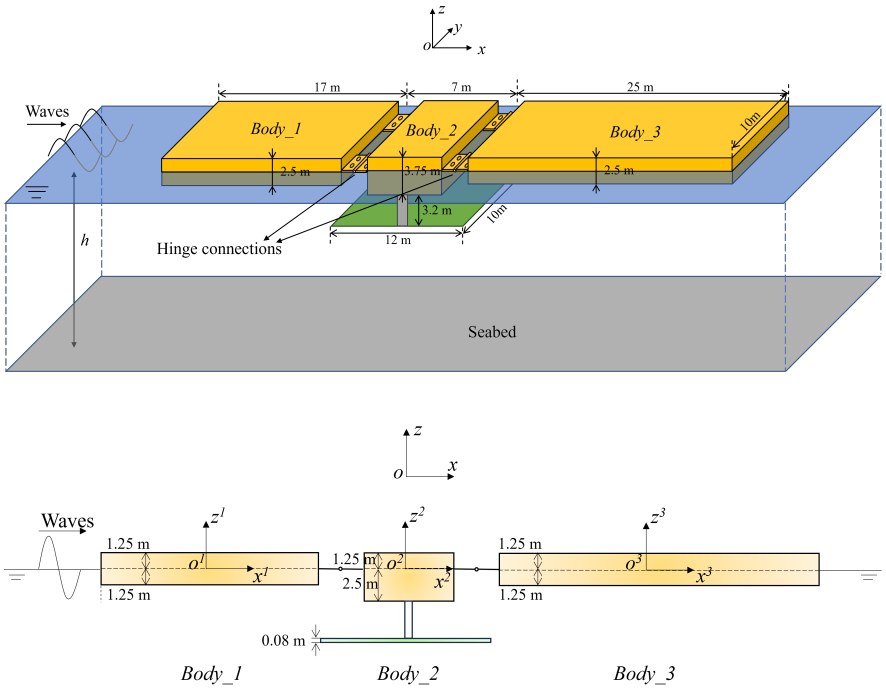

Figure 7.1: Configuration of the three-body hinge-barge WEC.

rectangular bodies: *Body*_1 as the fore barge, *Body*_2 as the central barge, and *Body*_3 as the aft barge. The configuration of the multi-body WEC is depicted in Fig. 7.1. The damping plate connected to *Body*_2 aims to reduce the vertical motion of *Body*_2, increasing the pitch motions of *Body*_1 and *Body*_3. The global coordinate system $o-xyz$ is a right-handed Cartesian coordinate system with $x-y$ axes in the horizontal water plane and z axis oriented in the upward direction. The waves are propagating towards the positive x-axis throughout the computation. The motion responses are described in body-fixed coordinate systems $o^j - x^j y^j z^j$, where $j = 1, 2, 3$ corresponds to the j-th body. The dimensions selected for the barges and the heave plate are derived from one of the conducted geometry optimisation studies [85].

The interaction of radiation between the three bodies should be considered. The state vector is defined as $\boldsymbol{x} = [\eta^1, \eta^2, \eta^3, \dot{\eta}^1, \dot{\eta}^2, \dot{\eta}^3, u^1, u^{12}, u^{13}, u^{21}, u^2, u^{23}, u^{31}, u^{32}, u^3]^{\mathrm{T}}$, where η is the motion, $\dot{\eta}$ is the velocity, and u is the intermediate variable representing the radiation effect. The system matrix $\boldsymbol{A_r}$, the state matrix $\boldsymbol{B_r}$, and the output

matrix $\boldsymbol{C_r}$ for a three-body system can be written as,

$$\boldsymbol{A}_r = \begin{bmatrix} \boldsymbol{A}_r^1 & \mathbf{0} & & & \dots & & & \mathbf{0} \\ \mathbf{0} & \boldsymbol{A}_r^{12} & \mathbf{0} & & & & & \\ & \mathbf{0} & \boldsymbol{A}_r^{13} & \mathbf{0} & & \ddots & & \\ & & \mathbf{0} & \boldsymbol{A}_r^{21} & \mathbf{0} & & & \\ \vdots & & & \mathbf{0} & \boldsymbol{A}_r^2 & \mathbf{0} & & \vdots \\ & & & & \mathbf{0} & \boldsymbol{A}_r^{23} & \mathbf{0} & \\ & & \ddots & & & \mathbf{0} & \boldsymbol{A}_r^{31} & \mathbf{0} \\ & & & & & & \mathbf{0} & \boldsymbol{A}_r^{32} & \mathbf{0} \\ \mathbf{0} & & & & \dots & & \mathbf{0} & \boldsymbol{A}_r^3 \end{bmatrix},$$

$$\boldsymbol{B}_r = \begin{bmatrix} \boldsymbol{B}_r^1 & \mathbf{0} & \mathbf{0} \\ \mathbf{0} & \boldsymbol{B}_r^{12} & \mathbf{0} \\ \mathbf{0} & \mathbf{0} & \boldsymbol{B}_r^{13} \\ \boldsymbol{B}_r^{21} & \mathbf{0} & \mathbf{0} \\ \mathbf{0} & \boldsymbol{B}_r^2 & \mathbf{0} \\ \mathbf{0} & \mathbf{0} & \boldsymbol{B}_r^{23} \\ \boldsymbol{B}_r^{31} & \mathbf{0} & \mathbf{0} \\ \mathbf{0} & \boldsymbol{B}_r^{32} & \mathbf{0} \\ \mathbf{0} & \mathbf{0} & \boldsymbol{B}_r^3 \end{bmatrix}, \tag{7.1}$$

$$\boldsymbol{C}_r = \begin{bmatrix} \boldsymbol{C}_r^1 & \boldsymbol{C}_r^{12} & \boldsymbol{C}_r^{13} & \mathbf{0} & \mathbf{0} & \mathbf{0} & \mathbf{0} & \mathbf{0} & \mathbf{0} \\ \mathbf{0} & \mathbf{0} & \mathbf{0} & \boldsymbol{C}_r^{21} & \boldsymbol{C}_r^2 & \boldsymbol{C}_r^{23} & \mathbf{0} & \mathbf{0} & \mathbf{0} \\ \mathbf{0} & \mathbf{0} & \mathbf{0} & \mathbf{0} & \mathbf{0} & \mathbf{0} & \boldsymbol{C}_r^{31} & \boldsymbol{C}_r^{32} & \boldsymbol{C}_r^3 \end{bmatrix}$$

As stated in Chapter 5, the interaction between *Body_*1 and *Body_*3 can be ignored due to their distance. Therefore, $\boldsymbol{A}_r^{13}$, $\boldsymbol{A}_r^{31}$, $\boldsymbol{B}_r^{13}$, $\boldsymbol{B}_r^{31}$, $\boldsymbol{C}_r^{13}$, and $\boldsymbol{C}_r^{31}$ are replaced by 0 in Eq. 7.1. This simplification offers considerable advantages in computational speed and hardly has influences on results.

The form of constraint matrix $\boldsymbol{S}_{21}$ and $\boldsymbol{S}_{22}$ for each hinge is similar to Eq. 5.3, but

different in distances to hinge point R,

$$\boldsymbol{\eta}^2 = \begin{bmatrix} \eta_1^2 \\ \eta_2^2 \\ \eta_3^2 \\ \eta_4^2 \\ \eta_5^2 \\ \eta_6^2 \end{bmatrix} = \begin{bmatrix} 1 & 0 & 0 & 0 & 0 & 0 \\ 0 & 1 & 0 & 0 & 0 & R1+R2 \\ 0 & 0 & 1 & 0 & -(R1+R2) & 0 \\ 0 & 0 & 0 & 1 & 0 & 0 \\ 0 & 0 & 0 & 0 & 1 & 0 \\ 0 & 0 & 0 & 0 & 0 & 1 \end{bmatrix} \begin{bmatrix} \eta_1^1 \\ \eta_2^1 \\ \eta_3^1 \\ \eta_4^1 \\ \eta_5^1 \\ \eta_6^1 \end{bmatrix} + \begin{bmatrix} 0 \\ 0 \\ -R2 \\ 0 \\ 1 \\ 0 \end{bmatrix} [\Delta\theta] \tag{7.2}$$
$$= \boldsymbol{S}_{21}^1 \boldsymbol{\eta}^1 + \boldsymbol{S}_{22}^1 \boldsymbol{\Delta\theta}$$

$$\boldsymbol{\eta}^3 = \begin{bmatrix} \eta_1^3 \\ \eta_2^3 \\ \eta_3^3 \\ \eta_4^3 \\ \eta_5^3 \\ \eta_6^3 \end{bmatrix} = \begin{bmatrix} 1 & 0 & 0 & 0 & 0 & 0 \\ 0 & 1 & 0 & 0 & 0 & R2+R3 \\ 0 & 0 & 1 & 0 & -(R2+R3) & 0 \\ 0 & 0 & 0 & 1 & 0 & 0 \\ 0 & 0 & 0 & 0 & 1 & 0 \\ 0 & 0 & 0 & 0 & 0 & 1 \end{bmatrix} \begin{bmatrix} \eta_1^2 \\ \eta_2^2 \\ \eta_3^2 \\ \eta_4^2 \\ \eta_5^2 \\ \eta_6^2 \end{bmatrix} + \begin{bmatrix} 0 \\ 0 \\ -R3 \\ 0 \\ 1 \\ 0 \end{bmatrix} [\Delta\theta] \tag{7.3}$$
$$= \boldsymbol{S}_{21}^2 \boldsymbol{\eta}^2 + \boldsymbol{S}_{22}^2 \boldsymbol{\Delta\theta}$$

As stated in section 5.8, for a three-body system, the total constraint matrix is the product of the individual constraint matrices,

$$
\begin{aligned}
\boldsymbol{\eta} = \begin{bmatrix} \boldsymbol{\eta}^1 \\ \boldsymbol{\eta}^2 \\ \boldsymbol{\eta}^3 \end{bmatrix} &= \begin{bmatrix} \boldsymbol{I} & \boldsymbol{0} & \boldsymbol{0} \\ \boldsymbol{0} & \boldsymbol{I} & \boldsymbol{0} \\ \boldsymbol{0} & \boldsymbol{S}_{21}^2 & \boldsymbol{S}_{22}^2 \end{bmatrix} \begin{bmatrix} \boldsymbol{\eta}^1 \\ \boldsymbol{\eta}^2 \\ \boldsymbol{\Delta\theta}^2 \end{bmatrix} \\
&= \begin{bmatrix} \boldsymbol{I} & \boldsymbol{0} & \boldsymbol{0} \\ \boldsymbol{0} & \boldsymbol{I} & \boldsymbol{0} \\ \boldsymbol{0} & \boldsymbol{S}_{21}^2 & \boldsymbol{S}_{22}^2 \end{bmatrix} \begin{bmatrix} \boldsymbol{I} & \boldsymbol{0} & \boldsymbol{0} \\ \boldsymbol{S}_{21}^1 & \boldsymbol{S}_{22}^1 & \boldsymbol{0} \\ \boldsymbol{0} & \boldsymbol{0} & \boldsymbol{I} \end{bmatrix} \begin{bmatrix} \boldsymbol{\eta}^1 \\ \boldsymbol{\Delta\theta}^1 \\ \boldsymbol{\Delta\theta}^2 \end{bmatrix} \\
&= \begin{bmatrix} \boldsymbol{I} & \boldsymbol{0} & \boldsymbol{0} \\ \boldsymbol{S}_{21}^1 & \boldsymbol{S}_{22}^1 & \boldsymbol{0} \\ \boldsymbol{S}_{21}^2\boldsymbol{S}_{21}^1 & \boldsymbol{S}_{21}^2\boldsymbol{S}_{22}^1 & \boldsymbol{S}_{22}^2 \end{bmatrix} \begin{bmatrix} \boldsymbol{\eta}^1 \\ \boldsymbol{\Delta\theta}^1 \\ \boldsymbol{\Delta\theta}^2 \end{bmatrix} = \boldsymbol{S} \begin{bmatrix} \boldsymbol{\eta}^1 \\ \boldsymbol{\Delta\theta}^1 \\ \boldsymbol{\Delta\theta}^2 \end{bmatrix} = \boldsymbol{S}\boldsymbol{\eta}'
\end{aligned}
\tag{7.4}
$$

The motion equation remains the same form as Eq. 3.15 with an extended input $\boldsymbol{f}_{\mathrm{e}}(t) = [f_{\mathrm{e}}^1(t), f_{\mathrm{e}}^2(t), f_{\mathrm{e}}^3(t)]^{\mathrm{T}}$ and state vector $\boldsymbol{\eta}'(t) = [\eta^1(t), \Delta\theta^1(t), \Delta\theta^2(t)]^{\mathrm{T}}$. The input regular waves have the same configuration as in Section 5.5. The amplitude of the wave excitation force on *Body_*3, denoted as $f_{\mathrm{e}}^3(t)$, is relatively smaller than those acting on *Body_*1 and *Body_*2. The total number of DoF for the unhinged system is 18, while for the hinged system, it is reduced to 8: the 6-DoF motion of *Body_*2, and the pitch motion of *Body_*1 and *Body_*3. Each pair of adjacent bodies is interconnected by a single PTO unit. Under the assumption that both PTO systems have an identical configuration, the damping forces of the two units are expressed as follows,

$$
\begin{aligned}
f_{\mathrm{PTO}}^1 &= (B_{\mathrm{PTO}} + \beta^1 B_{\mathrm{c}})\Delta\dot{\theta}^1 \\
f_{\mathrm{PTO}}^2 &= (B_{\mathrm{PTO}} + \beta^2 B_{\mathrm{c}})\Delta\dot{\theta}^2
\end{aligned}
\tag{7.5}
$$

where β^1 and is the control command for the PTO between *Body_*1 and *Body_*2, while β^2 corresponds to the control command for the PTO between *Body_*2 and *Body_*3.

Figure 7.2 displays a contour plot of the total power output across different PTO damping coefficients and wave frequencies. The multiple peaks in the plot can be

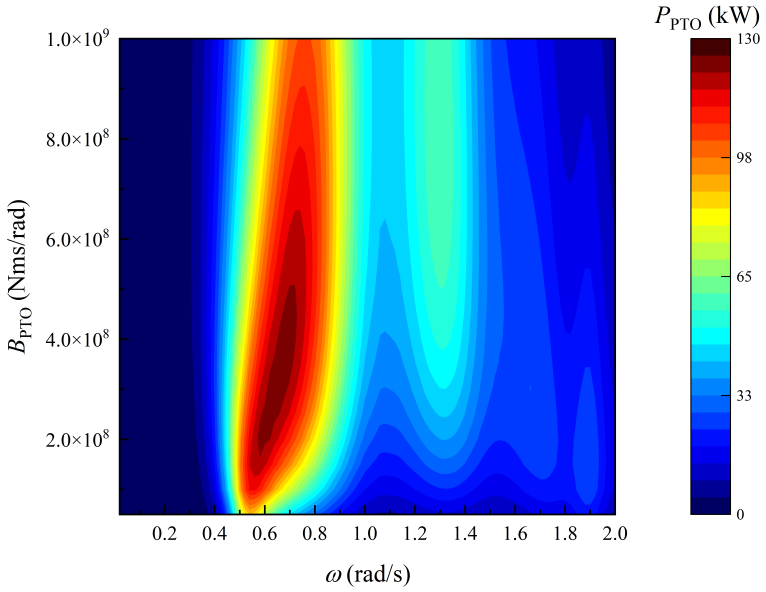

Figure 7.2: The contour plot of P_{PTO} under different PTO damping and wave frequencies.

attributed to the multiple resonance frequencies in the three-body system. The initial setting of the damping coefficient of the PTO, B_{PTO}, can be guided by the data presented in this figure.

7.3 Control under PMP

7.3.1 Reconstruction of objective function

In order to directly enhance the power absorption efficiency of the system, the objective function $\bar{J}$ is defined as the total power output of the two PTO systems,

$$\begin{aligned} \max\left(\bar{J}\right) &= \max\left(P_{\mathrm{PTO}}\right) \\ &= \max\left(\frac{1}{T}\int_0^{\mathrm{T}}\left[(B_{\mathrm{PTO}}+\beta^1 B_{\mathrm{c}})(\Delta\dot{\theta}^1)^2 + B_{\mathrm{PTO}}+\beta^2 B_{\mathrm{c}})(\Delta\dot{\theta}^2)^2\right]dt\right) \end{aligned} \tag{7.6}$$

which has a similar form to $\bar{J}_4$ as detailed in Chapter 5. In the following analysis, this objective function aiming at optimising the P_{PTO} will continue to be referred to as $\bar{J}_4$.

By solving the value of co-state $\boldsymbol{\lambda}$, the Hamiltonian H containing $\beta^1(t)$ and $\beta^2(t)$

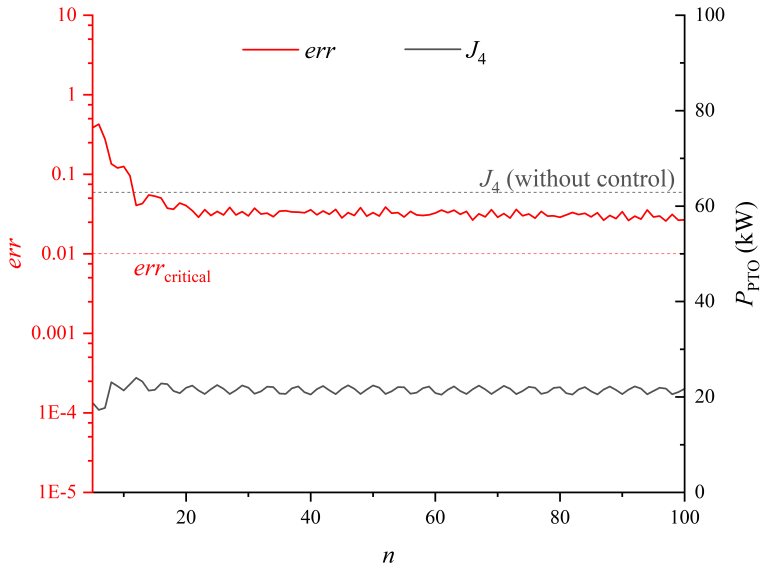

Figure 7.3: The variation of err and P_{PTO} with the number of iterations under declutching control.

can be derived. During the control process, the two separate control commands $\beta^1(t)$ and $\beta^2(t)$ will have the same rules as in Eq. 4.6 for deciding their values respectively. However, due to the different dynamics of the two pairs of adjacent bodies, the optimal control commands will be different.

7.3.2 Control results

The damping coefficient of PTO B_{PTO} is set to 6×10^7 Nm·s/rad and the wave frequency of incoming regular wave is set to 0.66 rad/s. Fig. 7.3 illustrates the variation of both err and P_{PTO} across different iteration numbers. Unfortunately, the performance depicted in both parameters is not optimal. The err fails to decrease below the critical threshold err_{critical}, indicating a tendency for the results to fluctuate without convergence. Furthermore, the P_{PTO} observed under control is lower than without control, suggesting that the optimisation process may not be fully effective and potentially be trapped in local optima.

A further examination of $\Delta\dot{\theta}$ and P_{PTO} observed in PTO_1 as presented in Fig. 7.4 reveals the underlying reasons for the observed non-optimal performance. When without control, the phase between $\Delta\dot{\theta}$ and f_{PTO} was initially the same. The implemen-

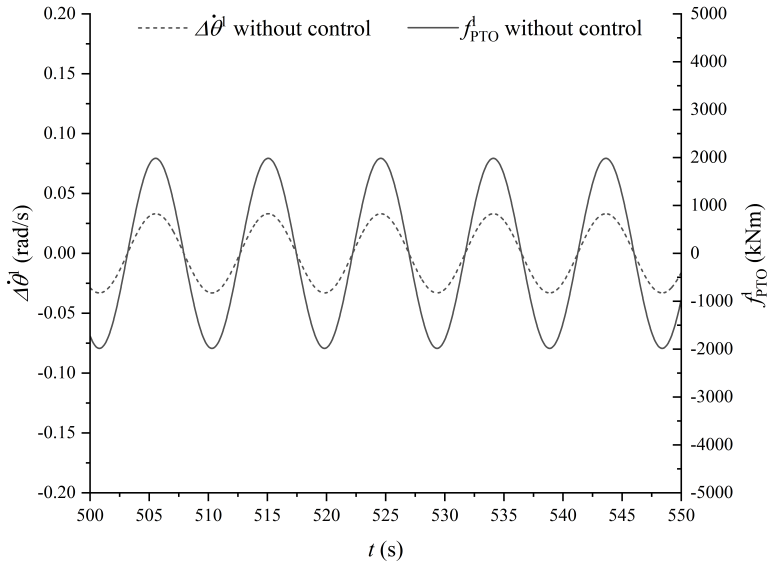

(a) Without control.

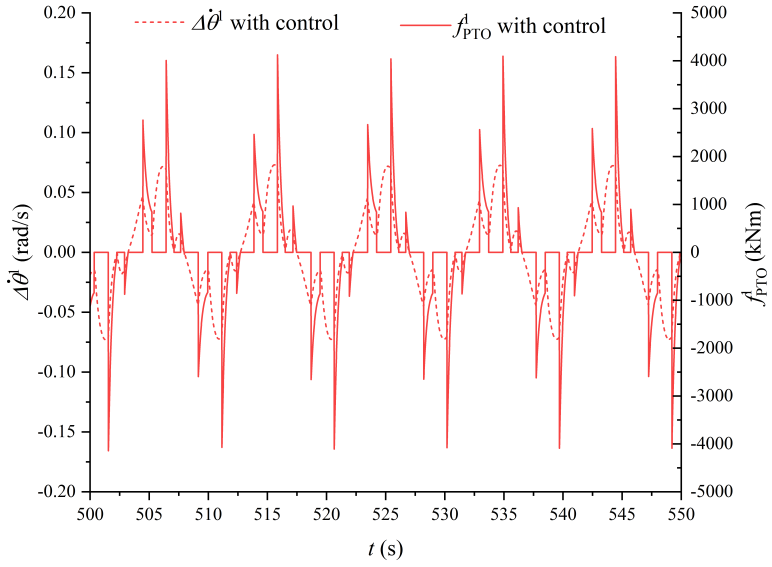

(b) With control.

Figure 7.4: The relationship of $\Delta\dot{\theta}$ and P_{PTO} of PTO_1 when (a) without control and (b) with control.

tation of declutching control, while amplifying the maximum amplitude, also reduced the value to zero at some horizons, thereby reducing the overall average value. The performance of PTO_2 is similar and not shown herein.

Figure 7.5 depicts the eventual total power output. The results indicate that the

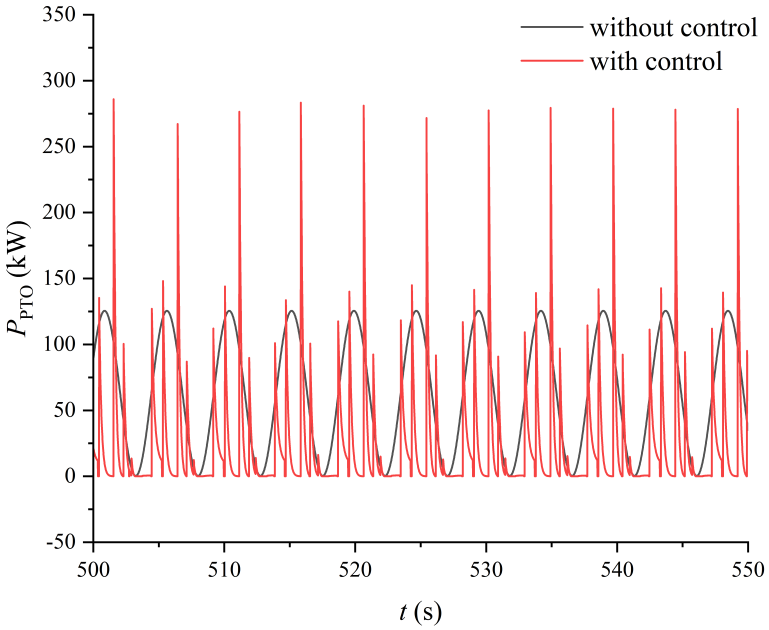

Figure 7.5: The total power output of the system under declutching control.

time variation of P_{PTO} has many fluctuations and does not show any significant enhancement.

Figure 7.6 illustrates the variation of both err and P_{PTO} across different iteration numbers when B_{PTO} is set to 6×10^8 Nm·s/rad. The err succeeds in decreasing below the critical threshold err_{critical}, showing a better convergence in this situation. However, P_{PTO} is still not well optimised.

7.3.3 Alternative strategies under PMP

Latching control approach

The latching control strategy employs an infinitely added damping coefficient to prevent relative motion between floating bodies. This control strategy does not directly alter the damping coefficient used in the PTO power calculation, expressed as $P_{\mathrm{PTO}} = B_{\mathrm{PTO}}\Delta\dot{\theta}^2$, and it only affects the relative pitch motion $\Delta\dot{\theta}$. This approach effectively reduces the discontinuity of the objective function, thereby enhancing the possibility of convergence. However, it is noteworthy that when latching control reduces $\Delta\dot{\theta}$ to zero, the objective function may still exhibit discontinuity.

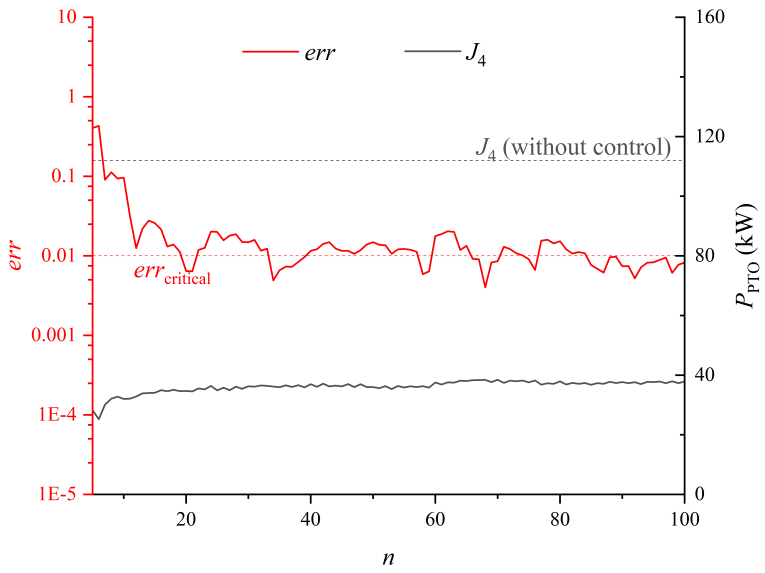

Figure 7.6: The variation of err and P_{PTO} with the number of iterations when $B_{\mathrm{PTO}} = 6 \times 10^8$.

The B_{PTO} and wave frequency are configured the same as declutching control. Therefore, results when without control are the same. The comparison of results obtained under declutching and latching control are presented in Fig. 7.7. The results under latching control demonstrate rapid convergence, as evidenced by the err falling below err_{critical} quickly. P_{PTO} is effectively optimised when latching control is applied. The power output with control is 17.46% higher than without control.

The details of $\Delta\dot{\theta}$ and P_{PTO} observed in PTO_1 and PTO_2 are respectively presented in Fig. 7.8. The relationship demonstrates that the results are effectively optimised under latching control because of the collaboration of two PTO systems. When without control, the phase between $\Delta\dot{\theta}$ and f_{PTO} was initially the same. The application of latching control restricts a portion of the relative motion between *body*_1 and *body*_2. When *body*_1 and *body*_2 are latched together, the motion of *body*_2 is reduced and the relative motion between *body*_2 and *body*_3 increases. Therefore, the latching control simultaneously results in the release of relative motion between *body*_2 and *body*_3, thereby enhancing the overall average power output.

Figures 7.9 and 7.10 depict the eventual total P_{PTO} and the P_{PTO} of the two PTO systems respectively. The results indicate that the P_{PTO} under latching control is

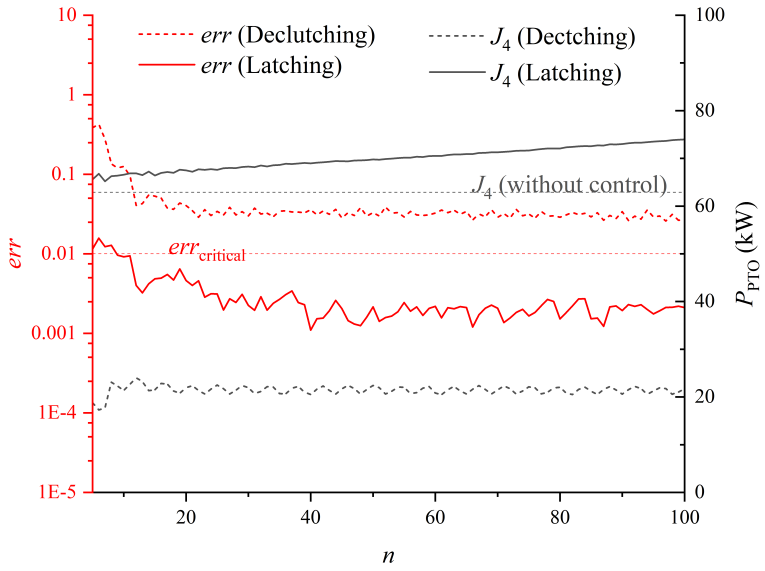

Figure 7.7: The variation of err and P_{PTO} with the number of iterations under latching control.

generally higher than without control. The control effect observed on PTO_1 is better than that of PTO_2, which corresponds to the change of $\Delta\dot{\theta}$ and f_{PTO} in Fig. 7.8. Figure 7.11 displays the controlled PTO damping coefficients, illustrating the actions of PTO_1 and PTO_2. The activation of control in these two PTO systems does not occur simultaneously.

Overall, these findings highlight that latching control is an alternative control strategy for enhancing the efficiency of PTO systems in multi-body WECs.

Wave energy control

According to the discussion in Chapter 5, the objective function $\bar{J}_4$ is designed to represent the maximisation of power absorbed by the PTO system, while $\bar{J}_2$ is formulated to represent the maximisation of the total work done by the wave force. $\bar{J}_2$ has a better control effect and convergence speed than $\bar{J}_4$ because of its continuity. This subsection aims to undertake a comparative analysis of these two objective functions, investigating the difference in their respective influences.

The objective function $\bar{J}_2$ represents the total wave power, specifically the average value of work performed by the wave force on the system,

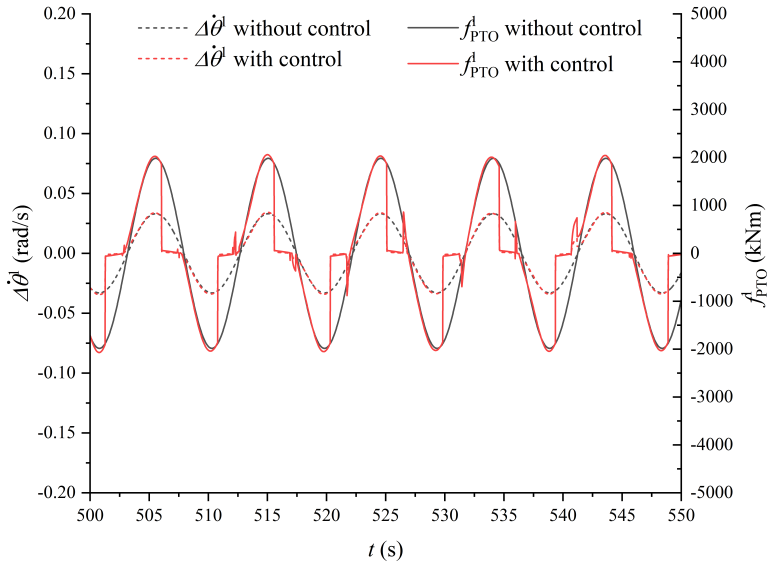

(a) PTO_1.

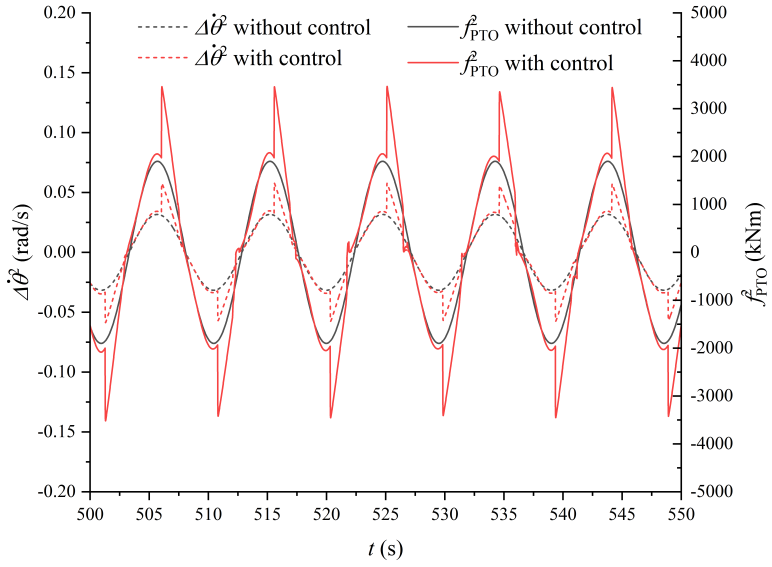

(b) PTO_2.

Figure 7.8: The relationship of $\Delta\dot{\theta}$ and P_{PTO} of (a) PTO_1 and (b) PTO_2 under latching control.

$$\begin{aligned}\max\left(\bar{J}_2\right) &= \max\left(P_{\mathrm{wave}}\right) \\ &= \max\left(\frac{1}{T}\int_0^T \left[f^1_{\mathrm{wave}}(t)\dot{\eta}^1(t) + f^2_{\mathrm{wave}}(t)\dot{\eta}^2(t) + f^3_{\mathrm{wave}}(t)\dot{\eta}^3(t)\right] dt\right)\end{aligned} \tag{7.7}$$

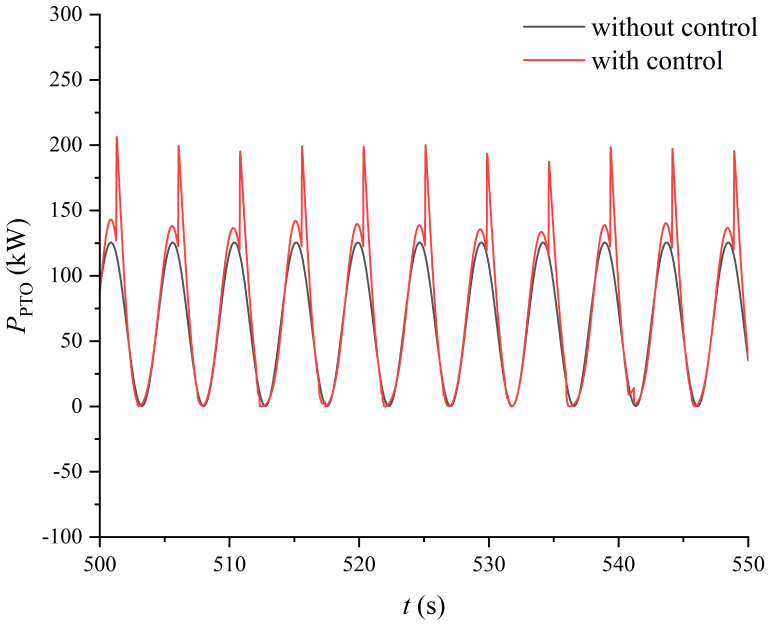

Figure 7.9: The total power output of the system under latching control.

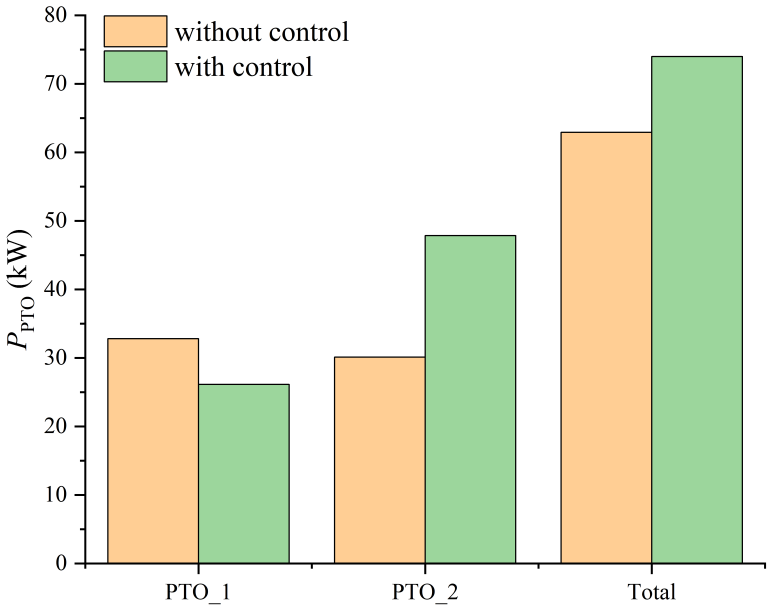

Figure 7.10: The power output of the two PTO systems under latching control.

This objective function does not include discontinuous terms and aligns closely with the goal of enhancing the efficiency of wave energy absorption. While it does not directly represent the power output of the PTO system, it can exert a similar effect in terms of

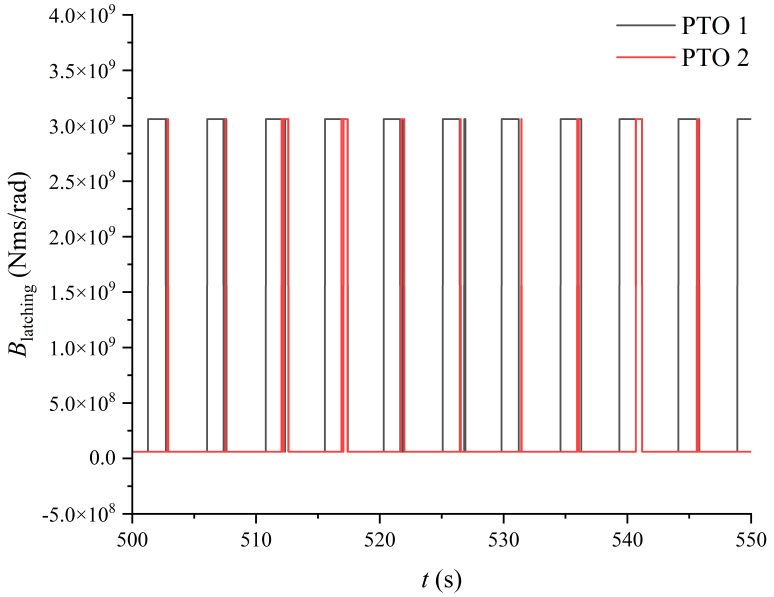

Figure 7.11: The controlled PTO damping coefficients of the system under latching control.

optimising energy capture.

The B_{PTO} is adjusted to 1×10^9 Nm·s/rad and the wave frequency is set to 0.4 rad/s, in order to observe a more obvious control effect. The results in Figs. 7.12 indicate that the variation in wave power can indirectly result in the variation of PTO power output as a "by-product". This phenomenon is likely attributed to the inherent mechanics of wave energy conversion systems, where the efficiency of PTO systems is naturally linked to the energy input from wave power. However, after convergence, the results indicate a decline in performance. Consequently, we have selected the control commands and results obtained before $n = 16$ as representative of optimised results.

The analysis presented in Fig. 7.13 provides a detailed examination of the variables $\Delta\dot{\theta}$ and f_{PTO} of PTO_1 and PTO_2 respectively. The performance of f_{PTO} for both PTO_1 and PTO_2 are similar, with amplifications observed in both $\Delta\dot{\theta}$ and f_{PTO} during the in-phase horizon. The behaviours of $\Delta\dot{\theta}$ of each PTO are different. When f_{PTO} is zero, $\Delta\dot{\theta}$ of PTO_1 is amplified, whereas for PTO_2, it is also reduced to zero.

Figures 7.14 and 7.15 collectively display the variation of total power output P_{PTO}

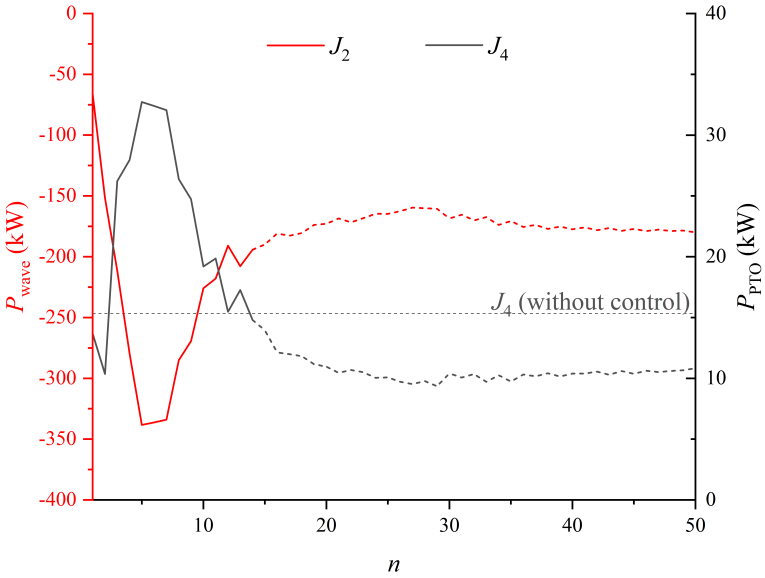

Figure 7.12: The variation of err and P_{PTO} with the number of iterations under the objective function $\bar{J}_2$.

and the individual power outputs enhancement of the two distinct PTO systems, PTO_1 and PTO_2. The power output under objective function $\bar{J}_2$ is generally higher than without control and the control effect on two PTO systems is similar. Figure 7.16 displays the controlled PTO damping coefficients, illustrating the actions of PTO_1 and PTO_2. The frequency of declutching control activation in PTO_1 is notably higher, leading to an amplification of its average $\Delta\dot{\theta}$. The increased motion in $body\_2$ subsequently reduces the necessity for $body\_3$ to accelerate, resulting in a less frequent activation of declutching control in PTO_2.

In summary, while with its limitations, these findings highlight the considerable potential of wave energy control as an alternative strategy for enhancing the efficiency of PTO systems in multi-body WECs.

7.4 Control under non-smooth optimisation

Due to the challenges in achieving convergence for PTO power output ($\bar{J}_4$) when using PMP, it becomes necessary to explore alternative optimal control methods. In this context, the non-smooth optimisation becomes a highly suitable option, particularly for

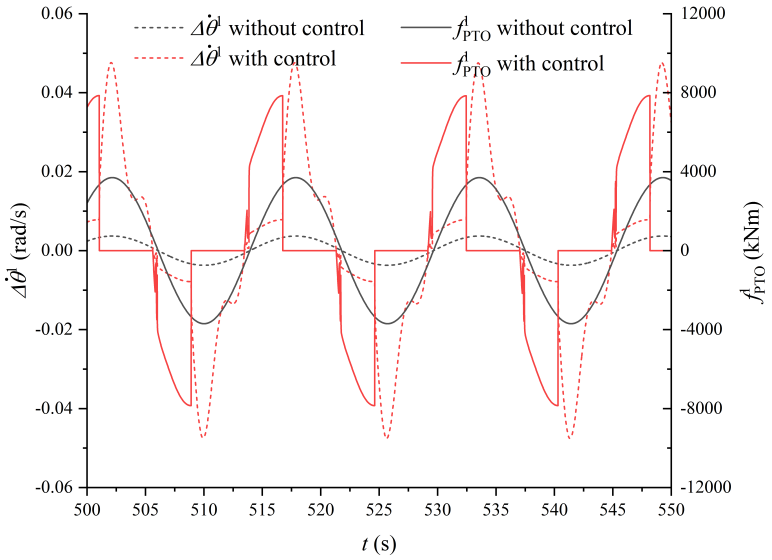

(a) *PTO*_1.

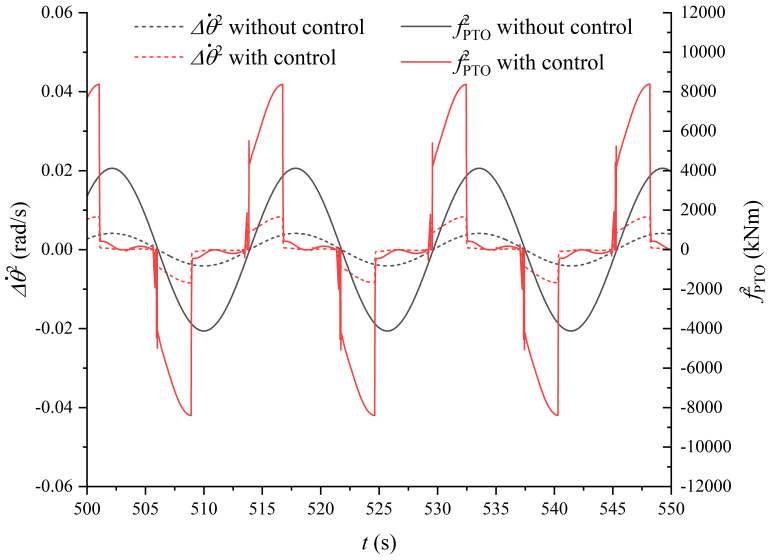

(b) *PTO*_2.

Figure 7.13: The relationship of $\Delta\dot{\theta}$ and P_{PTO} of (a) *PTO*_1 and (b) *PTO*_2 under objective function $\bar{J}_2$.

a discontinuous objective function.

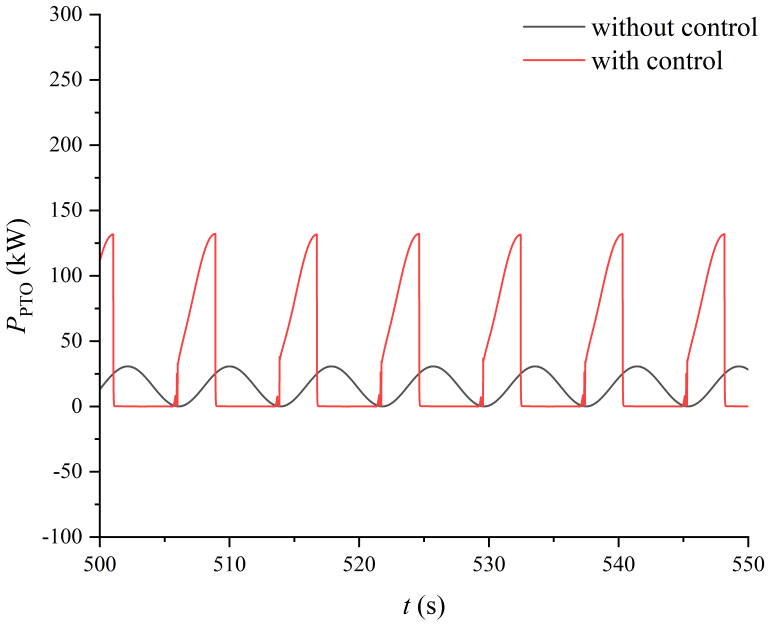

Figure 7.14: The total power output of the system under objective function $\bar{J}_2$.

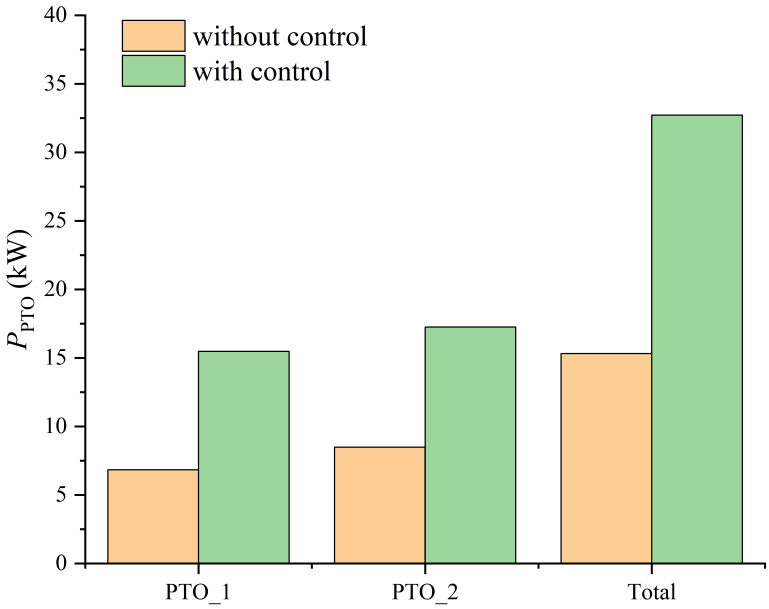

Figure 7.15: The power output of the two PTO systems under objective function $\bar{J}_2$.

7.4.1 Non-smooth optimisation

Non-smooth optimisation is a branch of optimisation theory dealing with problems where the objective function or the constraints are not differentiable at all points in

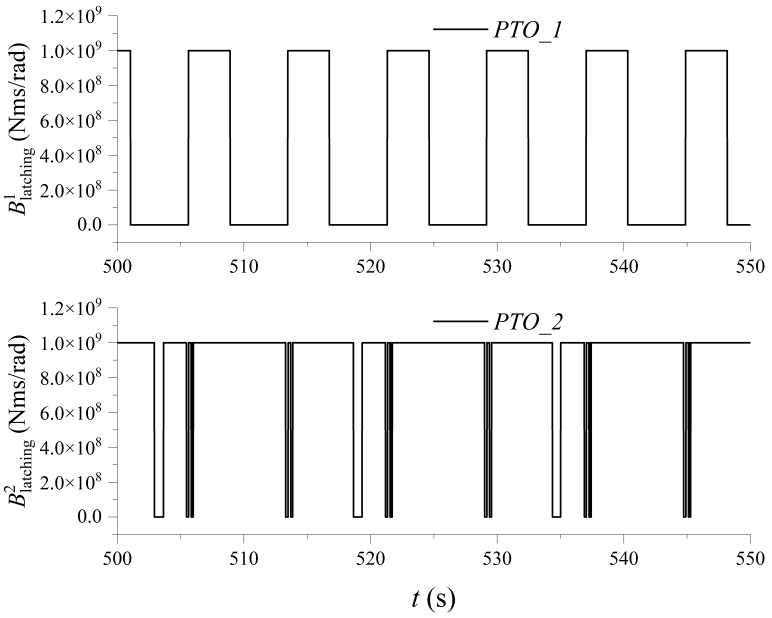

Figure 7.16: The controlled PTO damping coefficients of the system under objective function $\bar{J}_2$.

their domain. Traditional optimisation techniques, such as PMP, often rely on the smoothness of the objective function, particularly the existence of derivatives. However, in the problem related to declutching control, the PTO damping coefficient B_{d} involved in the objective function is a discontinuous function. It switches between a constant B_{PTO} and 0 with the opening and closing of the by-pass valve.

To handle this discontinuity, non-smooth optimisation techniques like sub-gradient method have been developed. The sub-gradient method is an extension of the gradient method used for smooth functions. For non-smooth functions, the gradient at a point may not exist, but sub-gradients (generalisations of gradients) can be used instead. The method iteratively updates the solution in a direction determined by a sub-gradient of the function at the current point. Unlike gradients, sub-gradients do not necessarily point in the steepest descent direction, thus the method requires careful step size selection.

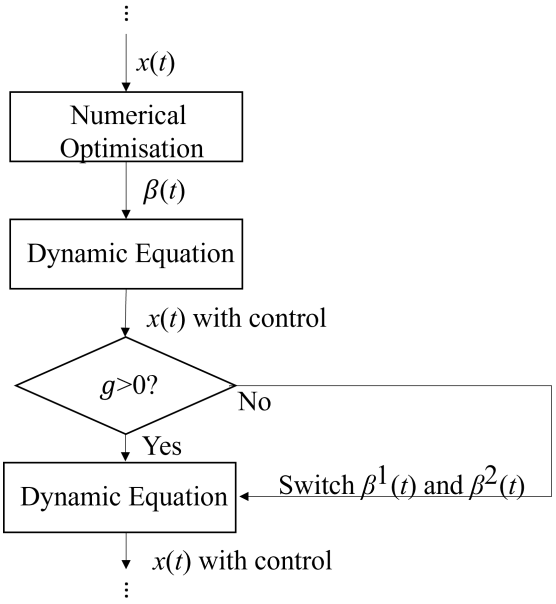

Figure 7.17: The flow chart of sub-gradient optimisation.

7.4.2 Control results

In the context of the declutching control applied in this thesis, the control command, β, operates on a binary 0-1 basis. This will lead to a fixed step size, as β is limited to switching exclusively between 0 and 1. As a result, the process of updating β can be simplified as a judgement. The sub-gradient of the objective function $\bar{J}_4$ is defined as g. If $g \geq 0$, β remain unchanged; if $g < 0$, β switches to the alternative binary value. A segment of the corresponding flow chart explaining this concept is depicted in Fig. 7.17.

With sub-gradient optimisation, it is easier to escape local optima, thereby increasing the possibility of achieving convergence. The critical error err_{critical} is still set as 0.01. The results are smoother curves of convergence for both err and P_{PTO}, especially when compared to the performance under declutching control alone. The sub-gradient method shows the potential to effectively mitigate the fluctuations and instabilities of declutching control. The final controlled P_{PTO}, despite declines and convergences to a lower value, is still higher than those obtained without control. This indicates that the control strategy, despite not maximising P_{PTO} to its highest potential value, still

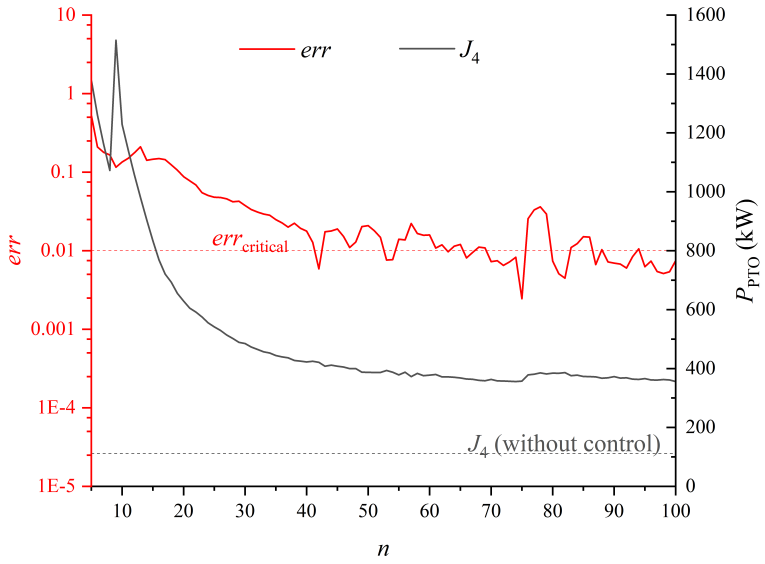

Figure 7.18: The variation of err and P_{PTO} with the number of iterations with sub-gradient optimisation.

enhances the system's performance.

The analysis presented in Fig. 7.19 provides details on the behaviour of $\Delta\dot{\theta}$ and P_{PTO} for the two PTO systems. The application of sub-gradient optimisation introduces a notable change in the performance of the system. Both $\Delta\dot{\theta}$ and f_{PTO} are amplified for a part of a motion period, suggesting an enhancement in the PTO power output. *body*_3 is almost kept declutched all the time and allowed to move freely, thus gaining larger acceleration. This strategy leads to PTO_2 having little to no power output. By sacrificing PTO_2, the system as a whole achieves a higher level of efficiency.

From Fig. 7.20, we see the variation in total power output (P_{PTO}) with and without the application of sub-gradient optimisation. The power output with sub-gradient optimisation is not only higher but also more concentrated. This suggests that sub-gradient optimisation effectively enhances the system's ability to harness wave energy. Figure 7.21 clearly illustrates the strategic sacrifice of PTO_2 in order to enhance the overall power output of the system. Figure 7.22 illustrates the controlled damping coefficients for the PTO systems. The activation of declutching control in PTO_1 demonstrates a regular pattern. In contrast, PTO_2 consistently exhibits activation

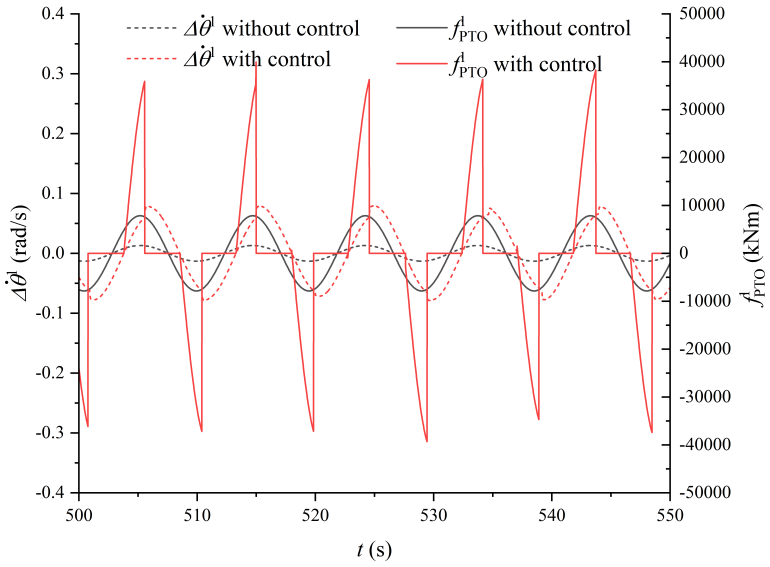

(a) *PTO*_1.

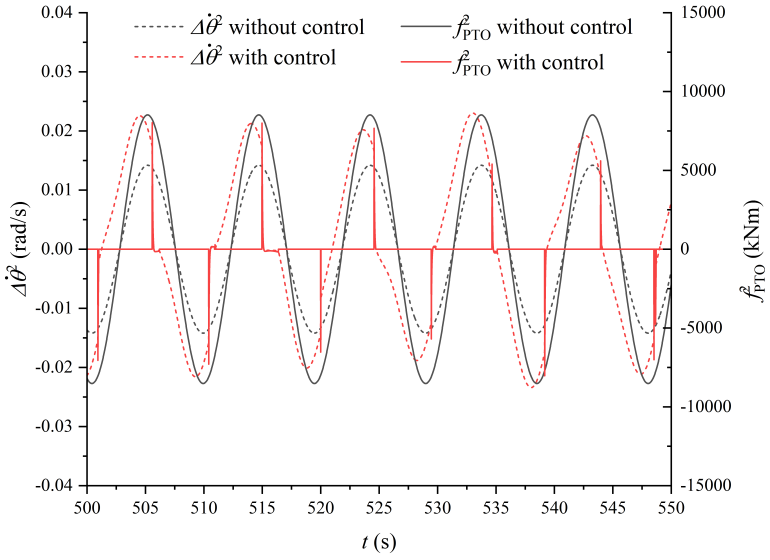

(b) *PTO*_2.

Figure 7.19: The relationship of $\Delta\dot{\theta}$ and P_{PTO} of (a) *PTO*_1 and (b) *PTO*_2 with sub-gradient optimisation.

of declutching control, ensuring the floating bodies all get enough acceleration.

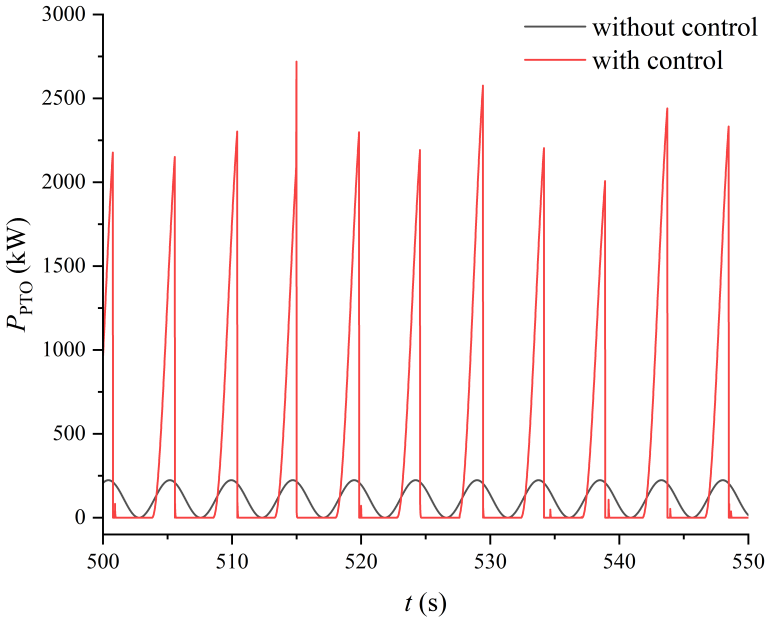

Figure 7.20: The total power output of the system with sub-gradient optimisation.

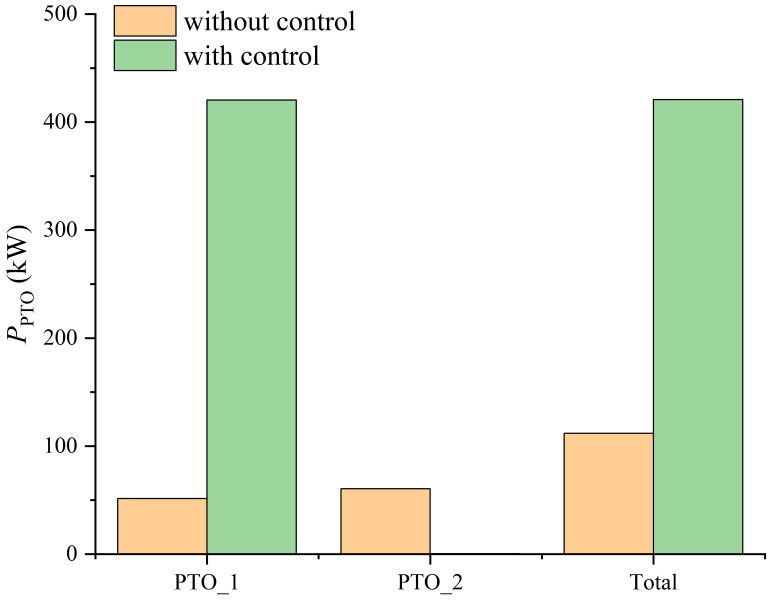

Figure 7.21: The power output of the two PTO systems with sub-gradient optimisation.

7.4.3 Control effect comparison

The comparison between the sub-gradient method and PMP in optimising P_{PTO} for multi-body WEC is presented in Fig. 7.23. Although without a faster convergence

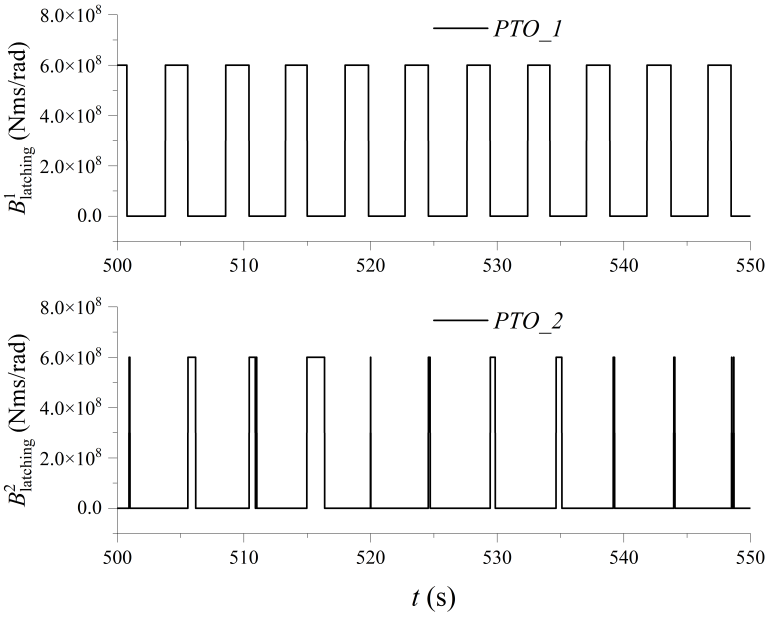

Figure 7.22: The controlled PTO damping coefficients of the system with sub-gradient optimisation.

speed in *err*, the sub-gradient method shows an ability to prevent the algorithm from getting trapped in undesired local optima. The increase in P_{PTO} of the sub-gradient method observes an impressive 11.13 times greater than the PMP method, highlighting the significant potential of sub-gradient methods in optimising multi-body WEC systems. This improvement is so significant that a logarithmic scale is required on the right y-axis to appropriately represent the results.

The comparison between the sub-gradient method and PMP in optimising P_{PTO} for multi-body WEC is presented in Fig. 7.24. Three scenarios are presented: without control, with declutching control, and with sub-gradient optimisation.

For PTO_1, when without control, the power output is 51.4 kW; when with declutching control, the power output decreases to 18.5 kW but remains within the same order of magnitude; when with sub-gradient optimisation, the power output experiences a dramatic increase, jumping to more than 420.4 kW, indicating the significant enhancement provided by this method. For PTO_2, the results are quite different: when without control, the power output is 60.5 kW, similar to PTO_1; when with declutching control, there is also a moderate decrease to 16.2 kW in power output;

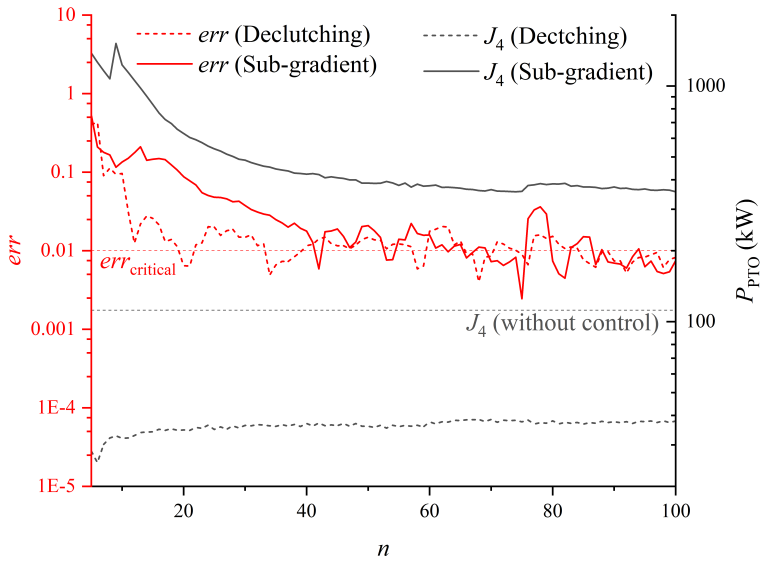

Figure 7.23: The variation of err and P_{PTO} with the number of iterations with the two optimisation algorithms. (Left y-axis in logarithmic scale)

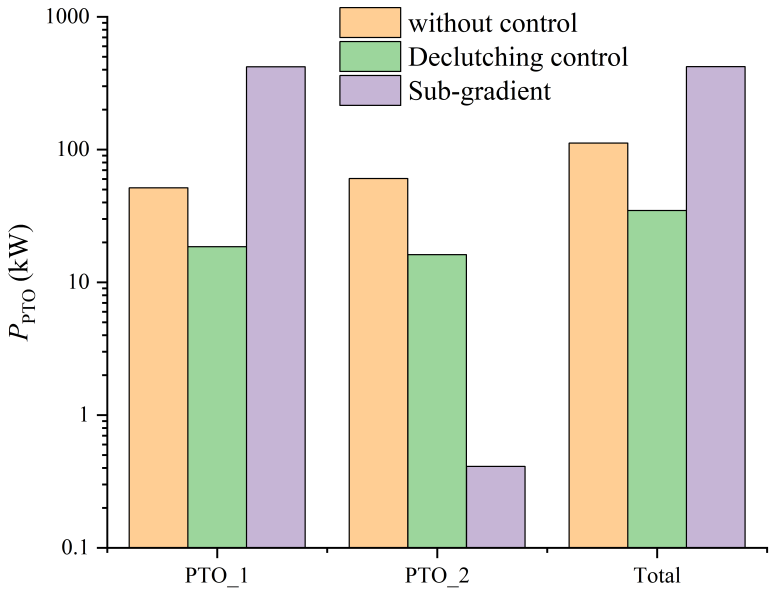

Figure 7.24: The power output of the two PTO systems with the two optimisation algorithms.

when with sub-gradient optimisation, the power output drops to around 0.4 kW, which corroborates the conclusions earlier that PTO_2 is "sacrificed" to increase the total power output. The logarithmic scale on the y-axis allows for a clearer comparison of values that have large differences. The sub-gradient optimisation result for PTO_1 is

two orders of magnitude higher than that without control, which would be difficult to discern on a linear scale.

7.5 Summary

The effectiveness of increasing the power output of multi-body WEC is highly related to the form of objective functions and the chosen optimisation method. A discontinuous objective function will reduce the efficiency of optimal control strategies. Non-smooth optimisation method is proven to be an effective alternative to Pontryagin's Maximum Principle in addressing discontinuous objective functions.

Notably, in this chapter, the objective function is set as the collaborative power output of the two PTO systems. However, in the case of a three-body system, optimal control involves optimising the power absorption from two separate PTO systems simultaneously. This multi-objective problem presents a complex challenge but can be solved using Pareto optimisation, which provides a potential direction for future research.

Chapter 8

Conclusions and Future Work

8.1 Conclusions

With the rapid advancement of offshore renewable energy, developing optimal control strategies for multiple floating bodies has emerged as a critical area of practical application. This thesis explores multiple disciplines, including floating multi-body dynamics, advanced control strategies, and optimisation algorithms. Its main objective is to fill the gap between theory and real-world applications in the domain of multiple floating body control. The main chapters of this thesis detail the realisation of simulated optimal control in three cases involving multiple floating bodies. The key conclusions are as follows:

1. A novel optimal declutching control method is developed to realise the control of floating multiple bodies. The control effect of optimising performance is based on the maximising or minimising of objective functions, including the motion mitigation ($\bar{J}_1$), the enhancement of the wave power absorption ($\bar{J}_2$), the increase of relative angular velocity between bodies ($\bar{J}_3$), and the enhancement of PTO power absorption ($\bar{J}_4$). In the case of hinged boxes, each of the objective functions can effectively accomplish its designated task enhancing performance.

2. In the case of hinged boxes, the mechanism of control can be shown through the relationship of velocities and forces. With respect to $\bar{J}_1$, motion mitigation

is achieved by tuning the phase of the damping force to be in anti-phase with the motion of the controlled body. For $\bar{J}_2$, the key point is aligning the velocity and wave force in phase. For $\bar{J}_3$, the objective is to position the velocities of the two bodies in anti-phase. Meanwhile, for $\bar{J}_4$, the control effect lies in the optimisation of the damping force. Besides, the control effectiveness of the four objective functions is sensitive to the variation of wave frequency.

3. In exploring motion control within multiple floating body systems, the research selects an SS-ring system (Semi-submersible platform combined with a ring-type WEC) and a Spar-plate system as case studies. It has been observed that the motion of the platform is effectively reduced under both regular wave and irregular sea conditions through optimal declutching control. The damping force between bodies provides a resistance effect to mitigate the motion of platforms. Simultaneously, as a beneficial "by-product", the energy absorbed by PTO experiences an increase.

4. For the proposed Spar-plate system, a detailed parametric analysis was undertaken. This analysis focused on assessing the impact of the hinged plate's mass (r_{M}) and the damping coefficient of PTO system (B_{PTO}) is investigated. The results indicate that achieving the optimal control effect does not necessarily require a large plate. Conversely, an over-large plate tends to shift the system's dynamics to be predominantly driven by inertia forces, making the control effect of damping force less noticeable. For a small plate, the control effect increases with B_{PTO}.

5. The primary goal for multi-body WECs is to maximise the PTO power output. However, the optimal declutching will cause discontinuity of the controlled PTO damping force. This may lead to issues with convergence or sub-optimal control effects. This inherent limitation of the method can be addressed either by modifying the objective function or by employing non-smooth optimisation techniques, which are adept at handling discontinuous objective functions.

8.2 Future work

1. The optimal control method for multiple floating bodies proposed in this thesis exhibits significant potential for integration within a Model Predictive Control framework, which contains three subsections: prediction, optimisation, and control. For wave prediction, an Artificial Neural Network could be employed. Based on this integration, the impacts of varying prediction and control horizons on the system's performance can be investigated.

2. The concept of controlling multiple floating bodies has a wide range of applications beyond the scope of this thesis. This includes scenarios such as wave attenuation problems using multiple floating breakwaters, stabilisation in floating photovoltaic systems, and operational efficiency of maritime transportation like sea trains.

3. The proposed spar-plate design has a limitation concerning its dependency on wave direction. Specifically, the motion mitigation effectiveness of the pitch plate is significantly diminished when the wave angle approaches 90 or 270 degrees. To address this directional sensitivity, a potential solution could be attaching additional plates beneath the pitch plate, oriented in various directions. This could enhance the system's responsiveness and effectiveness across a broader range of wave angles.

4. When objective function has multiple time-variant variables that are related to control, the trajectories are possible to vary significantly. In this case, the application of traditional optimal control methods may lead to lengthy iterations and, in some cases, fail to converge to an optimum. It is necessary to try some alternative global optimisation methods, such as Simulated Annealing, Genetic Algorithms, Particle Swarm Optimisation, and ant colony optimisation.

Bibliography

[1] Made Jaya Muliawan, Madjid Karimirad, and Torgeir Moan. Dynamic response and power performance of a combined Spar-type floating wind turbine and coaxial floating wave energy converter. *Renewable Energy*, 50:47–57, 2 2013.

[2] Mirko Previsic, Jeff Epler, Maureen Hand, Donna Heimiller, Walter Short, and Kelly Eurek. The future potential of waver power in the United States. Technical report, Re Vision Consulting, LLC, Sacramento, California, 2012.

[3] John V. Ringwood, Giorgio Bacelli, and Francesco Fusco. Energy-maximizing control of wave-energy converters: The development of control system technology to optimize their operation. *IEEE Control Systems*, 34(5):30–55, 10 2014.

[4] A Robertson, J Jonkman, M Masciola, H Song, A Goupee, A Coulling, and C Luan. Definition of the Semisubmersible Floating System for Phase II of OC4. Technical report, National Renewable Energy Lab.(NREL), Golden, CO (United States), 2014.

[5] Solomon C.S. Yim, Tongchate Nakhata, and Erick T. Huang. Coupled nonlinear barge motions, part II: Stochastic models and stability analysis. *Journal of Offshore Mechanics and Arctic Engineering*, 127(2):83–95, 5 2005.

[6] J Jonkman. Definition of the Floating System for Phase IV of OC3. Technical report, National Renewable Energy Lab.(NREL), Golden, CO (United States), 2010.

[7] DNVGL. DNVGL-RP-0286 Coupled analysis of floating wind turbines. Technical report, DNV GL, Oslo, Norway, 2019.

[8] Main types of WEC.

[9] Li Guo Wang and John V. Ringwood. Control-informed ballast and geometric optimisation of a three-body hinge-barge wave energy converter using two-layer optimisation. *Renewable Energy*, 171:1159–1170, 6 2021.

[10] Ross Henderson. Design, simulation, and testing of a novel hydraulic power take-off system for the Pelamis wave energy converter. *Renewable Energy*, 31(2):271–283, 2 2006.

[11] Richard Yemm, David Pizer, Chris Retzler, and Ross Henderson. Pelamis: Experience from concept to connection. *Philosophical Transactions of the Royal Society A: Mathematical, Physical and Engineering Sciences*, 370(1959):365–380, 1 2012.

[12] J. Cameron McNatt and Christopher H. Retzler. The performance of the Mocean M100 wave energy converter described through numerical and physical modelling. *International Marine Energy Journal*, 3(1):11–19, 5 2020.

[13] Odd Faltinsen. *Sea loads on ships and offshore structures*, volume 1. Cambridge university press, 1993.

[14] John Nicholas Newman. *Marine hydrodynamics*. The MIT press, 1977.

[15] W. E. Cummins. The impulse response function and ship motions. Technical report, DAVID TAYLOR MODEL BASIN, WASHINGTON D C, 1962.

[16] M. Masubuchi and R. Kawatani. Frequency Response Analysis of an Ocean Wave Energy Converter. *Journal of Dynamic Systems, Measurement, and Control*, 105(1):30–38, 3 1983.

[17] Y.R. Choi and S.Y. Hong. An Analysis of Hydrodynamic Interaction of Floating Multi-Body Using Higher-Order Boundary Element Method. In *The Twelfth International Offshore and Polar Engineering Conference*. International Society of Offshore & Polar Engineers, 2002.

[18] Zhi Ming Yuan, Atilla Incecik, Saishuai Dai, Day Alexander, Chun Yan Ji, and Xinshu Zhang. Hydrodynamic interactions between two ships travelling or stationary in shallow waters. *Ocean Engineering*, 108:620–635, 11 2015.

[19] Masashi Kashiwagi, Kazuaki Endo, and Hiroshi Yamaguchi. Wave drift forces and moments on two ships arranged side by side in waves. *Ocean Engineering*, 32(5-6):529–555, 4 2005.

[20] Deqing Zhang, Zhi Ming Yuan, Junfeng Du, and Huajun Li. Hydrodynamic modelling of large arrays of modularized floating structures with independent oscillations. *Applied Ocean Research*, 129, 12 2022.

[21] Min Zhang and Sebastian Schreier. Review of wave interaction with continuous flexible floating structures, 11 2022.

[22] Henry Lei Han. A Novel 6DOF Rigid Connector for Large Floating Platforms. In *International Conference on Offshore Mechanics and Arctic Engineering*, volume 42711, pages 17–26, 2007.

[23] R S Langley. Random dynamic analysis of multi-body offshore structures. *Ocean Engng*, 11(4):381–401, 1984.

[24] J N Newman. Wave effects on deformable bodies. *Applied Ocean Research*, 16:47–59, 1994.

[25] L. Sun, R. Eatock Taylor, and Y. S. Choo. Responses of interconnected floating bodies. *IES Journal Part A: Civil and Structural Engineering*, 4(3):143–156, 8 2011.

[26] Si Ming Zheng, Yong Hao Zhang, Yong Liang Zhang, and Wan An Sheng. Numerical study on the dynamics of a two-raft wave energy conversion device. *Journal of Fluids and Structures*, 58:271–290, 10 2015.

[27] Ramkumar Kandasamy, Fangsen Cui, Nicholas Townsend, Choon Chiang Foo, Junyan Guo, Ajit Shenoi, and Yeping Xiong. A review of vibration control methods for marine offshore structures, 11 2016.

[28] Christian Cermelli, Dominique Roddier, and Alexia Aubault. WindFloat: a floating foundation for offshore wind turbines—part II: hydrodynamics analysis. In *International conference on offshore mechanics and arctic engineering*, pages 135–143, 2009.

[29] Carlos Lopez-Pavon and Antonio Souto-Iglesias. Hydrodynamic coefficients and pressure loads on heave plates for semi-submersible floating offshore wind turbines: A comparative analysis using large scale models. *Renewable Energy*, 81:864–881, 9 2015.

[30] S Sudhakar and S Nallayarasu. Influence of heave plate on hydrodynamic response of spar. In *International conference on offshore mechanics and arctic engineering*, pages 437–447, 2011.

[31] Gustavo R.S. Assi, Tommaso Crespi, and Morteza Gharib. Novel geometries of serrated helical strakes to suppress vortex-induced vibrations and reduce drag. *Applied Ocean Research*, 120, 3 2022.

[32] Peter Bearman and Maša Branković. Experimental studies of passive control of vortex-induced vibration. *European Journal of Mechanics, B/Fluids*, 23(1):9–15, 1 2004.

[33] Saman Rashidi, Masoud Hayatdavoodi, and Javad Abolfazli Esfahani. Vortex shedding suppression and wake control: A review, 11 2016.

[34] T. Zhou, S. F.Mohd Razali, Z. Hao, and L. Cheng. On the study of vortex-induced vibration of a cylinder with helical strakes. *Journal of Fluids and Structures*, 27(7):903–917, 10 2011.

[35] M J Downie, J M R Graham, C Hall, A Incecik, and I Nygaard. An experimental investigation of motion control devices for truss spars. *Marine Structures*, 13(2):75–90, 2000.

[36] O. A. Montasir and V. J. Kurian. Effect of slowly varying drift forces on the motion characteristics of truss spar platforms. *Ocean Engineering*, 38(13):1417–1429, 9 2011.

[37] Matthew A. Lackner and Mario A. Rotea. Passive structural control of offshore wind turbines. *Wind Energy*, 14(3):373–388, 2011.

[38] Mi An Xue, Peng Dou, Jinhai Zheng, Pengzhi Lin, and Xiaoli Yuan. Pitch motion reduction of semisubmersible floating offshore wind turbine substructure using a tuned liquid multicolumn damper. *Marine Structures*, 84, 7 2022.

[39] Hamid Hokmabady, Alireza Mojtahedi, Samira Mohammadyzadeh, and Mir Mohammad Ettefagh. Structural control of a fixed offshore structure using a new developed tuned liquid column ball gas damper (TLCBGD). *Ocean Engineering*, 192, 11 2019.

[40] Zili Zhang and Christian Høeg. Inerter-enhanced tuned mass damper for vibration damping of floating offshore wind turbines. *Ocean Engineering*, 223, 3 2021.

[41] Semyung Park, Matthew A Lackner, P Pourazarm, John Cross-Whiter GLOSTEN Seattle, and Usa A Rodriguez Tsouroukdissian. An investigation on the impacts of passive and semi-active structural control on a fixed-bottom and a floating offshore wind turbine. *Wind Energy*, 22(11):1451–1471, 2015.

[42] J M Jonkman. Influence of control on the pitch damping of a floating wind turbine. In *46th AIAA aerospace sciences meeting and exhibit*, page 1306, 1 2008.

[43] Hoai Vu Anh Truong, Tri Dung Dang, Cong Phat Vo, and Kyoung Kwan Ahn. Active control strategies for system enhancement and load mitigation of floating offshore wind turbines: A review, 12 2022.

[44] Zhongyou Wu and Yaoyu Li. Hybrid model predictive control of floating offshore wind turbines with artificial muscle actuated mooring lines. *Journal of Dynamic Systems, Measurement and Control, Transactions of the ASME*, 144(5), 5 2022.

[45] Zhongzhou Yang and Yaoyu Li. Active vertical vane control for stabilizing platform roll motion of floating offshore turbines. *Wind Energy*, 21(11):997–1010, 11 2018.

[46] Kaustubh Khedkar, Nishant Nangia, Ramakrishnan Thirumalaisamy, and Amneet Pal Singh Bhalla. The inertial sea wave energy converter (ISWEC) technology: Device-physics, multiphase modeling and simulations. *Ocean Engineering*, 229, 6 2021.

[47] Tristan Perez. *Ship motion control: course keeping and roll stabilisation using rudder and fins*. Springer Science & Business Media, 2006.

[48] Ferdi Cakici and Emre Kahramanoglu. Numerical roll motion control by using fins based on the linear quadratic regulator and dynamic mode decomposition. *Applied Ocean Research*, 142, 1 2024.

[49] Lifen Hu, Ming Zhang, Xingxing Yu, Zhi Ming Yuan, and Wubin Li. Real-time control of ship's roll motion with gyrostabilisers. *Ocean Engineering*, 285, 10 2023.

[50] Javier López-Queija, Eider Robles, Josu Jugo, and Santiago Alonso-Quesada. Review of control technologies for floating offshore wind turbines, 10 2022.

[51] K Budal and J Falnes. Interacting point absorbers with controlled motion. In *Conference on Power form Sea Waves*, pages 381–399, 1980.

[52] M Greenhow and S P White. Optimal heave motion of some axisymmetric wave energy devices in sinusoidal waves. *Applied Ocean Research*, 19(3-4):141–159, 1997.

[53] Jørgen Hals, Johannes Falnes, and Torgeir Moan. Constrained optimal control of a heaving buoy wave-energy converter. *Journal of offshore mechanics and Arctic engineering*, 133(1), 2011.

[54] R E Hoskin and Nancy Nichols. Optimal strategies for phase control of wave energy devices. In *ASCE Specialty Conference, Utilization of Ocean Waves*, pages 184–199. ASCE: American Society of Civil Engineers, 6 1987.

[55] A. Babarit, G. Duclos, and Alain H. Clément. Comparison of latching control strategies for a heaving wave energy device in random sea. *Applied Ocean Research*, 26(5):227–238, 2004.

[56] Aurélien Babarit and Alain H Clément. Optimal latching control of a wave energy device in regular and irregular waves. *Applied Ocean Research*, 28(2):77–91, 2006.

[57] António F.de O. Falcão. Phase control through load control of oscillating-body wave energy converters with hydraulic PTO system. *Ocean Engineering*, 35(3-4):358–366, 3 2008.

[58] Stephen H Salter, J R M Taylor, and N J Caldwell. Power conversion mechanisms for wave energy. *Proceedings of the Institution of Mechanical Engineers, Part M: Journal of Engineering for the Maritime Environment*, 216(1):1–27, 2002.

[59] A Babarit, Michel Guglielmi, and A H Clement. Declutching control of a wave energy converter. *Declutching control of a wave energy converter. Ocean Engineering*, 36:12–13, 2009.

[60] Jørgen Hals, Johannes Falnes, and Torgeir Moan. A comparison of selected strategies for adaptive control of wave energy converters. *Journal of Offshore Mechanics and Arctic Engineering*, 133(3), 3 2011.

[61] Xian-Tao Zhang, Jian-Min Yang, and Long-Fei Xiao. Declutching control of a point absorber with direct linear electric PTO systems. *Ocean Systems Engineering*, 4(1):63–82, 3 2014.

[62] L. Li, Y. Gao, D. Z. Ning, and Z. M. Yuan. Development of a constraint non-causal wave energy control algorithm based on artificial intelligence. *Renewable and Sustainable Energy Reviews*, 138, 3 2021.

[63] Changhai Liu, Zhixue Zhao, Min Hu, Wenzhi Gao, Jian Chen, Hao Yan, Yishang Zeng, Tao Zhang, Xuling Liu, Qingjun Yang, Gang Bao, Suxin Chen, and Daozhu Wei. A novel discrete control for wave energy converters with a hydraulic power take-off system. *Ocean Engineering*, 249, 4 2022.

[64] Lev Semenovich Pontryagin. *Mathematical theory of optimal processes*. Routledge, 2018.

[65] Richard Bellman. Dynamic programming. *Science*, 153(3731):34–37, 1966.

[66] Rudolf Emil Kalman. Contributions to the theory of optimal control. *Bol. soc. mat. mexicana*, 5(2):102–119, 1960.

[67] E J McShane. The calculus of variations from the beginning through optimal control theory. *SIAM journal on control and optimization*, 27(5):916–939, 1989.

[68] José J. Cândido and Paulo A.P.S. Justino. Modelling, control and Pontryagin Maximum Principle for a two-body wave energy device. *Renewable Energy*, 36(5):1545–1557, 5 2011.

[69] Changhai Liu, Qingjun Yang, and Gang Bao. Latching control using optimal control method for a raft-type wave energy converter. *Ships and Offshore Structures*, 13(sup1):138–154, 2018.

[70] Guang Li, George Weiss, Markus Mueller, Stuart Townley, and Mike R. Belmont. Wave energy converter control by wave prediction and dynamic programming. *Renewable Energy*, 48:392–403, 12 2012.

[71] Michael Richard Belmont, J M K Horwood, R W F Thurley, and J Baker. Shallow angle wave profiling lidar. *Journal of Atmospheric and Oceanic Technology*, 24(6):1150–1156, 2007.

[72] J. C.C. Henriques, J. M. Lemos, L. Eça, J. N.H. Valério, L. M.C. Gato, and A. F.O. Falcão. A Discontinuous Galerkin Method for optimal and sub-optimal control applied to an oscillating water column wave energy converter. *IFAC-PapersOnLine*, 50(1):15670–15677, 7 2017.

[73] J. C.C. Henriques, L. M.C. Gato, A. F.O. Falcão, E. Robles, and F. X. Faÿ. Latching control of a floating oscillating-water-column wave energy converter. *Renewable Energy*, 90:229–241, 5 2016.

[74] Jinming Wu, Yingxue Yao, Liang Zhou, and Malin Göteman. Real-time latching control strategies for the solo Duck wave energy converter in irregular waves. *Applied Energy*, 222:717–728, 7 2018.

[75] J. Ross Halliday, David G. Dorrell, and Alan R. Wood. An application of the Fast Fourier Transform to the short-term prediction of sea wave behaviour. *Renewable Energy*, 36(6):1685–1692, 6 2011.

[76] M. R. Belmont, J. M.K. Horwood, R. W.F. Thurley, and J. Baker. Filters for linear sea-wave prediction. *Ocean Engineering*, 33(17-18):2332–2351, 12 2006.

[77] Liang Li, Zhiming Yuan, and Yan Gao. Maximization of energy absorption for a wave energy converter using the deep machine learning. *Energy*, 165:340–349, 12 2018.

[78] GL DNV. Sesam User Manual-HydroD. Technical report, DNV GL, Høvik, Norway, 2013.

[79] George Biddell Airy. *Tides and waves*. B. Fellowes, 1845.

[80] DNV GL. WADAM-wave analysis by diffraction and morison theory. Technical report, DNV GL, 2019.

[81] Tristan Perez and Thor I. Fossen. A Matlab toolbox for parametric identification of radiation-force models of ships and offshore structures. *Modeling, Identification and Control*, 30(1):1–15, 2009.

[82] Johannes Falnes. *Ocean Waves and Oscillating Systems: Linear Interactions Including Wave-Energy Extraction*. Cambridge University Press, Cambridge, 2002.

[83] Subrata Chakrabarti, Jeffrey Barnett, Harish Kanchi, Anshu Mehta, and Jinsuk Yim. Design analysis of a truss pontoon semi-submersible concept in deep water. *Ocean Engineering*, 34(3-4):621–629, 3 2007.

[84] Ruisheng Ma, Kaiming Bi, and Hong Hao. Mitigation of heave response of semi-submersible platform (SSP) using tuned heave plate inerter (THPI). *Engineering Structures*, 177:357–373, 12 2018.

[85] F Paparella and J V Ringwood. Optimal Control of a Three-Body Hinge-Barge Wave Energy Device Using Pseudospectral Methods. *IEEE Transactions on Sustainable Energy*, 8(1):200–207, 2017.

[86] Andrew Paulmeno and Sarah E Mouring. Design and Testing of a Model Scale McCabe Wave Pump. In *ISOPE International Ocean and Polar Engineering Conference*, pages ISOPE–I. ISOPE, 2013.